2017

UTILIZATION OF BIO-RENEWABLE LIGNIN IN BUILDING HIGH CAPACITY, DURABLE, AND LOW-COST SILICON-BASED NEGATIVE ELECTRODES FOR LITHIUM-ION BATTERIES

Tao Chen
University of Kentucky, tao.chen@uky.edu
Digital Object Identifier: https://doi.org/10.13023/ETD.2017.219

STUDENT AGREEMENT:

I represent that my thesis or dissertation and abstract are my original work. Proper attribution has been given to all outside sources. I understand that I am solely responsible for obtaining any needed copyright permissions. I have obtained needed written permission statement(s) from the owner(s) of each third-party copyrighted matter to be included in my work, allowing electronic distribution (if such use is not permitted by the fair use doctrine) which will be submitted to UKnowledge as Additional File.

I hereby grant to The University of Kentucky and its agents the irrevocable, non-exclusive, and royalty-free license to archive and make accessible my work in whole or in part in all forms of media, now or hereafter known. I agree that the document mentioned above may be made available immediately for worldwide access unless an embargo applies.

I retain all other ownership rights to the copyright of my work. I also retain the right to use in future works (such as articles or books) all or part of my work. I understand that I am free to register the copyright to my work.

REVIEW, APPROVAL AND ACCEPTANCE

The document mentioned above has been reviewed and accepted by the student's advisor, on behalf of the advisory committee, and by the Director of Graduate Studies (DGS), on behalf of the program; we verify that this is the final, approved version of the student's thesis including all changes required by the advisory committee. The undersigned agree to abide by the statements above.

Tao Chen, Student

Dr. Yang-Tse Cheng, Major Professor

Dr. Thomas Dziubla, Director of Graduate Studies

UTILIZATION OF BIO-RENEWABLE LIGNIN IN BUILDING HIGH CAPACITY, DURABLE, AND LOW-COST SILICON-BASED NEGATIVE ELECTRODES FOR LITHIUM-ION BATTERIES

DISSERTATION

A dissertation submitted in partial fulfillment
of the requirements for the degree of Doctor
of Philosophy in the College of Engineering
at the University of Kentucky

By
Tao Chen
Lexington, Kentucky

Director: Dr. Yang-Tse Cheng, Professor of Chemical and Materials Engineering
And Co-Director: Dr. Susan Odom, Professor of Chemistry
Lexington, Kentucky
2017

ABSTRACT OF DISSERTATION

UTILIZATION OF BIO-RENEWABLE LIGNIN IN BUILDING HIGH CAPACITY, DURABLE, AND LOW-COST SILICON-BASED NEGATIVE ELECTRODES FOR LITHIUM-ION BATTERIES

Silicon-based electrodes are the most promising negative electrodes for the next generation high capacity lithium ion batteries (LIB) as silicon provides a theoretical capacity of 3579 mAh g^{-1}, more than 10 times higher than that of the state-of-the-art graphite negative electrodes. However, silicon-based electrodes suffer from poor cycle life due to large volume expansion and contraction during lithiation/delithiation. In order to improve the electrochemical performance a number of strategies have been employed, such as dispersion of silicon in active/inactive matrixes, devising of novel nanostructures, and various coatings for protection. Amongst these strategies, silicon-carbon coating based composites are one of the most promising because carbon coating is comparatively flexible, easy to obtain, and scalable with various industrial processes.

Low cost and renewable lignin, which constitutes up to 30% dry mass of the organic carbon on earth, is widely available from paper and pulp mills which produce lignin in excess of 50 million tons annually worldwide. It is a natural bio-polymer with high carbon content and highly interconnected aromatic network existing as a structural adhesive found in plants. Generally burnt for energy on site, lignin is gradually finding its way into high value-added products such as precursor for carbon fibers, active material in negative electrodes, and raw material for supercapacitors.

This dissertation focuses on high performance silicon-based negative electrodes utilizing lignin as the carbon precursor for conductive additive, binder, and carbon coating. To my knowledge this is one of the first works attempting to utilize and summarize the performance of lignin in silicon-based negative electrodes. The first part of the dissertation shows that silicon-lignin composites treated at 800 ºC displayed good capacity and cycling performance. The second part goes to generalize the effect of temperature on silicon-lignin composites and shows that a low temperature treatment granted an electrode with superior performance and cycling properties owing to the preservation of polymeric properties of lignin. The final part of the dissertation discusses the current research trends in SiO_x based negative electrodes and extends lignin to that field.

This dissertation will, hopefully, provide knowledge and insight for fellow researchers wishing to utilize lignin or other renewable resources in devising advanced battery electrodes.

KEYWORDS: Lithium ion battery, bio-renewable, Si, SiO_x, lignin

Author's Signature: Tao Chen

Date: May 15th, 2017

UTILIZATION OF BIO-RENEWABLE LIGNIN IN BUILDING HIGH CAPACITY, DURABLE, AND LOW-COST SILICON-BASED NEGATIVE ELECTRODES FOR LITHIUM-ION BATTERIES

By

Tao Chen

Director of Dissertation: Dr. Yang-Tse Cheng

Co-Director of Dissertation: Dr. Susan Odom

Director of Graduate Studies: Dr. Thomas Dziubla

Date: May 15th, 2017

Dedicated to my Family

ACKNOWLEDGEMENTS

I would like to thank a lot of people for my wonderful life, research, and growth in Lexington and at the University of Kentucky. I appreciate everyone sincerely, though the list here may not be complete.

First of all, I would like to thank my advisor Dr. Yang-Tse Cheng for bringing me into his group and field of lithium-ion batteries. Without Dr. Cheng's gratitude for my unique background, continued support, understanding, and instructions for the past years, I may not be able to complete this dissertation. I would also like to thank my co-advisor, Dr. Susan Odom for guiding me in the correct research direction when there were many options. I would also like to thank Dr. Stephen E. Rankin and Dr. Mona Shirpour for serving on my Ph.D. Committee and Dr. Jian Shi as my outside examiner. Secondly, I would like to thank my former and current group members, such as Dr. Qinglin Zhang, Dr. Jie Pan, Dr. Jiagang Xu, Dr. Mohanad Al-Shroofy, Jiazhi Hu, Yikai Wang, Long Zhang, Dawei Li, Dingying Dang, Baleegh Alobaid, and Wang Ming, for their invaluable assistance and input. I would also like to thank Dr. Nicolas Briot and Dr. Dali Qian from the Electron Microscopy Center and Dr. Yiyang Liu from Department of Chemistry. I appreciate my advisor during my masters' degree, Dr. Bruce J. Hinds, for bringing me to the University of Kentucky and previous group members Dr. Zhiqiang Chen, Dr. Xin Su, and Dr. Ji Wu for their assistance. Many thanks to all the faculty and staff in the Department for their help along the way, especially Dr. Fuqian Yang and Dr. Thomas Dziubla.

I have spent a wonderful five and half years at the beautiful city of Lexington and made life-long friends, such as Dr. Yan Jin, Dr. Yitian Zhang, Dr. Jie Pan, Dr. Qinglin Zhang, Di Liang, and Yucong Sang.

Most importantly, I would like to thank my family and extended family which are the best in the world. I appreciate the fun I had growing up with my little brother and many great years to come.

Finally, I would like to thank the financial support from National Science Foundation (Award Number: 1355438).

TABLE OF CONTENTS

LIST OF FIGURES

LIST OF TABLES

Chapter 1 Introduction

We live in a world that consumes energy to fuel the luxuries resulting from our technological advancements. Fossil fuels, the largest consumed energy source, are not renewable and deemed to run out in the future. For this reason, renewable energy resources, such as hydro, wind, and solar energy, are important for long term sustainability. One of the characteristics of renewable energy resources is often their intermittency, meaning that an efficient, reliable, and cost-effective energy storage system is required to store energy at times of peak production to be released at times of peak consumption [1]. It is now generally accepted that among electrochemical batteries, the lithium-ion battery (LIB) system is the most promising candidate for the storage of renewable energy. LIB transforms various energy sources to chemical energy and can deliver this stored chemical energy as electrical energy with high conversion efficiency and without gaseous emission. Another concern is the global warming due to excessive CO_2 emission and imbalance of the global ecosystem, partly due to gaseous emissions from transportation vehicles. LIB powered electric vehicles (EVs), most of which do not emit gases, therefore are favorited by politicians, economic leaders, the scientific community, and major car makers as the inevitable next step to alleviate global warming problems.

Lithium-ion batteries, first introduced to market in 1991 by Sony [2], are the most popular battery technology due to their high gravimetric and volumetric energy, high power density, long cycle life, and low self-discharge [3-7]. They are already heavily used in consumer electronics such as laptops, mobile phones, medical devices, and electric vehicles (EVs), which provides a clean and green alternative to fossil fueled vehicles [5, 8]. However, the most typical LIB specific energy of ~200 Wh kg^{-1} currently means that LIB powered EVs are still not comparable to the performance of internal combustion vehicles. The uncompetitive price of $400-

600/KWh and low cycle life expectancy of 1000 cycles also hinder their large scale deployment in grid-scale and renewable energy storage systems [9].

The development of new materials and methods to improve LIB capacity and performance is critical to the incorporation of this technology at the grid level. Before the introduction of some of the recent developments, the fundamental working principles of LIBs are introduced.

1.1 Fundamentals of lithium-ion batteries

Figure 1 illustrates the basic LIB system that has dominated the market for years. The main cell is comprised of a few parts: the carbon (graphite) as the anode, a lithium metal oxide such as $LiCoO_2$ as the cathode, separator which physically separates the two electrodes, and the electrolyte which allows the movement of lithium ions during charge and discharge. The carbon, which is graphite specifically in this case, has a layered structure that allows Li intercalation between the layers as shown. The reaction of graphite and Li can be shown as:

$$C_6 + Li^+ + e^- \rightleftharpoons LiC_6$$

The cathode $LiCoO_2$, which is a layered structure, can also host Li with the following equation:

$$LiCoO_2 \rightleftharpoons \frac{1}{2}\, Li^+ + \frac{1}{2}\, e^- + Li_{0.5}CoO_2$$

Because of the lower potential of graphite toward Li (0.1 V vs Li/Li^+) compared to that of $LiCoO_2$ (3.9 V vs Li/Li^+), the graphite is used as the negative electrode during discharge; the $LiCoO_2$ used as the positive electrode during discharge. The electrolyte, of which the most common is lithium hexafluorophosphate ($LiPF_6$) dissolved in organic carbonate, must transport Li ions efficiently. 1) The electrolyte must be chemically stable with the various chemical species in

the operation window of the battery, usually from 3.0-4.2 V vs Li/Li^+; 2) have a high conductivity and low viscosity; 3) and possess the ability to form a stable solid electrolyte interface (SEI) to prevent further electrolyte decomposition. During the initial charging process, the organic solvent contained in the electrolyte decomposes at the negative electrode and forms an inactive SEI layer, which slows further decomposition of the electrolyte in subsequent cycles [10]. On one hand, the formation of SEI consumes cyclable Li provided by the cathode, lowering coulombic efficiency (CE); on the other hand, the formation of a stable SEI can prevent further physical contact of the anode material from the electrolyte, therefore preventing further degradation. The properties of SEI and its relevance to battery performance will be discussed throughout the chapters.

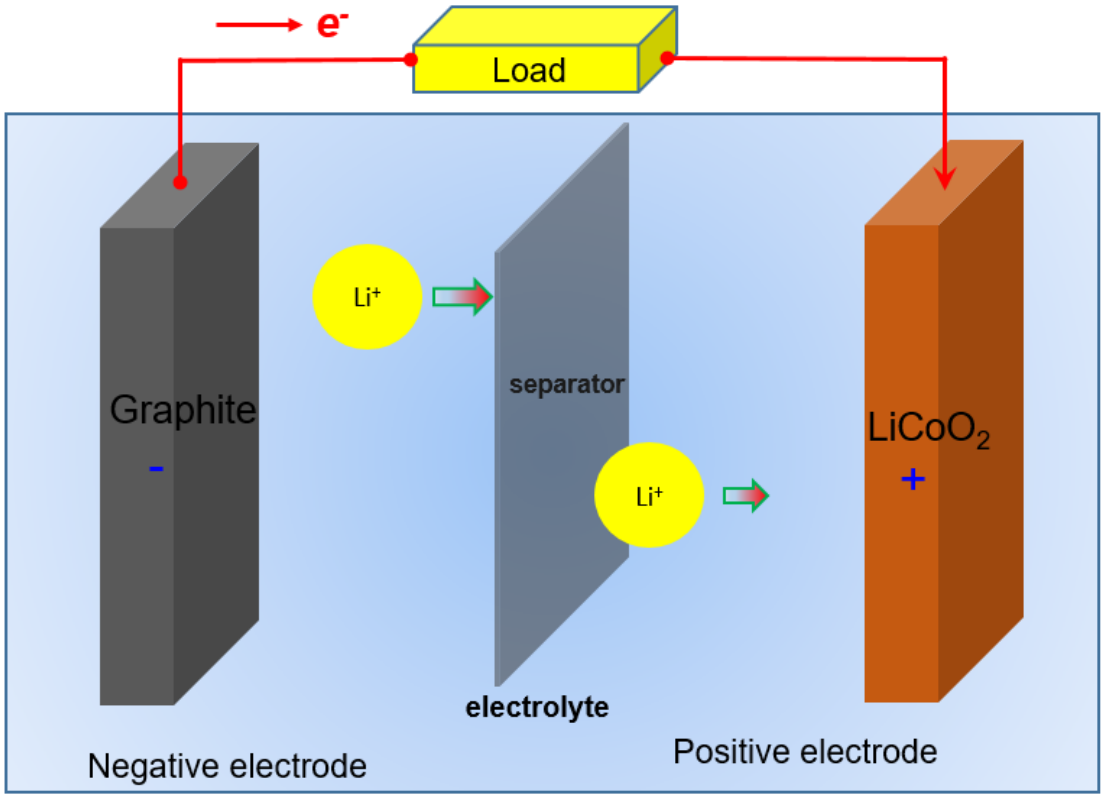

Figure 1.1. A schematic representation of the most commonly used LIB based on graphite anode and $LiCoO_2$ cathode during the discharge process.

The performance of LIBs can be described by several fundamental parameters. Specific capacity is defined as the amount of charge that can be stored per unit mass of the electrode material:

$$C_e = \frac{F \times z}{M \times 3.6}\ mAh\ g^{-1}$$

where C_e is the specific capacity, F is the Faradic constant, z is the amount of charge per mole of electrode material, and M is the molar mass of the formula electrode material. The specific capacity of the whole battery cell is determined by both the anode and the cathode, therefore the specific capacity of the full cell is:

$$C_{cell} = \frac{C_{e(anode)} \times C_{e(cathode)}}{C_{e(anode)} + C_{e(cathode)}}$$

It should be noted that in full cells, any additional mass besides the anode and cathode decreases the overall capacity.

Coulombic efficiency (CE) is another important factor in determining the cycling performance of LIBs, which is defined as the ratio of delithiation capacity to lithiation capacity in the same cycle [11]. High coulombic efficiency is important during extended cycling of LIBs, because even a 0.1% loss in CE (99.9%) leads to a 10% loss in capacity over 100 cycles, while a 1% loss in CE (99%) can result in nearly 64% loss over the same number of cycles.

All components of the LIB are essential for the overall performance, e.g., the anode and cathode decide theoretical capacities of the battery, separators are crucial safety features, and electrolyte along with additives type can determine the cycling performance of the cell. Therefore, extensive research has been carried out in all the LIB areas. Anode has been one of the hottest areas of research because elements with much higher theoretical capacity such as Si (3579 mAh g^{-1}) can potentially replace graphite (theoretical capacity of 372 mAh g^{-1}), while on the

cathode side no such material with dramatic increase in theoretical capacity was proposed. In the following section, common anode materials for LIBs, especially Si and SiO_x, is introduced in detail.

1.2 Anode materials of LIBs

Alternative anode materials are required in LIBs because the direct use of Li metal forms dendrites which can cause short circuiting, start a thermal runaway, and cause the battery to catch fire [12]. Although this can also occur in LIBs with other anodes such as graphite or Si, the problem is more prominent in Li metal LIBs due to the easy formation of dendrites. Recently, there is a resurgence to use Li metal directly as the anode material because the development of investigative tools and new nanotechnology-based concepts, which is reviewed in [13]. However, because Li metal based LIB chemistries such as Li-S and Li-Air are still in its infancy, only alternative electrode materials which can host Li is discussed further in detail.

1.2.1 Graphitic and hard carbons

The carbon based anode materials have enabled commercial LIBs for more than 20 years, and are the most dominant anode materials today [7]. The 2D graphene planes in graphite allow Li intercalation, mechanical stability, good electronic conductivity of $2\text{-}3x10^5$ S cm^{-1} along the basal plane, and Li^+ transport [14]. Furthermore, many forms of carbons are inexpensive, are widely available, have low delithiation potential, and undergo relatively low volume change during lithiation/delithiation (10%) [15]. The theoretical gravimetric capacity of carbon is 372 mAh g^{-1}, higher than most cathode materials, which ranges from 120-200 mAh g^{-1} [12].

Commercial carbon materials can be divided into two classes. Graphitic carbons have large graphitic grains and can achieve close to theoretic capacity. However, graphitic carbons do

not pair well with propylene carbonate (PC) electrolyte, which is preferred due to its low melting point of -49 °C and high ionic conductivity of 69 mS cm^{-1} [10]. PC intercalates between the graphitic planes, causing the graphite to exfoliate and lose capacity [16]. Because the inability to work under PC electrolyte conditions which facilitate fast Li ion transport, one of the disadvantages of graphitic carbons is thus moderate performance at high rates. Hard carbons have small graphitic grains with disordered orientation, and are much less likely to be exfoliated. Nano-voids and defects exist between the grains, resulting in measured capacities exceeding the theoretical 372 mAh g^{-1} [12]. Combined with the possibility of pairing with PC as the electrolyte, hard carbons yield high capacity, high-rate-performing electrodes. However, the high fraction of non-uniform edge planes increase quantity of SEI formed, resulting in low coulombic efficiency and consumption of Li provided by the cathode. Currently hard carbon anodes with high capacity of 400 mAh g^{-1} could be realized although with a low first cycle coulombic efficiency of 87%.

Due to the stable performance, low cost, and wide availability of carbons, it can be foreseen that in the near future carbon would still be the primary commercial anode material, or the major component of a composite anode material (with high capacity anode material such as Si or SiO_x).

1.2.2 Lithium titanium oxide ($Li_4Ti_5O_{12}$/LTO)

Lithium titanium oxide ($Li_4Ti_5O_{12}$, or LTO) has also been successfully commercialized because of its combination of thermal stability [17], high tolerance, relative high volumetric capacity, and high cycle life [18]. LTO features a low-strain intercalation mechanism where the phase change caused by lithiation/delithiation results in only 0.2% change in volume [19], which results in good cyclability.

The equilibrium potential of LTO is high (1.55 V vs Li/Li^+) compared to graphite (0.1 V vs Li/Li^+), which affects its electrochemical performance. First, this high potential large avoids the formation and growth of an anode SEI, which usually occurs at potentials <1 V *vs*. Li/Li^+. Because SEI formation does not occur, LTO nanoparticles can be used similar to the usage of intercalation cathode material without the need of coating protection, leading to superior rate performance [20]. Secondly, because of the high potential 1.55 V *vs*. Li/Li^+, LTO is safe because Li dendrites does not form at this high potential.

The drawbacks of the LTO electrode compared to carbon are the high cost of Ti, the reduced cell voltage, and lower theoretical capacity (175 mAh g^{-1}) compared to carbon-based electrodes [12]. Additionally, poor electronic conductivity (10^{-13} S cm^{-1}) of $Li_4Ti_5O_{12}$ limits its high rate performance.

1.2.3 Alloying materials anodes

An alloy is a mixture of chemical elements, which is formed by mixing two or more elements, at least one of which is a metal. Alloying anodes here refer to elements which electrochemically alloy and form compound phases with Li, such as Sn [21], Ge [22, 23], Ga [24], and Si [25]. Due to the properties of the elements, they feature low reaction potential *vs*. Li/Li^+, usually below 1 V. Alloying materials can have high volumetric and specific Li storage capacity, as summarized in Table 1.1, but with large volume change from 200-300% during lithiation/delithiation. For anodes, this is disastrous because the large volume expansion can lead to: 1) physical and electrical disconnection between electrode materials, leading to capacity decrease; 2) increased cell capacitance; and 3) unstable SEI layer that leads to the continuous consumption of cyclable Li and electrolyte decomposition. Thus, alloy-type anodes generally suffer from short cycle life due to the loss of active material and increasing cell impedance [12].

To address the large volume expansion of alloy materials and unstable SEI, a number of strategies have been proposed. Forming composites with a carbon matrix is preferred because it provides mechanical stability, and an electron transport path, while maintaining Li diffusion path [26-28]. The carbon coating can stabilize SEI growth and maintain integrity of the whole electrode. Electrolyte additives can also minimize the loss of Li by forming more stable SEI layers [29, 30]. Newly developed binders may help to increase the utilization of active anode material and enhance cyclability by weak bond interactions between the binder chemical moieties and alloy element surface groups [31-33].

Table 1.1. Specific, volumetric capacities for some elements, and their volume expansions.

Material	Specific capacity (mAh g^{-1})	Volumetric capacity (mAh mL^{-1})	Volume expansion	Ref
C	372	781	10%	[15]
Sn	993	7249	255%	[21, 34, 35]
Al	993	2681	200%	[35, 36]
Ge	1620	7366	240%	[34, 35, 37]
Si	3579	8339	300%	[34, 38]

1.2.4 Si and SiO_x anode materials

Of all alloy materials, Si has received the most attention not only because of its high specific and volumetric capacities as shown in Table 1.1, but also its relatively low delithiation potential, abundance, low cost, and biological inertness. However, as discussed, the large volume expansion

of Si during lithiation/delithiation results in quick capacity fade during cycling, of which a mechanism can be shown as in Figure 1.2. The enlarged volume of the anode upon lithiation results in the covering of Si with a high surface area layer of SEI, which collapses, disjoints, and folds upon volume contraction associated with delithiation. On the start of a new circle, fresh Si is exposed to the electrolyte and new SEI is created. As the result, Li and electrolyte are continuously consumed, and rapid fading of capacity is observed, which results in capacity values <500 mAh g-1 after just four cycles for a Si electrode using PVDF as binder [39]. Some of the approaches to deal with the volume expansion includes compositing with carbon matrixes, development of more compatible binders, and electrolyte additives. In addition to these approaches, various nanostructuring methods to reduce effect of volume changes were also heavily researched, which can be summarized into a few categories [40]: 1) 0D Si, that is, nanoparticles. Si nanoparticles (<140 nm) are less susceptible to effects of fracturing, pulverization, and disconnection compared to Si microparticles because of their small size. Some 0D Si nanostructures includes porous Si nanoparticles [41], Si-C core-shell nanostructures [42], silicon-graphene composite [43], and silicon-carbon nanotube composite [44]; 2) 1D Si, that is, Si nanotubes [45] and Si nanowires prepared by vapor-liquid-solid growth [46]. The long aspect ratio of these materials means shorter diffusion length for Li and better resistance to cracking and breaking; 3) 2D Si thin films [47]. Si thin films are attractive because they can be synthesized in large batches by common industrial synthesis methods such as physical vapor deposition (PVD) or chemical vapor deposition (CVD), and is superior in performance to that of Si microparticles.

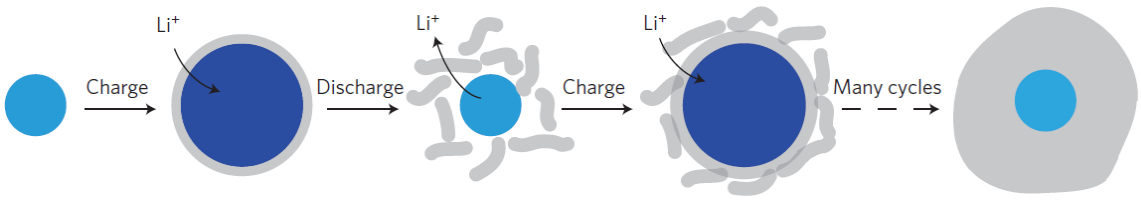

Figure 1.2. A solid silicon nanowire expands upon lithiation. A thin layer of SEI forms in this lithiated and expanded state. During delithiation, the silicon structures shrink, and the SEI can

break down into separate pieces, exposing fresh silicon surface to the electrolyte. In later cycles, new SEI continues to form on the newly exposed silicon surfaces, and this finally results in a very thick SEI layer on the outside of the silicon nanowires. Reproduced with permission [45]. Copyright 2012, Nature Publishing Group.

SiO_x-based anodes are a class of electrodes with many similarities to Si electrodes. In amorphous SiO_x, Si and O exist in clusters of Si and SiO_2 while surrounded by a variety of sub-oxide type tetrahedral coordinates at interface regions [48]. This means that in SiO_x, many types of Si-Si and Si-O bonds exist and Si exists in many valence states, such as Si^0, Si^{2+}, Si^{3+}, and Si^{4+}. The reversible Li host in SiO_x-based anodes is still Si, so the same lithiation/delithiation process happens between Li and Si. However, Li also reacts with SiO_2 irreversibly to create Li oxides and Li silicates, which usually do not react with Li, nor can the Li be retracted from them [49]. As the result, SiO_x-based anodes suffer from low initial coulombic efficiency (ICE). As the trade-off for the low ICE of 70-90%, SiO_x-based anodes can show amazing cycling performance of >90% retention after 400 cycles, which is superior compared to Si because the Li oxides and Li silicates act as inactive matrix to accommodate the volume changes and prevent Si from direct contact with electrolyte [50-52].

In today's state-of-the art LIBs, both Si and SiO_x have been added in small quantities to graphite to boost the specific capacity of the anode, with a weight ratio of typically less than <10%. One such product is a SiO/graphite composite from BTR China with capacity of 600-650 mAh g^{-1} [53]. At this weight composite range, the battery system can still use most of the components from a conventional graphite anode LIB with good performance. At higher weight composition ranges, the volume changes of Si and SiO_x begin to take over the properties of graphite and conventional components can no longer be used effectively. Therefore, it is of great interest to us to enable Si or SiO_x-based anodes by a simple and effective carbon compositing technique, which is the focus of this dissertation research.

1.3 Binders for Si and SiO_x anode

Si electrodes works poorly with traditional poly(vinylidene fluoride) (PVDF) binders, as a result a number of binders has been evaluated for Si electrodes, including sodium carboxymethyl cellulose (NaCMC) [39], polyacrylic acid (PAA) [33], polyimide imide [54], and alginate [31]. Alginate, a major constituent of brown algae, enables better cycling of Si electrodes by 1) inducing only weak interactions between the binder and the electrolyte; 2) providing access of Li^+ to the Si surface; 3) assisting in building a deformable and stable SEI layer on the Si surface. Overall significant electrochemical cycling performance was observed by the development of the binders. For SiO_x electrodes they were also applied, for example CMC [55, 56], PAA [51, 57], polyimide imide [58, 59], and alginate [60]. PVDF is still used in some SiO_x electrode works, such as [52, 61, 62]. Guerfi *et al*. [63] studied the effect of three types of binders, PVDF, CMC-based water dispersed binder (WDB), and polyimide on SiO_x/C or SiO_x/C-graphite (1:1 w:w) composite electrode electrochemical performance. The average size of the SiO_x particles was 7 µm. The highest 1st cycle reversible capacity was found in cells containing polyimide (1026 mAh g^{-1}), followed by WDB (817 mAh g^{-1}) and then PVDF (472 mAh g^{-1}). The cell with WDB had the highest 1st cycle CE, followed by polyimide and then PVDF. Through cross section in situ SEM, obvious disintegration of SiO_x particles and cracks due to cycling was observed for both electrodes. The authors confirm that there is difference in electrochemical performance when different binders were used with SiO_x, however a limited number of cycles and fixed SiO_x size was reported in the study. Komaba *et al*. [64] studied the effect of PAA, CMCNa, poly(vinyl alcohol) PVA, and PVDF binder on SiO_x cycling with a larger number of cycles. PAA binder showed the best performance as the reversible capacity reached 700-750 mAh g^{-1} for 50 cycles at a rate of 100 mA g^{-1}. SiO_x particles with the three other binders lost almost all of its capacity after

50 cycles. Through synergized analysis of XRD, electron microscopy, XPS, IR, and adhesive strength test, the authors attributed the good results to amorphous PAA being not only able to tightly bind, but also cover individual SiO_x particles. Additionally, PAA binder had a suppressing effect on electrode deformation compared to the PVDF binder. In 2013 Feng *et al*. [65] also studied alginate, CMC, and PAA binder performance with SiO_x/C or SiO_x electrodes and confirmed their beneficial effect in enhancing capacity retention due to their amorphous structure and high adhesion strength related to ester-like bonds. The best performance was seen when SiO_x/C electrode was combined with alginate or CMC binder.

Another non-conventional binder worth mentioning is functional conductive polymer binder poly(9,9-dioctylfluorene-*co*-fluorenone-*co*-methylbenzoic ester) (PFM) [66]. The polar ester functional group, which is designed for the adhesion with the SiO_2 surface, is especially suitable for SiO electrode material because it forms chemical bonding with the hydroxide terminated SiO_2 surface on via a trans-esterification reaction. Thus, the highly conductive polymer binder solves both the problem of low conductivity of SiO_x material and disconnection between active material and binder due to excessive volume change. As a result, reversible capacity of 1000 mAh g^{-1} for over 400 cycles with a 2% to 10% PFM was realized in the half cell. By using the conductive polymer binder PFM, the loading of active material SiO_x in the anode could be up to 98%, which realized capacities ~3 times higher than graphite in half cell. With addition of SLMP prelithiation Li powder, a SiO_x/NMC full cell was able to maintain a reversible capacity of ~110 mAh g^{-1} after more than 100 cycles at C/3, highlighting excellent properties of the binder.

Previously, polyacrylonitrile, PAN, has been used to composite with Si to form Si-C composites, retaining ~1500 mAh g^{-1} after 150 cycles, giving ~57.6% capacity retention [67]. One of the disadvantages to Si-PAN composite is its low capacity retention of 57.6% over 150 cycles.

Another is that PAN is produced from propene, which is extracted from non-renewable fossil fuels and is also expensive [68, 69]. In the search for a renewable carbon precursor with desirable chemical properties for forming a conductive matrix, lignin appeared as a potentially suitable candidate, and an overview of its properties and applications are discussed below.

1.4 Overview of lignin and its applications

1.4.1 Basics of lignin

Lignin is second only to cellulose as the most abundant renewable resource [70], and represents ~30% of all the non-fossil organic carbon on Earth [71]. In wood, the lignin weight percent is 20-25%, and 3-25% in other lignin sources such as cereal straws, bamboo, and bagasse. Lignin is the structural biopolymer that holds cellulose and hemicellulose together in plant species via covalent linkages. Therefore, it acts as a natural binder in plant species holding various elements together into a robust mechanical structure. Although many chemical aspects of lignin are still unclear today due to its complexity, it can be generally described as an amorphous and random polymer. Phenylpropane units constitute the main backbone of lignin, which is randomly cross-linked by a variety of different chemical bonds. Representation of a lignin polymer as predicted from NMR-based lignin analysis is shown in Figure 1.3. To summarize, lignin has the following characteristics: (1) basics of phenylpropylene units, (2) no repeating structure, and (3) amorphous, random polymer.

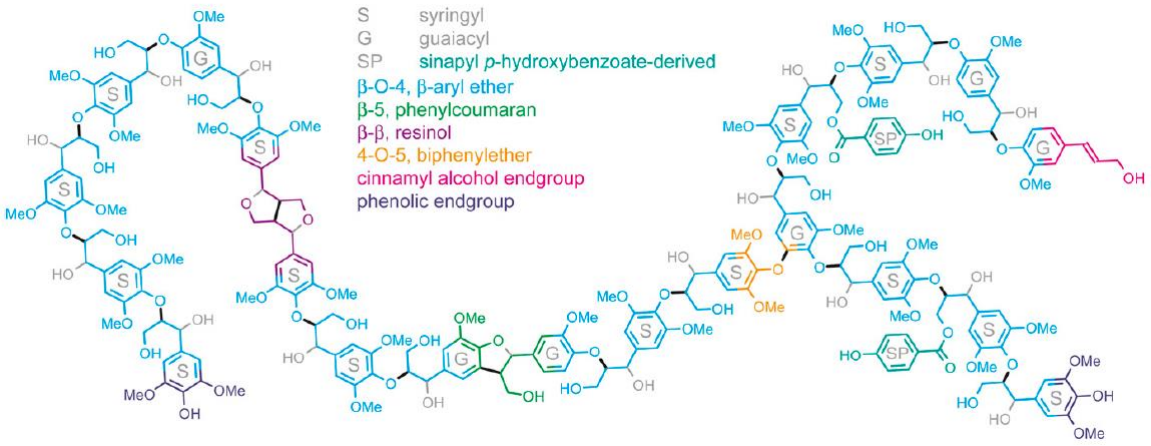

Figure 1.3. Representation of a lignin polymer from poplar, as predicted from NMR-based lignin analysis. Reproduced with permission [72]. Copyright 2013, American Society of Plant Biologists.

Available commercial lignins are side products of paper and pulp mills, where lignin is separated from cellulose, which can be made into paper. The worldwide low-purity lignin production in 2010 is estimated to be 50 million tons, but only 2% of that material was commercially used to make low value products such as dispersing or binding agents; the rest was burned as low-value fuel on-site [71]. Depending on the separation process, four main types of lignins are commonly available: 1) Kraft lignin, 2) lignosulfonate, 3) soda lignin, and 4) organosolv lignin. Kraft lignin is produced in the sulphate (Kraft) cooking process, where around 90-95% of the lignin contained in the wood is dissolved in the aqueous solution of sodium hydroxide and sodium sulfide. Kraft lignin contains several characteristics: 1) it contains an increased amount of phenolic hydroxyl groups [73]; 2) oxidative conditions during delignification can cause formation of quinone and catechol structures as well as increase the amount of carboxyl groups; 3) the molecular weight of Kraft lignin varies within range of 200 to 200,000 g/mol [74]. Soda lignins originates from soda or soda-anthraquinone pulping processes. The main difference in comparison to the Kraft process is the sulfur-free medium of the cooking liquor. Lignosulfonates are water-soluble polyelectrolytes that contain many charged groups, such as

phenolic hydroxyl groups, carboxylic groups, and sulphur containing groups as a result of sulphite cooking, in which the delignification was performed by means of HSO_3^- and SO_3^{2-} ions. Due to these groups lignosulfonates are comparatively dissolvable in water, enabling water-based application or preparation [75]. The production of lignosulfonates has been commercialized by main companies, of which the main producer is Borregard LignoTech with a capacity of about 500,000 tons [73]. In the organosolv lignin production process, a mixture of organic solvent/solvents and water is used as a cooking medium. The properties of organosolv lignins differ from other technical lignins. The major features are low molecular weight, high chemical purity, and poor solubility in water. Because of the complicated processes very small amounts of organosolv lignins are produced commercially.

1.4.2 Advanced applications of lignin

The current largest application of lignin is to directly burn it to generate energy, which accounts for 95% of the total lignin market [76]. Lignin is used as a replacement material for relatively low value chemicals or materials, such as additives for concrete mixtures, dust control, feed, food additives, and dispersants, accounting for 65% of the remaining 5% [76, 77].

Besides conversion into fuel and chemicals, lignin is promising in materials applications. One such platform is the global development of energy-efficient light weight vehicles. A body-in-white design-based model has demonstrated that 40-50% of the structural steel in a vehicle could be replaced with low weight carbon fiber composite materials [78]. However, to realize this goal, low-cost manufacturing of carbon fibers are required, but commercial carbon fibers derived from polyacrylonitrile (PAN) or pitch are too expensive for such type of large scale applications. Lignin, derived from biorefineries and pulp industry, could be an ideal substitute for PAN or pitch as carbon fiber precursor. Currently the production of carbon fibers from lignin has been demonstrated by a number of groups [68, 79-86]. Although huge advances were made in this

field, lignin-derived carbon fibers still suffer from poor mechanical properties compared with PAN or pitch derived counterparts. The disordered internal structures of carbon fibers from lignin are thought to be related to the amorphous and random structure of lignin. In order for lignin-derived carbon fibers to be competitive, new chemical modifications and/or innovative biosynthesis strategies are required [86, 87].

Lignin has also seen applications in energy-related fields. In 2012 Milczarek *et al*. [75] synthesized lignosulfonate/polypyrrole composite polymer films in aqueous environment. The oxidation of phenyl rings in lignosulfonate formed reversible quinone/hydroquinone redox groups, which provides a capacity of 496 mAh g^{-1} in electrons. The low conductivity of lignosulfonate was overcome by the high electronic conductivity of conductive polymer polypyrrole, which can also store charge reversibly. Further advances were made of this electrochemical system, although the requirement of aqueous solution environment reduced a lot of its practicality [88-90]. Lignin was also utilized as active anode material for LIBs [91-93] with capacities >360 mAh g^{-1}. Although the use of lignin as anode material precursor is attractive, its prices was not attractive compared to cheap commercial graphite. Compared as an active anode material for LIBs, lignin is more suitable as the precursor for porous carbons in supercapacitors and sodium ion batteries because it is a hard carbon precursor. Hard carbon refers to a type of non-graphitizable carbon produced by the pyrolysis of precursors such as organic polymers or hydrocarbons at T<1500 °C. The hard carbon structure is characterized by the ordering of most of the carbon atoms in the planar hexagonal networks but lack of long range order in the c direction [94]. Hard carbons cannot be graphitized even at high temperatures up to 3000 °C due to this lack of stack ordering. Because of this lack of long range order in the c direction, hard carbons can not only intercalate Li, but larger Na ions into its graphene layers, allowing it to perform well as a potential anode material for Na ion batteries [94-98]. Because of the lack of ordering between graphene layers in hard carbon, improved transport and rate capabilities were observed, therefore

lignin-derived carbons were also utilized as supercapacitor or ion capacitor electrode materials [99-102].

1.4.3 Combination of Si and SiO_x-based anode and lignin

Lignin is a candidate structural material in electrodes due to the reasons described below.

Firstly, Si and SiO_x suffer from large volume changes during lithiation and delithiation. A matrix that is highly conductive, flexible, and resistant to volume changes, is highly desired. The pyrolysis of lignin is a complex process where various volatile compounds and a solid residue are obtained after heat treatment [103, 104]. The major gaseous products are methanol, formaldehyde, acetic acid, light hydrocarbons, CO, CO_2, and H_2O. The solid residue consists of polycyclic aromatic hydrocarbons at intermediate temperatures from 150-550 °C and is increasingly devoid of hydrogen and oxygen at higher temperatures. The pyrolysis of lignin is also accompanied by mass loss, and the typical char yield is 40~50% at 600 °C, depending on the heating protocol and lignin type [68]. After heat treatment, lignin leaves behind a well interconnected carbon matrix because lignin is highly cross-linked. This well interconnected carbon matrix should be ideal in hosting Si and SiO_x particles because better connectivity of Si and SiO_x particles could be realized by this interconnected matrix, as compared to carbon matrix formed by pyrolysis of more linear precursors such as polyacrylonitrile. As a natural binder in plants, lignin is also expected to maintain some of its binder properties at a temperature of 500-600 °C. Furthermore, the heating of organic polymers such as lignin would eventually lead to electronic conductivity, allowing for the omission of additional conductive additives. Therefore, the compositing of heat treated lignin and Si can form Si-C composite electrodes with good electronic conductivity and mechanical robustness without the use of additional binders and conductive additive. These properties encouraged me to study Si-C composite electrodes made from lignin.

Secondly, as briefly mentioned above, lignin is under-valorized as an abundant product, as ~95% is directly burnt onsite as fuel. As a renewable source, available in the capacities of 50 million tons per year, it is very rewarding to find applications with high added value. The prices of lignin is also cheap ($150-250/ton, Alibaba) compared to conventional binder such as polyvinylidene ($11600/ton, Alibaba). The use of lignin in synthesizing binder-free Si-C composites can potentially lower the cost of the anode.

1.5 Structure of dissertation

This dissertation is divided into 6 chapters. Chapter 2 describes the performance of a binder-free Si-lignin electrode synthesized at high temperature of 800 °C. Chapter 3 describes the performance of a more generalized model of Si-lignin electrode and shows that the performance could be enhanced with lower heat treatment at 600 °C. Chapter 4 studies the performance of SiO_x particles composited with heat treated lignin and possible reasons for the excellent cycling performance. Chapter 5 is dedicated to the literature research of SiO_x-based anodes in LIBs, because of the importance of SiO_x in development of next generation high capacity LIBs, and because no such comprehensive review was published previously.

Chapter 2 Binder-free Lithium Ion Battery Electrodes Made of Silicon and Pyrolized Lignin

Most of the contents of this chapter is reproduced from the paper published as ref [26], "Chen, T.; Zhang, Q.; Xu, J.; Pan, J.; Cheng, Y.-T., Binder-free lithium ion battery electrodes made of silicon and pyrolized lignin. RSC Adv 2016, 6 (35), 29308-29313."

2.1 Introduction

In this chapter, a binder-free negative electrode for lithium ion battery consisted of renewable biopolymer lignin and nano-sized silicon nanoparticles is demonstrated. By mixing, coating, and subsequent pyrolization, 3-dimensional, interconnected composite films of Si/C directly on the copper current collector was synthesized, allowing for the assembly of coin-cells without the need of polymer binder and conductive carbon. It was found that carbon from pyrolized lignin can provide conductive pathways for electrons and protect silicon nanoparticles from extensive SEI formation by forming a core-shell foam-like 3D network, while bonding the composite film securely onto the Cu current collector. As a result, excellent electrochemical performance was observed with a high specific capacity of 1557 mAh g^{-1}, 89.3% capacity retention over 100 cycles, and good rate performance. A beneficial effect of 0.5% polyethylene oxide (PEO) on the morphology and electrochemical behavior of Si/C composite electrodes was also unveiled.

2.2 Experimental

2.2.1 Fabrication of Si-pLig binder-free electrode

Hardwood Kraft lignin (Lig) was obtained from Mead Westvaco. Kraft lignin was first mixed with 0.5 wt% polyethylene oxide (PEO, $1x10^6$ MW, Sigma Aldrich) by spatula, then the powder mixture was dissolved in dimethylformamide (DMF, Sigma Aldrich) with a weight ratio of 15%. The solution was heated to 60 °C under constant magnetic stirring for 2 h. Afterwards, silicon nanoparticles were added to the solution with a weight ratio of 15% to DMF. The solution was magnetically stirred for 6 h at 60 °C while going through sonication for 5 min, every 2 h. A Mazerustar KK-250 planetary mixer was also used every 2 h to ensure adequate mixing. The solution was stirred and heated until reaching a suitable viscosity for slurry coating onto copper foil by a doctor blade with a thickness of 127 µm. After drying in air, the coated copper foil was dried under vacuum at 120 °C overnight (silicon nanoparticle-lignin composite prior to pyrolization is denoted as Si-Lig) to obtain a uniform Si-Lig film.

The dried Si-Lig on copper foil was pyrolized in a tube furnace with argon atmosphere at a step rate of 2 °C /min up to 800 °C, then held for 2 h (pyrolized Si-Lig is denoted as Si-pLig) and then naturally cooled down. For making electrodes, 10 mm disks were cut and stored to be assembled into coin cells, with an average silicon mass loading of 1.4 mg cm^{-2} (post-pyrolization mass).

For comparison, silicon negative electrode using polyvinylidene fluoride (PVDF, Alfa Aesar) as the binder was prepared using conventional slurry coating method. The mass ratio of silicon, carbon additive (Super C65, Timcal), and respective binder was 3:1:1. PVDF was first dissolved in N-Methyl-2-pyrrolidone (99.5%, Alfa Aesar) solvent, then silicon nanoparticles and carbon black were mixed in the PVDF solution until a uniform slurry with reasonable viscosity was obtained. Finally, the slurry was coated onto copper foil by a doctor blade with a thickness of 127 µm.

2.2.2 Characterization

Scanning electron microscopy (SEM) was performed using a Hitachi S-4300 microscope with a 15 kV voltage in the imaging mode. The structure and morphology of the Si-pLig composite electrode were examined with a JEOL 2010F transmission electron microscope (TEM). The amount of Si in the Si-pLig composite was determined by thermal gravimetric analysis (TGA) (TA Q500 in high-resolution dynamic mode) in the air. The samples were heated to 800 °C at a constant rate of 10 °C/min.

2.2.3 Electrochemical measurement

For electrochemical performance of Si-pLig/Si-PVDF-Super C65 on copper current collectors, coin cells (CR2025 type) were assembled in an argon filled glove box, using Li metal foil as the counter/reference electrode, Celgard 3501 membrane as the separator, and 1M $LiPF_6$ in ethylene carbonate and diethyl carbonate (EC: DEC=1:1 vol%, BASF) with 10 wt% fluoroethylene carbonate (FEC) additive as the electrolyte. Electrochemical tests were performed using a Bio-Logic potentiostat (VMP-3) at room temperature. All specific capacities presented were calculated based on the weight of Si in the composite. TGA analysis was used to determine the weight percent of Si in the Si/C composite.

2.3 Results and discussions

The concept of Si nanoparticle/pyrolized lignin composite (Si-pLig) is shown in Figure 2.1(a). A by-product of paper and pulp industry, lignin commonly from tree wood is commercially available as fine powder. Prior to pyrolization, Si nanoparticles are uniformly dispersed and coated with the heavily cross-linked lignin while lignin also formed a 3D matrix surrounding the Si nanoparticles.

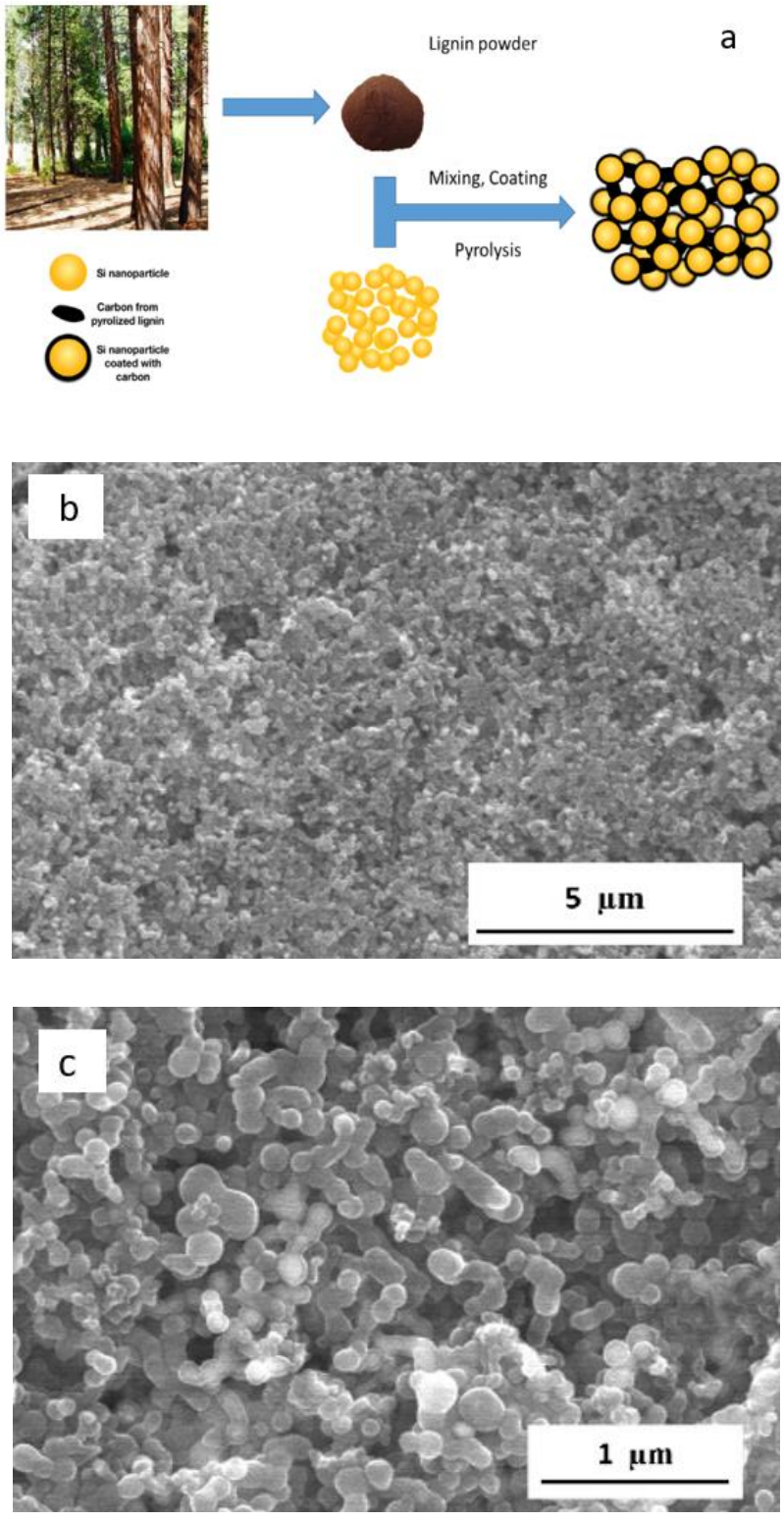

Figure 2.1. (a) Schematic illustration of Si nanoparticle-pyrolized lignin composite (Si-pLig). (b) SEM image of Si-pLig with PEO. Scale bar, 5 µm. (c) SEM image of Si-pLig with PEO at lower magnifications, scale bar 1 µm.

Upon pyrolization in an inert gas atmosphere, lignin is carbonized leaving behind a porous carbon network with graphitic and non-graphitic domains of high electronic conductivity surrounding Si nanoparticles [105]. Figure 1(b) shows a scanning electron microscopy (SEM) image of the Si-pLig composite, with coated Si nanoparticles mostly in the size range of 110-170 nm diameter connected by the carbon network derived from pyrolized lignin. Kubo and Kadla found that the addition of up to 1% PEO to lignin blends greatly increased the thermal mobility and spinnability while decreasing the rigidity of lignin during either thermal extrusion or electrospinning [106, 107]. In my case, there is also a marked difference between Si-Lignin composites with and without 0.5% PEO, as shown in Figure 2.1(c) and Figure 2.2, respectively. Si-pLig with PEO appeared as uniform foam-like 3D network with voids, while without PEO Si nanoparticles were embedded in a rigid carbon matrix. Large fibers/spheres observed on the surface layer was identified to be carbon fibers/spheres from pyrolized lignin, likely because the surface conditions during DMF evaporation were similar to that in electrospinning from lignin/DMF solution which resulted in the formation of sphere/bead/fiber morphology [69]. The morphological difference between the samples was also reflected in the electrochemical performance as shown later in this report. The Si-pLig composite electrode also showed excellent adhesion to Cu substrate even after 120 cycles, as shown from the cross-section SEM image in Figure 2.3.

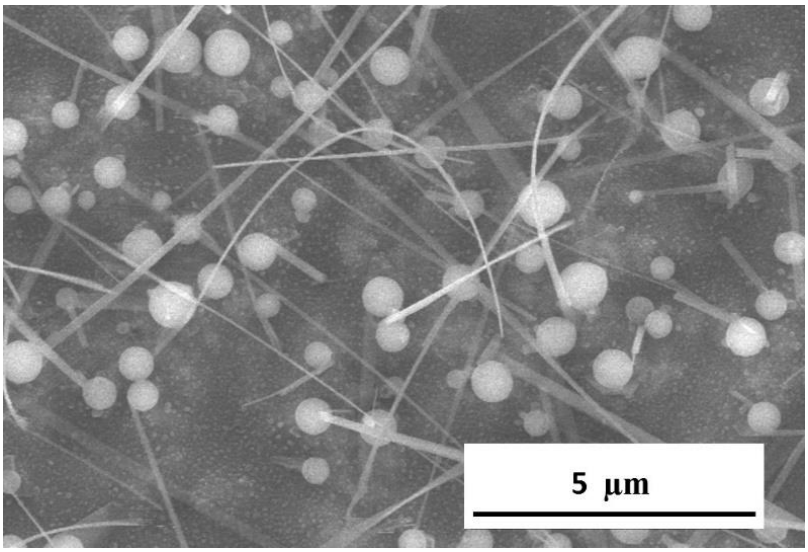

Figure 2.2. SEM image of Si-pLig without PEO addition.

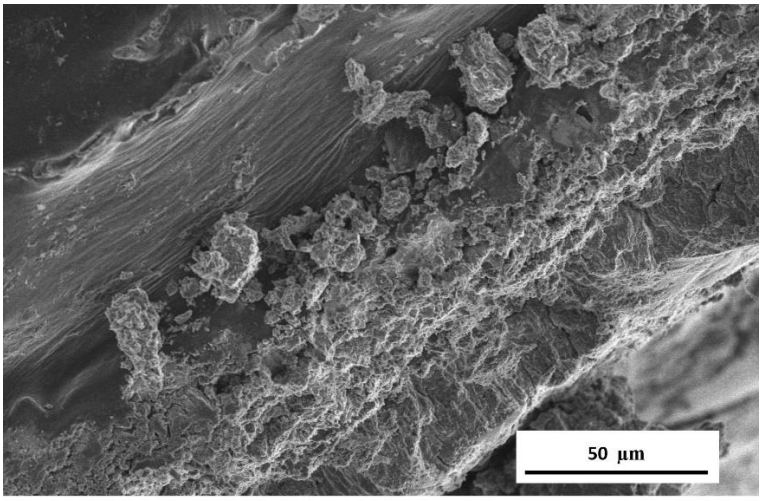

Figure 2.3. Cross-section SEM image of Si-pLig with PEO after 120 cycles.

Transmission electron microscopy (TEM) images shown in Figure 2.4(a) support the hypothesis that Si nanoparticles were not only interconnected but also encapsulated by pyrolized lignin. A core-shell structure with 120 nm diameter Si nanoparticle and amorphous graphite coating of about 20 nm thickness were observed. Yolk-shell Si-pLig particles were also observed throughout the composite film as shown in Figure 2.4(b). The observed yolk-shell particle formation in the composite may be explained by the fact that pyrolization char yield of hardwood

Kraft lignin is typically 50% leading to substantial lignin network volume reduction and contraction [68]. It has been shown that the yolk-shell structure could greatly enhance capacity retention in Si-based lithium ion battery electrodes because it could better accommodate volume changes during lithiation and de-lithiation [104]. The composite core-shell structure was further confirmed in Figure 2.4(c), where on the top right side an amorphous graphite layer of ~20 nm thickness was observed, and on the bottom left side crystalline silicon was identified with a crystal lattice of 0.313 nm [(111) face] [108].

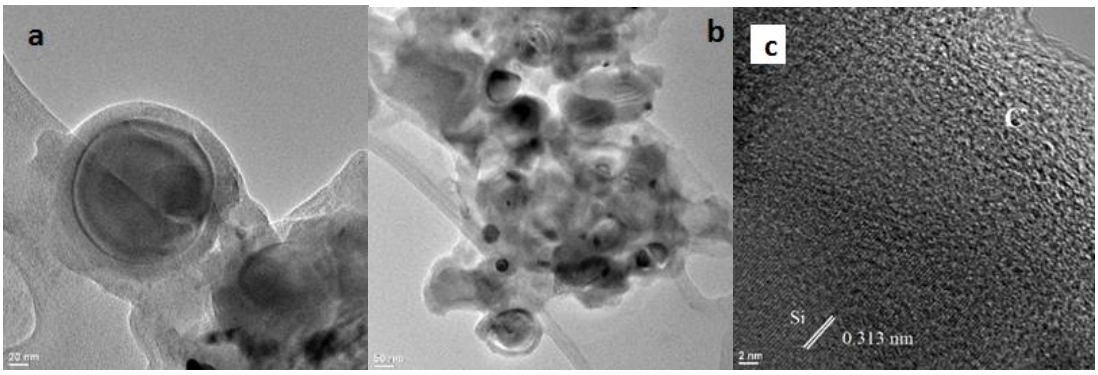

Figure 2.4 TEM images of as synthesized SiNP/pyrolized lignin composite (Si-pLig). (a) High magnification TEM. (b) Lower magnification TEM image of a bundle of Si nanoparticles. (c) Detailed TEM image of a Si nanoparticle coated by amorphous carbon. The crystal lattice 0.313 nm of Si (111) face is marked in the TEM image.

Thermogravimetric analysis (TGA) was performed to determine the weight percent of Si in the Si-pLig composite, shown in Figure 2.5(a). The initial monotonic mass decrease in the range of 400-600 °C was mainly due to oxidation of lignin and the mass increase after 600 °C due to oxidation of silicon in air, similar to previous reports [109, 110]. For a starting Si/lignin composite with Si nanoparticle weight composition of 50%, the resulting Si/SiO_x wt% after pyrolysis was 54.7%. This was lower than the expected 66.7%, which is reasonable due to possibly incomplete pyrolization of lignin and the formation of thin SiO_x layer at Si surface. In this report 50 wt% initial Si nanoparticles was chosen based on optimal results from previous publication, which also have shown that various Si/C ratios could be achieved by varying starting

conditions, resulting in different specific capacities [109]. This is one of the interesting areas I would like to study further in the future in order to optimize the performance of Si-pLig composite electrode.

The structure of the Si-pLig composite was analyzed by X-ray diffraction (XRD) and shown in Figure 2.5(b). A broad peak between 15 ° and 25 ° can be attributed to amorphous carbon obtained from pyrolized lignin and possibly SiO_2 amorphous peak upon comparison (JCPDS card number 29-0085). This shows that under a low temperature of 800 °C lignin was pyrolized primarily into an amorphous or hard carbon form [111]. It can also be seen that silicon nanoparticles retained their crystallinity in the composite by comparison with crystalline silicon diffraction pattern (i.e., JCPDS #27-1402).

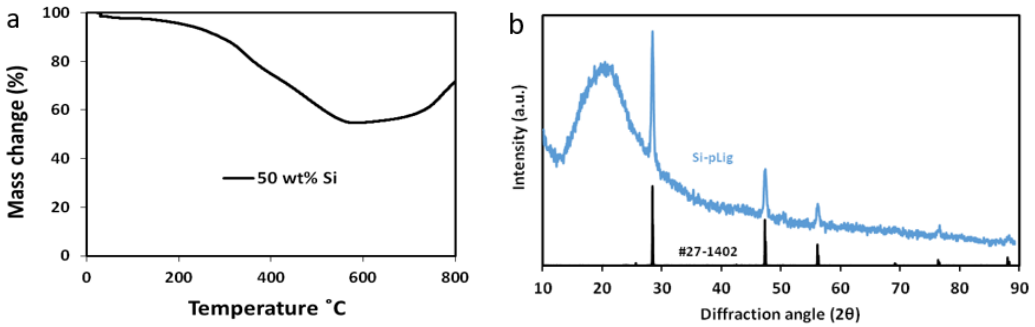

Figure 2.5. (a) XRD diffraction pattern of Si-pLig composite compared with standard silicon crystal XRD pattern. (b) Thermogravimetric analysis (TGA) result of the composite with 50 wt% starting silicon nanoparticle prior to pyrolysis.

Figure 2.6(a) shows the potential profile of the first 4 cycles of Si-pLig at a rate of 0.54 A g^{-1}. The initial charge (lithiation) and discharge (delithiation) capacities for the composite were 1747 mAh g^{-1} and 1251 mAh g^{-1} respectively, with a coulombic efficiency (CE) of 71.6%. The irreversible capacity loss could be attributed to the formation of a SEI on the surface of the electrode at 0.6-0.9 V [112]. Although the CE in the 1st cycle is unimpressive, discharge capacity increased with progressive cycling while the CE increased to 98.1% at cycle 4, likely due to

surface activation or stabilization commonly observed in Si-C composite electrodes [103, 113]. The onset of the silicon lithiation potential long plateau at 0.12 V in the 1st cycle, which is different from cycles 2-3, is indicative of lithiation of crystalline silicon, which is understood because Si nanoparticles are crystalline as shown in TEM observations in Figure 2.4(c) [25] and XRD in Figure 2.5(a).

Long term cycling and rate performance of the Si-pLig composite electrode are shown in Figure 2.6(b). With the initial discharge capacity at 1251 mAh g^{-1}, it gradually increased over progressive cycling until reaching the highest capacity of 1557 mAh g^{-1} at 25th cycle. The discharge capacity at the 100th cycle is 1391 mAh g^{-1}, a remarkable 89.3% capacity retention calculated against the highest capacity and an average cycling efficiency of 99.8% (Si-pLig CE) over 100 cycles. In contrast, the Si nanoparticle electrode with traditional PVDF binder as control (Si-PVDF) started at a high discharge capacity of 1732 mAh g^{-1}, but quickly dropped to 25% at the 10th cycle and lost value during further cycling. Additionally, the Si-pLig composite electrode displayed excellent rate capabilities as shown in Figure 2.6(c). The average capacity based on the mass of Si is 1587 mAh g^{-1} at 0.18 A g^{-1} after initial stabilization, 1626 mAh g^{-1} at 0.36 A g^{-1}, 1475 mAh g^{-1} at 0.72 A g^{-1}, and 1133 mAh g^{-1} at 1.44 A g^{-1}. When the current density is returned to 0.18 A g^{-1}, the discharge capacity recovered to previous levels.

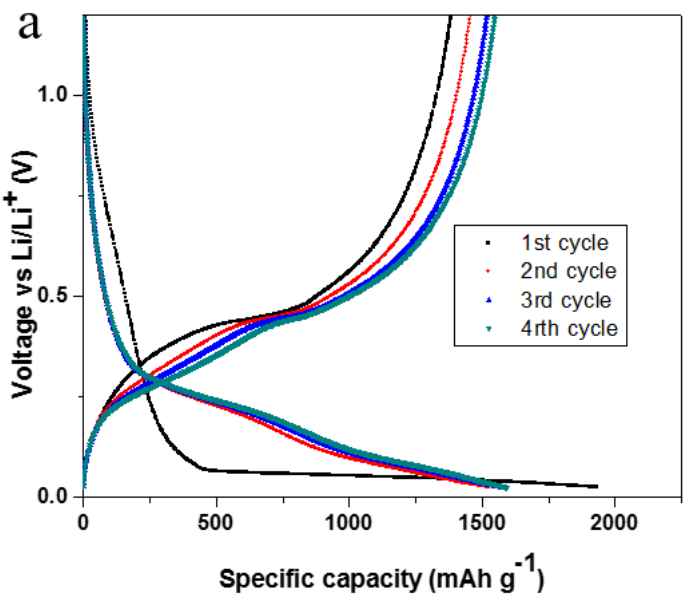
a
1.0
0.5
0.0
Voltage vs Li/Li+ (V)
0
500
1000
1500
2000
Specific capacity (mAh g-1)
1st cycle
2nd cycle
3rd cycle
4rth cycle

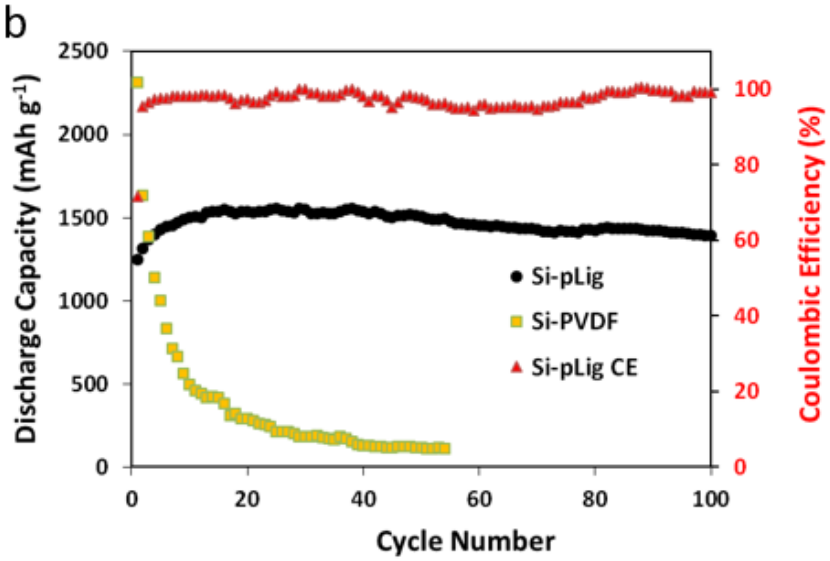
b
2500
2000
1500
1000
500
0
Discharge Capacity (mAh g-1)
100
80
60
40
20
0
Coulombic Efficiency (%)
0
20
40
60
80
100
Cycle Number
Si-pLig
Si-PVDF
Si-pLig CE

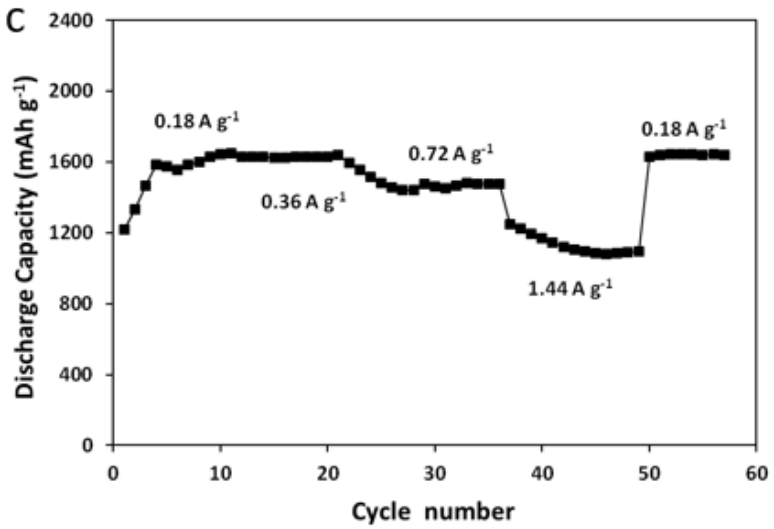

Figure 2.6. (a) Charge-discharge profile of Si-pLig for the first 4 cycles, under 0.54 A g^{-1} rate. The current density was based on the weight of silicon component. (b) Long term cycling performance and Coulombic efficiency of Si-pLig electrode at rate of 0.54 A g^{-1}, in comparison with Si-PVDF binder electrode. (c) Rate capability of Si-pLig electrode.

The exceptional electrochemical performance of the Si/C composite electrode may be understood based on the following considerations. First, carbon network obtained from pyrolized lignin acted as a mechanical support that encapsulated Si nanoparticles and provided good electrical conductivity; Secondly, carbon is known to be an excellent matrix for accommodating mechanical stress from volume changes in the lithiation/delithiation of Si, thus improving the cycling performance [28].

To study the mechanism of capacity loss during cycling, the electrochemical resistance of Si-pLig was measured by electrochemical impedance spectroscopy (EIS), with results shown in Figure 2.7(a). The impedance of the Si-pLig composite dropped dramatically after initial cycling which coincided with the capacity increase shown in Figure 2.6(a). This may be attributed to the activation process observed in Si-C composite materials [114]. Although impedance slowly increased during cycling from cycle 4 to cycle 24 and cycle 104, the impedance of the Si-pLig

composite was still smaller than it was before cycling. This indicates that the continuous capacity loss is not due to worsened kinetics but probably due to mechanical degradation and detachment of the composite, providing a direction for future improvement. The internal impedance of the cell could be described using the proposed equivalent circuit shown in Figure 2.7(b). In the equivalent circuit, R_S is the resistance associated with the cell components such as electrolyte, the working electrode, and reference electrode. R_{int} is the interface resistance related to the SEI, R_{ct} is the charge-transfer resistance, and W is the Warbug impedance element. Due to the porous structure of the Si-pLig composite electrode, the capacitor component in the equivalent circuit was replaced by the constant phase element[115]. The experimental impedance values fitted well with the equivalent circuit.

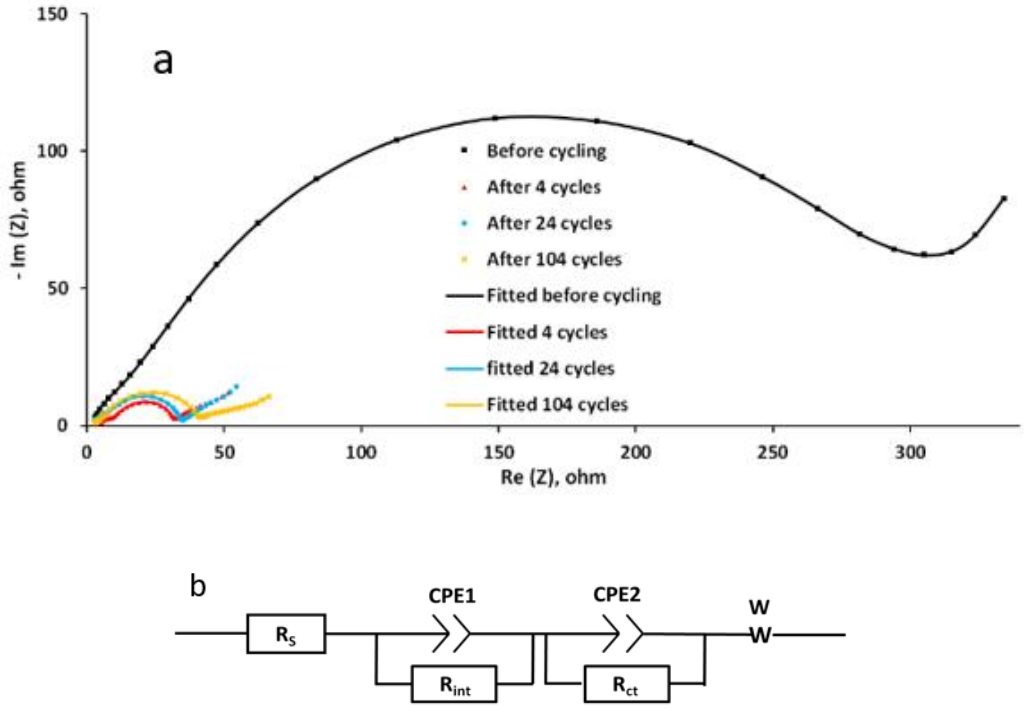

Figure 2.7. (a) Electrochemical Impedance Spectroscopy (EIS) of Si-pLig before and after cycling. The original data was plotted in symbols and the fitted line plotted in coloured lines, respectively. (b) Diagram of equivalent circuit.

Additionally, it is important to point out the effects of PEO addition during the composite electrode synthesis. As shown in Figure 2.2, without the 0.5 wt% PEO addition into the Si-Lig solution prior to pyrolization, Si precipitated from lignin matrix and a non-uniform composite electrode was formed. This expectedly resulted in poor electrochemical performance when it is compared to Si-pLig w 0.5% PEO, shown in Figure 2.8. As seen in Figure 2.8, discharge for Si-pLig w/o PEO started at 1.1 V and continued to 0.025 V, indicating rather significant SEI formation which deviated from typical discharge profiles of lithiation of crystalline silicon. This was also reflected in the low irreversible capacity of the first cycle, which we assigned to the poor contact between lignin and silicon without PEO to act as a "binder". The capacity of the Si-pLig w PEO after the first charge/discharge cycle was approximately 7 times higher than the Si-pLig w/o PEO.

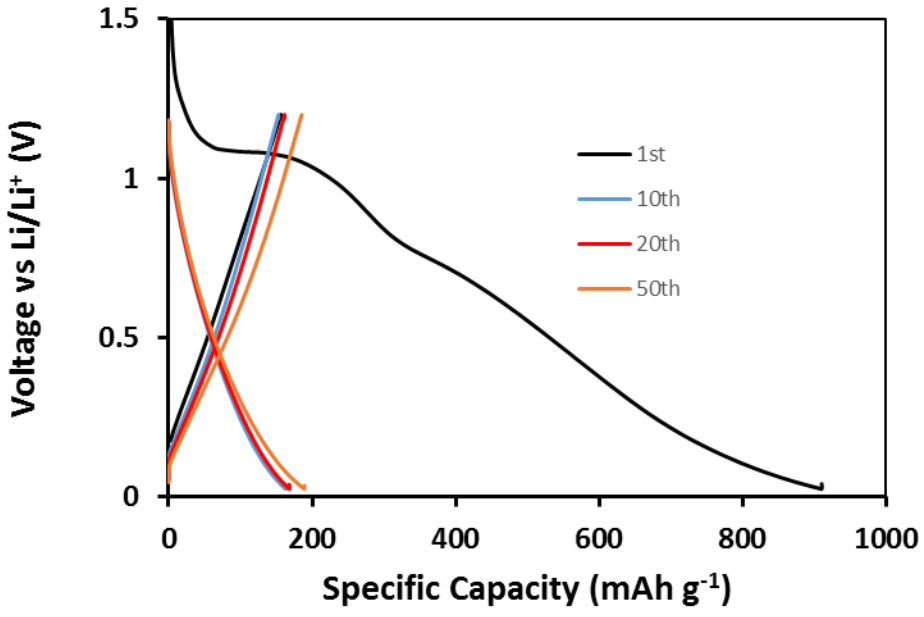

Figure 2.8. Voltage profile for Si-pLig without 0.5% PEO.

In Figure 2.9 the charge and discharge capacity of Si-pLig w/o PEO was shown over 100 cycles. The charge capacity of Si-pLig without PEO addition was less than 300 mAh g^{-1} in the

first few cycles, much lower than the Si-pLig samples prepared with PEO, although it slightly increased over continuous cycling possibly due to activation mechanism discussed previously. Combined with the SEM images, it is concluded that the addition of 0.5 wt% PEO ($1x10^6$ molecular weight (MW)) was crucial to form a backbone framework for the lower molecular weight lignin (average MW 20,000-30,000) and eventual formation of foam-like Si-pLig composite. Without the addition of 0.5 wt% PEO low molecular weight lignin molecules were unable to uniformly coat Si particles prior to and during pyrolization, which resulted in detrimental SEI formation on Si nanoparticles. Judging from the low discharge and charge capacity contribution from Si I believe that many Si nanoparticles were disconnected from the carbon matrix. The beneficial effect of PEO on improving spinnability of lignin into carbon fiber network was studied by Kadla *et al*., which could also be used to explain the present phenomenon since in both cases the desire was to form an ordered interconnected morphology[68, 69, 116]. I believe two reasons may account for the marked difference: 1) PEO is known to greatly promote hydrogen bonding along with other intermolecular and intra-molecular forces between lignin blends thus increasing the viscosity of Si-Lig composite which helps maintain the microstructure during heat treatment. 2) Enhanced Si nanoparticle-lignin hydrogen bonding interactions between the hydroxyls on Si surface and carboxylates formed during lignin heating allow for better encapsulation of Si nanoparticles [117].

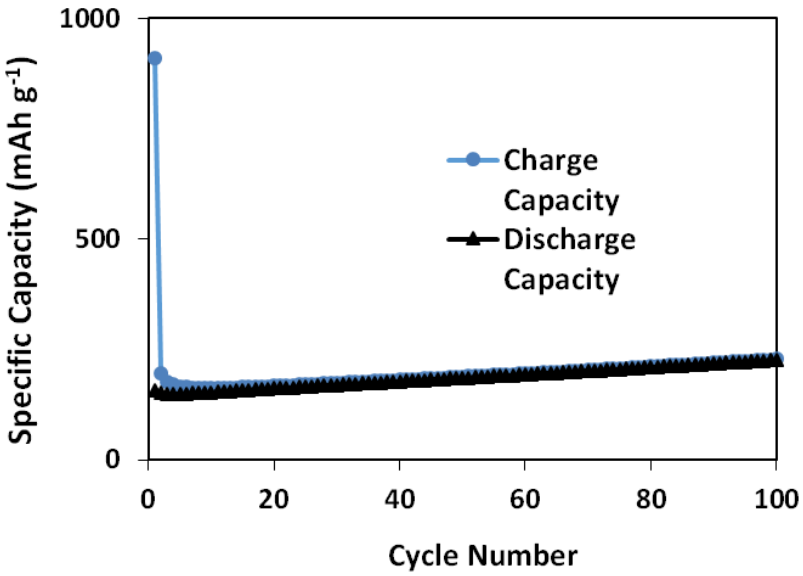

Figure 2.9. Charge and discharge capacity of Si-pLig without 0.5% PEO. Cycling rate was 0.54 A g^{-1}.

2.4 Conclusions

It is demonstrated that low-cost and renewable lignin could be composited with Si nanoparticles to form electrodes that exhibit high specific capacity during lithium charge/discharge cycles, with performance comparable to some of the recent publications on silicon nanoparticle electrodes [39, 102, 118-120].

My current work is important in two aspects: 1) The use of lignin as a renewable and low cost precursor for fabricating high performance Si electrodes for lithium ion batteries; 2) Pyrolized lignin with high molecular weight PEO as a backbone forms a binder free matrix with excellent electronic conductivity, ionic conductivity, and adhesion, thus removing the need for conventional binders such as PVDF. Although lignin has been previously explored for use in sodium ion batteries [121] and spun into carbon fibers (CF) as active material/support for lithium ion batteries [93, 122, 123], this is, to the best of my knowledge, one of the first reports in using

lignin as a precursor to form Si-C composites for lithium ion batteries with performances comparable to other Si-C reports [112, 124, 125]. There are variables not explored in this current work which may further enhance the performance of Si-pLig composite electrodes, such as optimizing Si-Lig ratio, Si nanoparticle size, pyrolization temperature/time, and PEO concentration/weight percent. It is believed that the low cost, renewability, and environmental friendliness associated with lignin and cost reduction by omitting binders will stimulate more interest in utilizing lignin and other biopolymers in energy related research.

Chapter 3 Low-Temperature Treated Lignin as Both a Binder and a Conductive Additive for Silicon Nanoparticle Composite Electrodes in Lithium-Ion Batteries

Most of the contents of this chapter is reproduced from the paper published as ref [126], "Chen, T.; Zhang, Q.; Xu, J.; Pan, J.; Cheng, Y.-T., Binder-free lithium ion battery electrodes made of silicon and pyrolized lignin. RSC Adv 2016, 6 (35), 29308-29313."

3.1 Introduction

The demand for higher energy density and low cost lithium ion batteries is ever increasing as market and policies promote the proliferation of electric vehicles[8, 127]. Currently, graphite is the mainstay negative electrode material for commercial lithium ion batteries, delivering a theoretical specific capacity of 372 mAh g^{-1}. Alternative materials such as pure lithium metal electrode and graphene are being developed [128, 129], although they all face serious challenges. Silicon is one of the promising negative electrode materials with the theoretical capacity of 4200 mAh g^{-1}, more than 10 times higher than that of graphite [130]. While silicon negative electrodes boast the advantages of high theoretical capacity, low lithiation/delithiation potential, and natural abundance, bulk silicon suffers from large volume change (300%) and pulverization leading to its ultimate failure well short of a few hundred cycles that is considered bare minimum for replacing graphite [25, 131]. A number of strategies have been studied to accommodate silicon volume expansion, including the development of binders [132, 133], dispersion of silicon in inactive/active composites [38, 114, 124, 133, 134], and devising of novel nanostructures [109, 135-137]. Among these approaches, silicon-carbon (Si-C) based composites are especially promising because carbon is comparatively flexible, electronically conductive, and easy to obtain

[28, 103]. Silicon and carbon materials have been composited through a number of methods, e.g., electrospinning, ball-milling, coating, and chemical self-assemblies [103, 123-125, 138, 139]. Although these methods have improved the performance of silicon negative electrodes considerably, they introduced, in some cases, complicated synthesis steps which made the composites uneconomical or inactive components which reduced energy density of the composite electrodes.

It is believed that simple synthesis steps that utilized renewable materials without inactive components are important for developing practical silicon based electrodes. Low cost and renewable lignin, which constitutes up to 30% dry mass of the organic carbon on earth, is widely available from paper and pulp mills which produced in excess of 50 million tons annually [140]. Generally burnt for energy on site, lignin is gradually finding its way into high value-added products [141]. For example, Kadla *et al*. used lignin as the precursor for making carbon fibers [68]. Tenhaeff *et al*. fabricated lignin into robust lignin fiber mats for lithium ion battery negative electrodes [93]. Recently, lignin has also been composited with pitch as the precursor for efficient sodium ion batteries [97]. Aside from being a by-product of paper and pulp industry, lignocellulosic mass for the renewable fuel industry is forecasted to reach the annual production of 60 million tons by 2020 as mandated by the US Environmental Protection Agency (EPA) [142]. With such a high abundancy, it is critical and profitable to find high value-added products for lignin to improve the renewable bio-resource landscape. It is proposed that lignin is a competitive additive for making high performance silicon based lithium ion battery negative electrodes.

Previously, it was shown that a heat treatment process at 800 °C would convert a silicon-lignin slurry to a binder-free Si-C composite electrode with high and stable electrochemical performance in which the lignin acted as both the conductive agent and binder [26]. However, the

high temperature treatment resulted in suboptimal utilization of silicon possibly due to the rigid structure of the lignin-derived carbonaceous network. To further improve the cyclability and utilization of silicon nanoparticles, it is explored in this section, a low-temperature heat treatment of the silicon-lignin composite, similar to a low-temperature treatment of Si-cyclized polyacrylonitrile (PAN) approach by Piper *et al.* [67]. They showed that by limiting the pyrolysis temperature to 300-500 °C, the cyclization of PAN proceeds without carbonization, thus maintaining polymeric properties while still introducing delocalized sp^2 π bonding for electronic conductivity. On lignin molecules there exist an abundance of various chemical moieties such as methoxyls, phenols, and hydroxyls while lignin itself is a cross-linked biopolymer with binder-like properties and usages [143]. It is speculated that, at intermediate heat treatment temperatures of 400-600 °C, lignin could be sufficiently carbonized providing excellent electronic conductivity via localized sp^2 π while maintaining some of its polymeric flexibility, allowing the composite to fully utilize silicon capacity and accommodate volume expansion. To test my hypothesis, scanning electron microscopy (SEM) was used to show that the Si-Lig composite was very robust and stable after a high number of cycles. Transmission electron microscopy (TEM) showed that silicon nanoparticles were uniformly dispersed and coated by a thin layer of amorphous carbon acting as a protection layer. Synergistic results of Raman, XPS, and mechanical property measurements by nano-indentation helped explain the chemical composition evolution of lignin during the heat treatment and proved that the Si-Lig composite was sufficiently electronically conductive while being flexible compared to higher temperature treated counterparts. Together these attributes ensured a Si-Lig composite with excellent electrochemical performance.

3.2 Experimental Section

3.2.1 Preparation of Si-Lig composite

Kraft lignin (Indulin AT), supplied by Mead Westvaco as a brown powder, is a purified form of Kraft pine lignin. It is derived by further acid hydrolysis of Kraft lignin, which removes both the sodium and the hemicellulose. The lignin was first mixed with 0.5 wt% polyethylene oxide (PEO, $1x10^6$ MW, Sigma Aldrich) by spatula, then the powder mixture was dissolved in dimethylformamide (DMF, Sigma Aldrich) with a weight ratio of 15%. The solution was heated to 60 °C under constant magnetic stirring for 2 h. Afterwards, silicon nanoparticles of diameters 30-50 nm (Nanostructured & Amorphous Materials) were added to the solution with a weight ratio of 15% to DMF. The solution was magnetically stirred for 6 h at 60 °C while going through sonication for 5 min, every 2 h. A Mazerustar KK-250S planetary mixer was also used every 2 h to ensure adequate mixing. The solution was stirred and heated until reaching a suitable viscosity for slurry coating onto copper foil by a doctor blade with a gap spacing of 127 µm. After drying in air, the coated copper foil was dried under vacuum at 120 °C overnight to obtain a uniform Si-Lig film. The average thickness of the composite film is ~25 µm.

The dried silicon-lignin on copper foil was heat treated in a tube furnace with argon atmosphere at a step rate of 2 °C /min up to 400-600 °C, then held for 10 min. For making electrodes, 12 mm disks were cut and stored to be assembled into coin cells.

3.2.2 Coin cell fabrication and electrochemical testing

For electrochemical performance of silicon-lignin half-cell electrode, coin cells (CR2025 type) were assembled in an argon filled glove box, using Li foil as the counter/reference electrode, Celgard 2400 membrane as the separator, and 1M $LiPF_6$ in ethylene carbonate and diethyl carbonate (EC: DEC=1:1 vol%, BASF) with 10 wt% fluoroethylene carbonate (FEC, BASF)

additive as the electrolyte. A total of more than 20 coin cells made from 3 batches were tested in half cell setups. For full cell NMC ($LiNi_{1/3}Mn_{1/3}Co_{1/3}O_2$, Umicore) electrode replaced the Li metal foil as the cathode electrode. The NMC electrode was prepared using the conventional slurry coating method with a composition of 92 wt% NMC/4 wt% carbon black (Super P C65, TIMCAL/4 wt% polyvinylidene fluoride (PVDF, No. 1100, Kureha, Japan). The average loading and density of the NMC electrode were ~14 mg cm^{-2} and ~1.7 g cm^{-3}, respectively and the loading and density of the silicon-lignin electrode were ~1 mg cm^{-2} and ~0.4 g cm^{-3}, respectively. Masses of the negative silicon-lignin electrode and positive NMC electrode were balanced so that the total capacity N/P ratio of the electrodes was ~1:1. The electrodes were assembled into CR2025 type full cell configuration coin cells and 6 full cells were tested.

Electrochemical tests were performed using a Bio-Logic potentiostat (VMP-3) at room temperature. The electrochemical properties of the electrodes were measured within a voltage range of 0.015-1.2 V using constant current mode. Impedance was measured potentiostatically by applying an AC voltage of 10 mV amplitude in the range of 100 kHz to 100 mHz directly using coin cells after a specific number of cycles. The Si wt% content of the composite was calculated by punching out individual electrodes (12 mm diameter) and weighing the mass loss after heat treatment, where the lignin component lost mass and silicon mass remained constant. The specific capacities of the electrodes were normalized based on the weight of Si in the composite or the total weight of the composite. The mass loading of the silicon-lignin composite electrodes was 0.9 to1.1 mg cm^{-2}, and the Si loading 0.60 to 0.73 mg cm^{-2}.

3.2.3 Characterization

Scanning electron microscopy (SEM) images were recorded using a Hitachi S-4300 microscope with a 6 kV voltage in the imaging mode. The structure of the silicon-lignin composite electrodes

was examined with a JEOL 2010F transmission electron microscope (TEM). X-ray photoelectron spectroscopy was performed on a Thermo Scientific K-Alpha system with Al Kα radiation. Nano-indentation was performed on an Agilent Technologies Nano Indenter G200. The maximum load was 9.8 mN, the loading rate was 0.49 mN/s, and the hold time at maximum load was 10 s. Depth profile (Continuous Stiffness Measurement mode) was studied between 0-3000 nm and average results were obtained for depth either 200-800 nm or 1000-3000 nm where the elastic modulus and hardness were consistent according to Oliver and Pharr [144, 145]. Raman analysis was performed on a Thermo Scientific DXR Raman microscope. Peak analysis was done using OriginPro.

3.3 Results and discussions

The electrochemical performance of silicon-lignin half cells was presented in Figure 3.1. The electronic conductivity of silicon-lignin composite is likely very low after heat treatment at 400 °C leading to almost no capacity. The main transition for the development of electronic conductivity for lignin in my case appeared to be between 400 °C and 500 °C. Figure 3.1(a) shows the initial charge (lithiation) and discharge (delithiation) capacity for silicon-lignin composite treated at 500 °C to be ~3000 mAh g^{-1} and 2330 mAh g^{-1}. Through cycles 2 to 5 capacity gradually increased until the coulombic efficiency (CE) was close to 100%. Figure 3.1(b) shows that the initial charge (lithiation) and discharge (delithiation) capacity for silicon-lignin composite treated at 600 °C is ~3780 mAh g^{-1} and 3086 mAh g^{-1} respectively calculated to the weight of silicon, which corresponds to 2500 mAh g^{-1} and 2050 mAh g^{-1} normalized to the weight of the entire composite electrode. Both electrodes showed a characteristic long plateau during the first lithiation at <0.1 V which corresponds to the amorphization of crystal Si [146].

Long term cycling of silicon-lignin electrodes treated at 500 °C and 600 °C is shown in Figure 3.1(c) and Figure 3.1(d), respectively. At 100 cycles silicon-lignin treated at 500 °C

showed a specific capacity of 2038 mAh g^{-1} normalized to silicon weight or 1386 mAh g^{-1} normalized to the weight of the entire electrode. At 100 cycles silicon-lignin treated at 600 °C showed a specific capacity of 2378 mAh g^{-1} normalized to silicon weight or 1591 mAh g^{-1} normalized to the weight of the entire electrode. Both electrodes demonstrated exceptional cycling properties at relatively high areal loading of ~1 mg cm^{-2} and areal capacity of ~2 mAh cm^{-2}. Compared to excellent capacity retention, the average coulombic efficiency of 98.6% was lower than expected and would be a topic of future improvement. A direct comparison of silicon-lignin composites heat treated at various temperatures is also shown in Figure 3.1(e). It is clear that the 600 °C treated silicon-lignin composite had the best cycling performance. More than 20 coin cells made from 3 batches were tested in half cell configurations and the capacity difference across different coin cells was minimal in the range of ~30 mAh g^{-1} calculated to the weight of silicon. None of the cells failed after a few cycles, showing the consistency and robustness of the silicon-lignin composite.

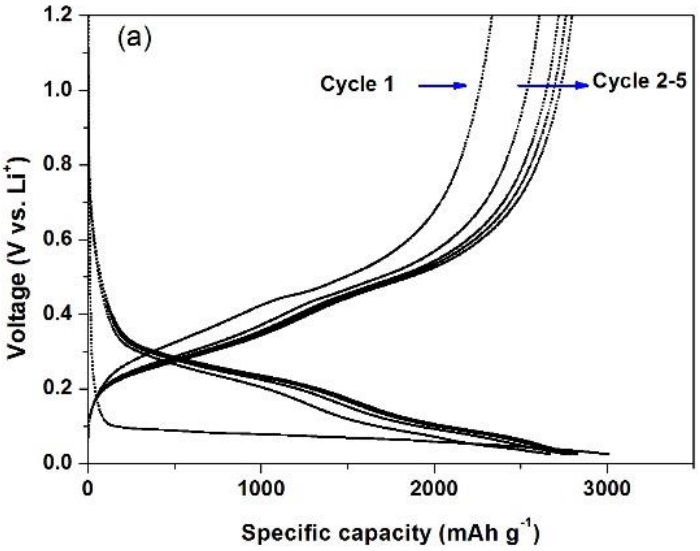
(a)
Cycle 1
Cycle 2-5
Voltage (V vs. Li+)
Specific capacity (mAh g-1)
1.2
1.0
0.8
0.6
0.4
0.2
0.0
0
1000
2000
3000

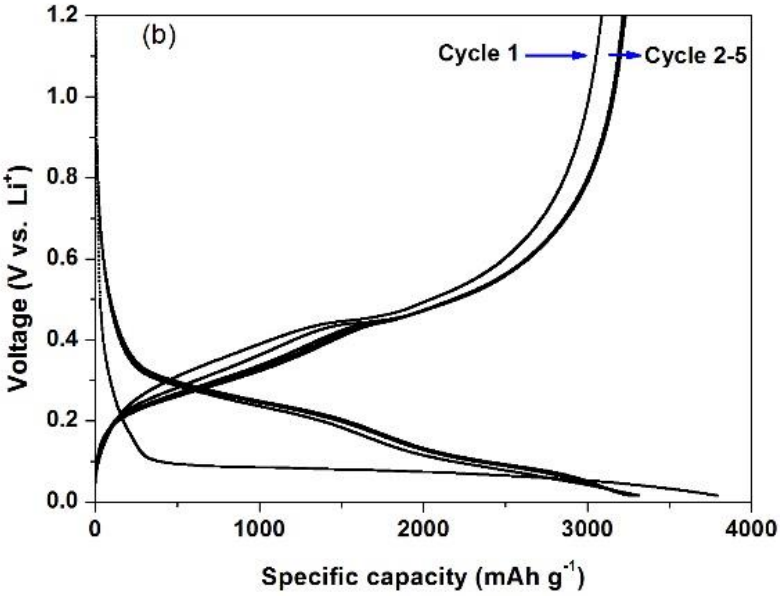
(b)
Cycle 1
Cycle 2-5
Voltage (V vs. Li+)
Specific capacity (mAh g-1)
1.2
1.0
0.8
0.6
0.4
0.2
0.0
0
1000
2000
3000
4000

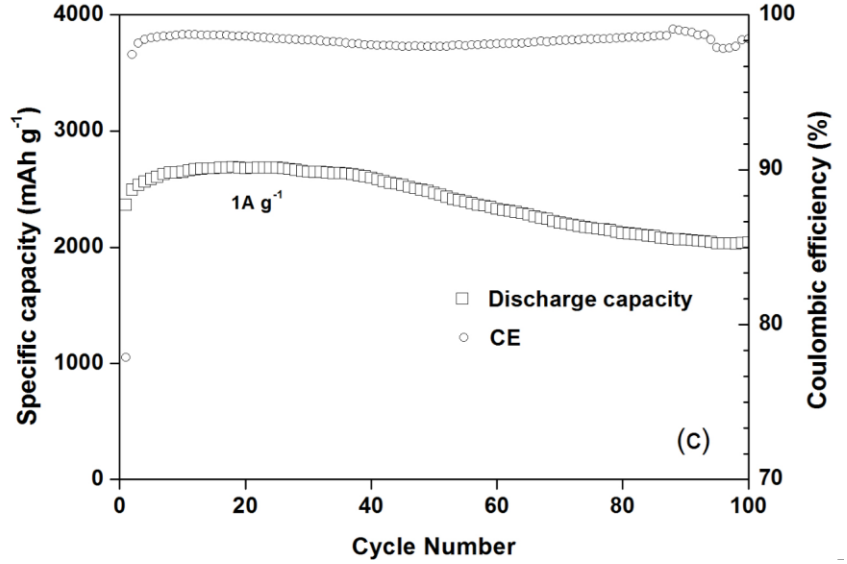
Specific capacity (mAh g-1)
Coulombic efficiency (%)
Cycle Number
1A g-1
Discharge capacity
CE
(c)

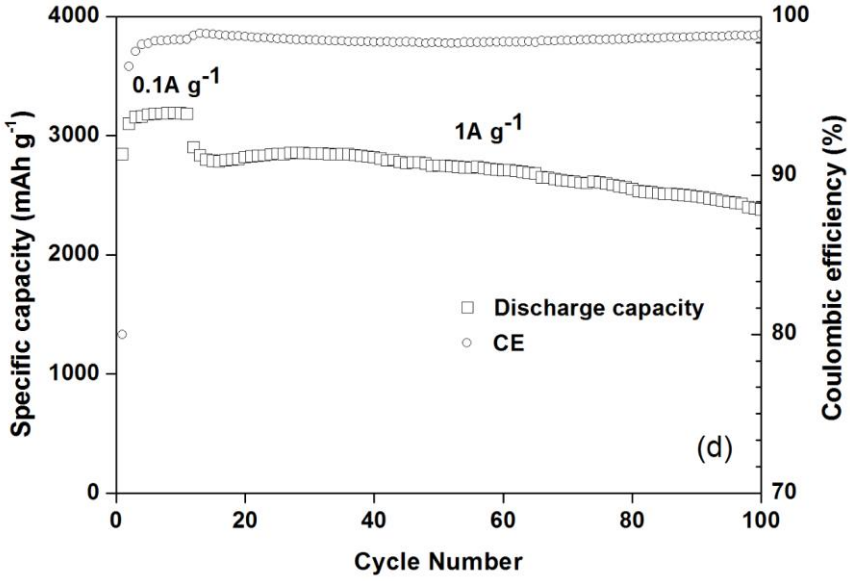
Specific capacity (mAh g-1)
Coulombic efficiency (%)
Cycle Number
0.1A g-1
1A g-1
Discharge capacity
CE
(d)

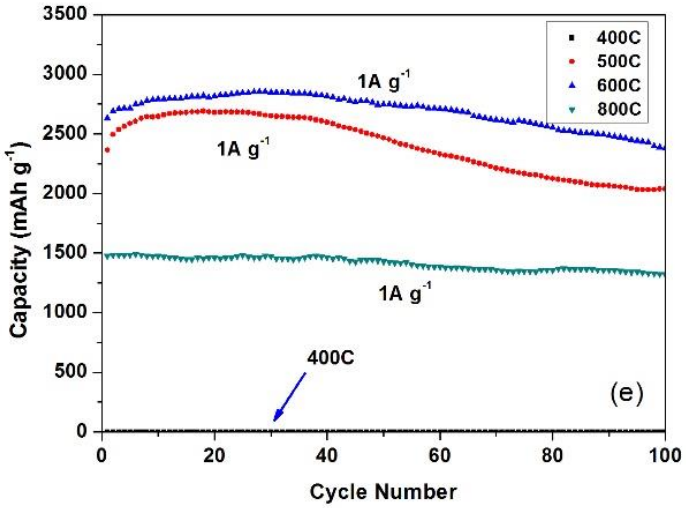

Figure 3.1. Electrochemical performance of silicon-lignin composite in half-cell tests (a) Voltage profiles for silicon-lignin treated at 500 °C. First 7 cycles at rate of 0.1 A g^{-1}. (b) Voltage profiles for silicon-lignin treated at 600 °C. First 5 cycles at rate of 0.1 A g^{-1}. (c) Cycling discharge capability and CE of silicon-lignin composite treated at 500 °C. Cycled at a rate of 1 A g^{-1}. (d) Cycling discharge capability and CE of silicon-lignin composite treated at 600 °C. Cycled at a rate of 1 A g^{-1}. (e) Comparison of silicon-lignin composite cycling capacity treated at 400 °C, 500 °C, 600 °C, and 800 °C.

Rate tests shown in Figure 3.2(a) for silicon-lignin composite treated at 600 °C demonstrated that the composite electrodes showed good performance under high rates and capacity under low cycling rates can be retained. There have been recent reports on the performance of silicon-based electrodes in full-cell setup and it is believed this is critical in evaluating the electrode performance due to the more complex and realistic testing environment [147-149]. Based on the superior performance of the electrode heat treated at 600 °C, it was selected to be coupled with NMC electrode and tested in a full-cell setup with electrochemical performance data shown in Figure 3.2(b) and Figure 3.2(c). The voltage profile is typical of silicon electrode in a full cell setup with NMC electrode and a first cycle coulombic efficiency of 80.1% was obtained. The capacity retention after 60 cycles was 44%, which is similar to most of the silicon-based full-cell performance reported in the literature [147, 149-151], showing that

although many electrodes are very promising in half-cells, the loss of lithium due to parasitic reactions at negative electrode and an unstable solid electrolyte interface (SEI) remains to be an unsolved problem.

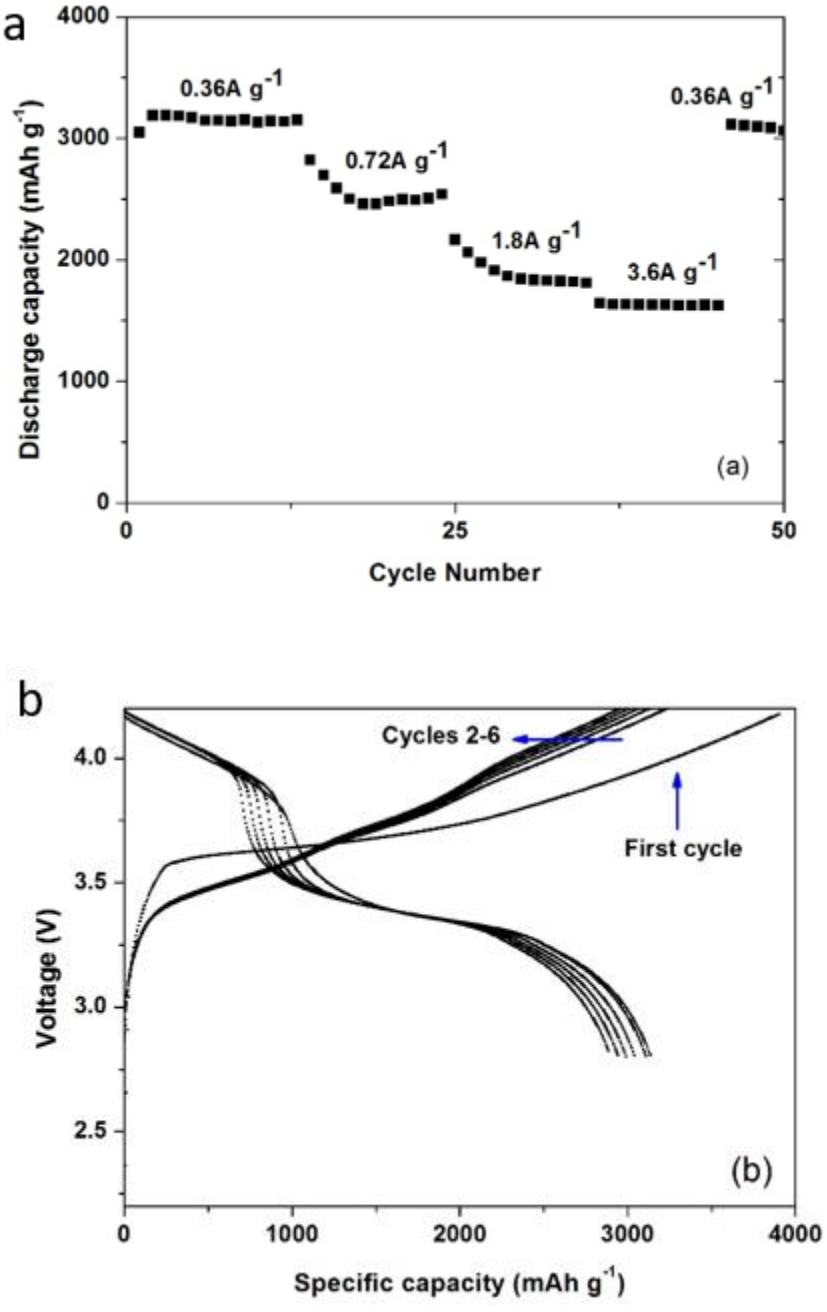

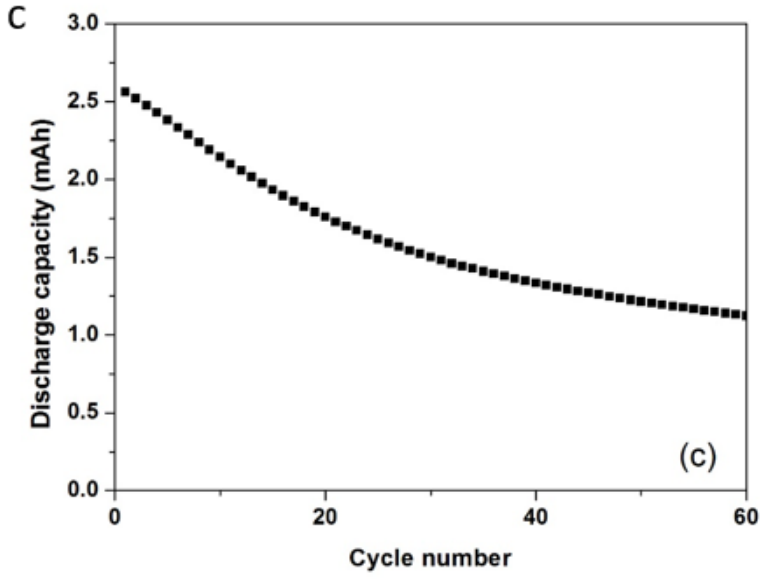

Figure 3.2. Electrochemical performance of silicon-lignin composite (a) Rate capability of silicon-lignin composite half-cell treated at 600 °C. (b) Voltage profiles of silicon-lignin composite treated at 600 °C coupled with NMC positive electrode cycled at 0.1 A g^{-1} between 2.8 V-4.2 V. The rate used and calculated capacity was determined based on the weight of silicon. (c) Cycling performance of silicon-lignin composite treated at 600 °C coupled with NMC positive electrode cycled at 0.1 A g^{-1} between 2.8 V-4.2 V. The rate used was based on the weight of silicon nanoparticles in the composite and the reported capacity is per coin cell.

To help understand the excellent electrochemical performance, the morphology of the silicon-lignin composite was studied by SEM and TEM. Figure 3.3(a) shows a SEM image of the silicon-lignin composite after heat treatment at 600 °C showing that coated silicon nanoparticles are mostly in the size range of 90-170 nm. The size distribution of the individual silicon-lignin particles is due to the varying size distribution of the commercial silicon nanoparticles (40-60 nm), different carbon coating thickness, and possibly bundling of several silicon nanoparticles. The morphology of silicon-lignin composites treated at 400, 500, 600 °C had similar morphology, and the SEM images of 400 and 500 °C composites are shown in Figure 3.4. It is observed that silicon nanoparticles are well connected throughout the 3D matrix provided by the lignin, similar to other silicon composite work [118, 133]. The structure of the silicon-lignin composite is further shown in detail by TEM images. Figure 3.3(b) proves that Si nanoparticles were not only

interconnected but also encapsulated by carbon from heat treated lignin. Figure 3.3(c) shows that the silicon nanoparticles are crystalline in nature with a thin layer of amorphous carbon coating. Post-cycling SEM images shown in Figure 3.5(a) indicates that the structure of the composite is surprisingly robust considering that no conventional binder was used, although some micrometer size cracks were formed due to silicon volume expansion. Overall most silicon nanoparticles maintained electronic conduction to the bulk of the composite after 50 cycles as indicated by electrochemical cycling data. It could also be seen in the SEM image in Figure 3.5(b**)** after 50 cycles carbon coated silicon nanoparticles have increased in size slightly probably due to SEI growth. Figure 3.5(c) also shows that the composite maintained good adhesion to the Cu substrate after 50 cycles, and no significant delamination from the substrate was observed. EDX mapping of shown in Figure 3.6 leads to the conclusion that a thin layer of native SiO_2 also existed on the surface of the silicon nanoparticles as indicated by O signals. Figure 3.7 shows silicon-lignin aggregates after 50 cycles. Crystalline silicon turned into amorphous silicon after reversible lithium insertion and the integrity of the composite was retained [152].

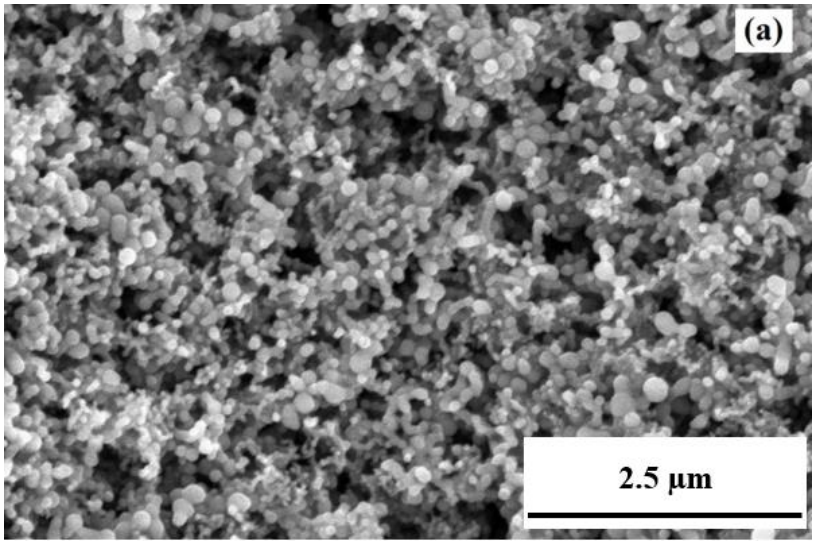

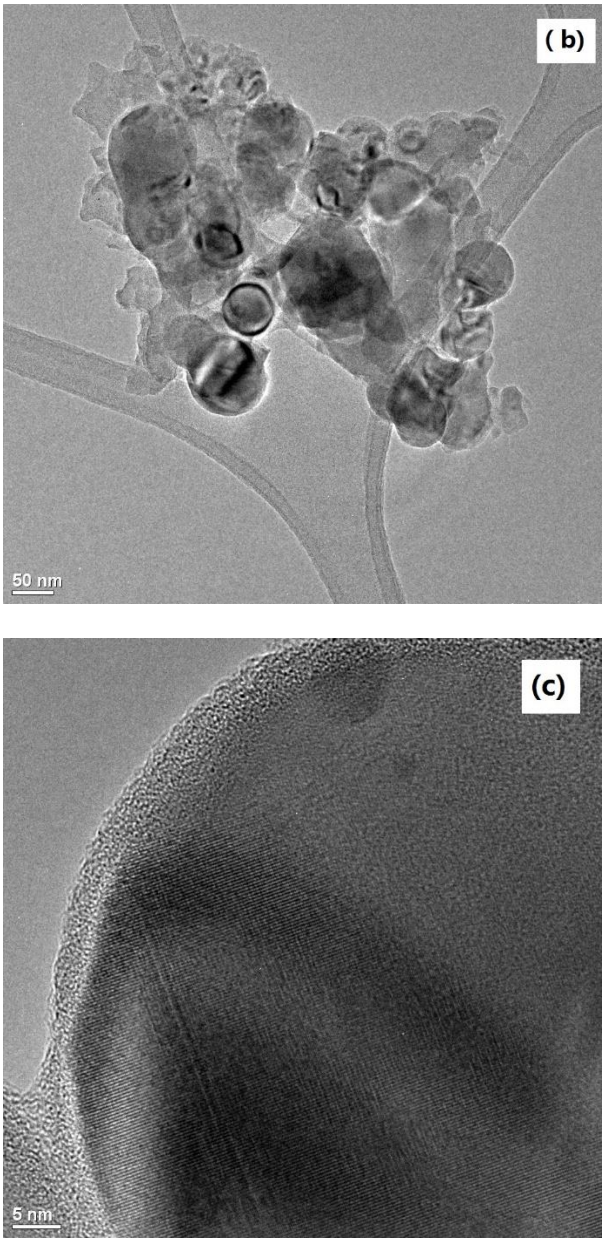

Figure 3.3. (a) SEM image shows the typical surface morphology of silicon-lignin composite after heat treatment at 600 °C. (b) TEM image shows a bundle of coated silicon nanoparticles. (c) HRTEM image of a silicon nanoparticle.

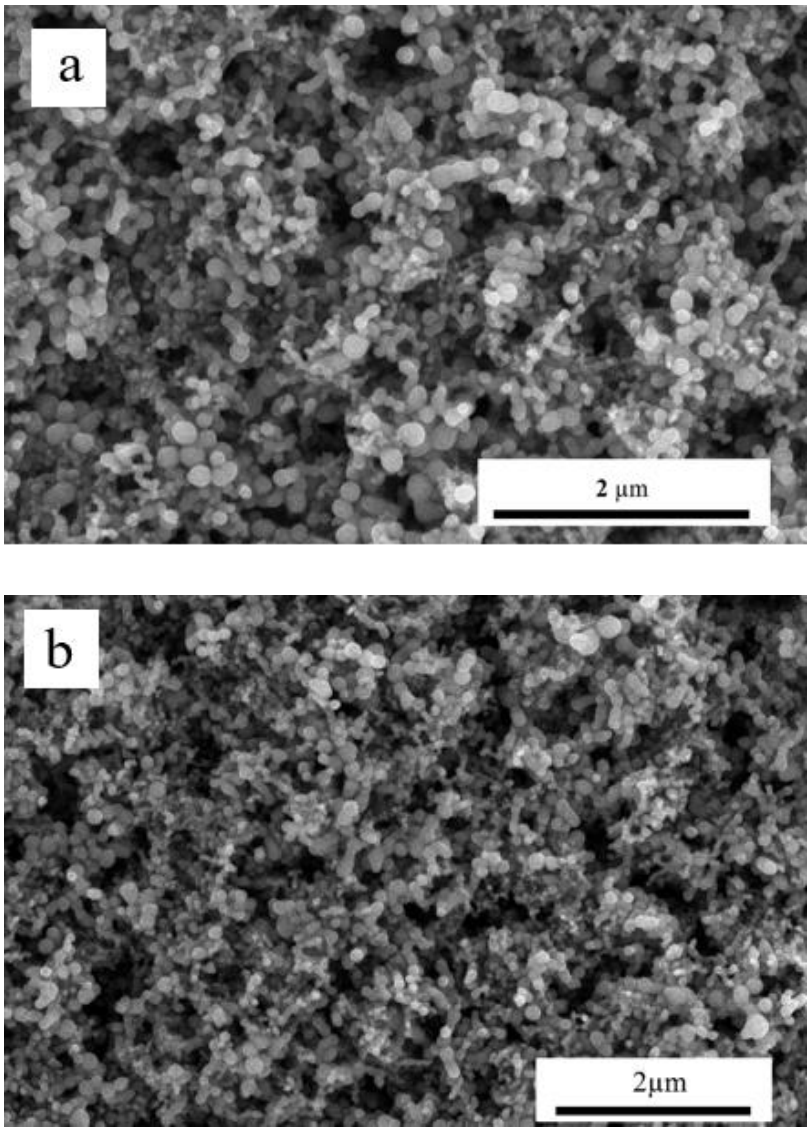

Figure 3.4. SEM images of Si-Lig composites after heat treatment at (a) 400 °C and (b) 500 °C.

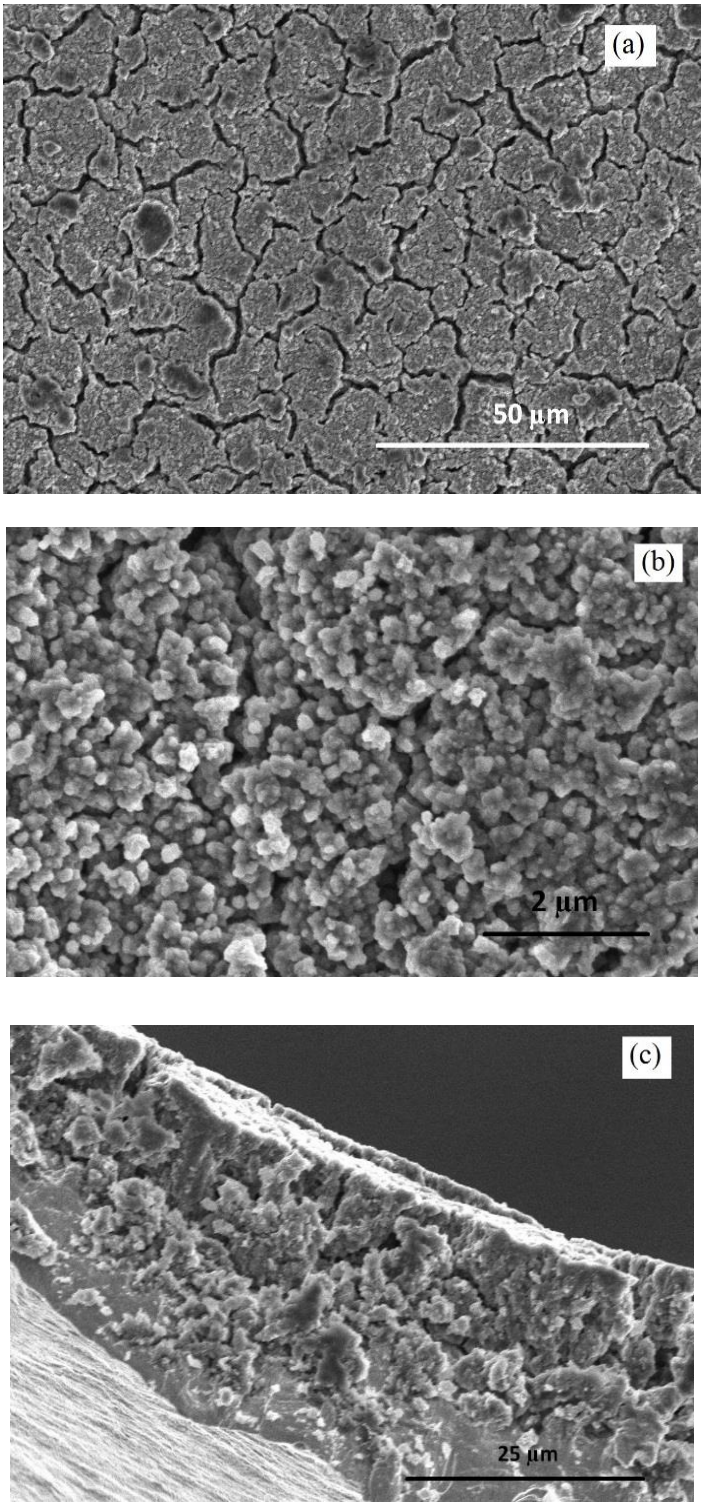

Figure 3.5. Post-cycling SEM images of silicon-lignin composite treated at 600 °C, after 50 cycles. (a) Low magnification top view (b) High magnification top view (c) Cross-section view.

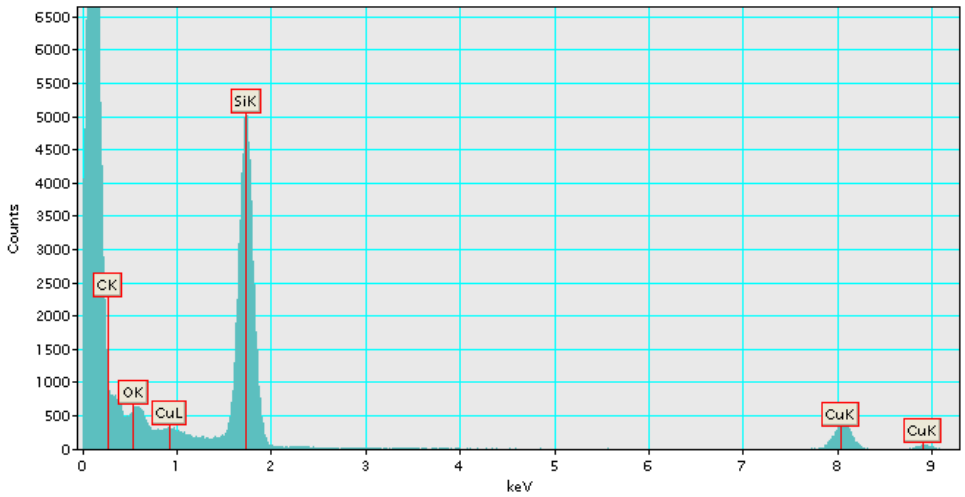

Figure 3.6. EDX mapping of Figure 3.3(c).

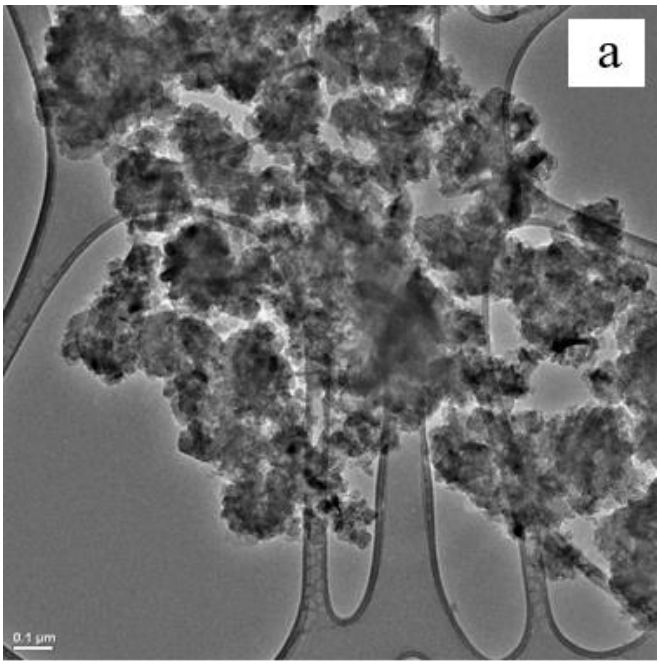

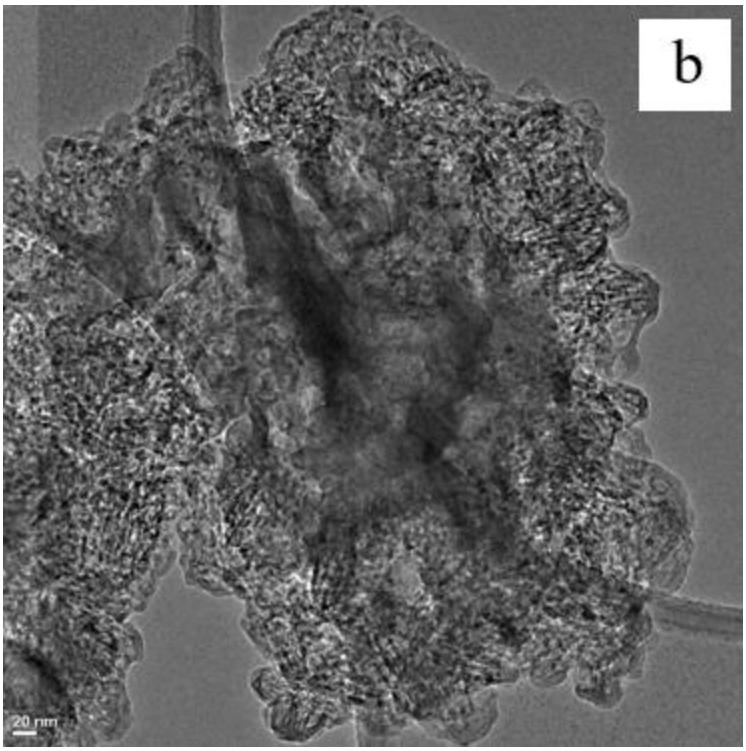

Figure 3.7. TEM images of the Si-Lig electrode after 50 cycles at a rate of 1 A g^{-1} with different magnifications, showing the integrity of the composite.

Although the pyrolytic behavior of lignin has been studied previously, XPS and Raman spectroscopy were used to analyze the chemical composition change in the silicon-lignin composites. Figure 3.8(a) shows the XPS spectra of C 1s from silicon-lignin composites treated at various temperatures. The non-treated Si-Lig displayed a wide band from 282 to 288 eV, with the main peak at ~284.4 eV. The broadening of the band toward lower energies is due to significant C-H bonding, and this broadening decreases with increasing treatment temperature [84]. The 286 eV peak is typically associated with C-O bonds such as hydroxyl and/or ether, and it also decreases substantially toward higher temperatures correlating with the release of H and O containing volatile compounds during pyrolysis. With increasing temperature, the C 1s bands become narrower and are more centered at ~284.7 eV which is related to C-C and C=C bonding. This suggests that over the course of temperature rise H and O moieties were lost substantially

leading to the formation of graphitic domains. There is also a main peak shift from Si-Lig non-treated to Si-Lig 800 °C which is likely due to the size change of condensed aromatics/graphite domains and loss of C-H bonding [153]. The C 1s spectra was deconvoluted mainly considering C-C/C=C and oxidized carbon. The peak area and ratio of C-C/C=C to oxidized carbon peaks were shown in Table 3.1. The monotonic increase in the peak ratio with increasing heat treatment temperature is understood because oxygen is gradually lost during heating up of organic material as gaseous side products.

Table 3.1. The normalized area of deconvoluted carbon peaks and ratio of C-C/C=C peaks to oxidized carbon peaks.

	Peak area (Arbitrary Units)		**Ratio of C-C/C=C to oxidized carbon peaks**
	C-C/C=C	**Oxidized peaks**	
Silicon-lignin composite (Non-treated)	37139	35621	1.0426
Silicon-lignin composite (400 °C)	58664	40015	1.4660
Silicon-lignin composite (500 °C)	52913	30820	1.7168
Silicon-lignin composite (600 °C)	63116	27624	2.2848
Silicon-lignin composite (800 °C)	54321	19560	2.7771

To further understand the ordering of carbons in lignin during heat treatment, Raman data was shown in Figure 3.8(b). There was no Raman shift for the non-treated silicon-lignin composite. For samples treated at 400, 500, and 600 °C two Raman shifts were seen specifically at 1367 cm^{-1} (D band) and 1593 cm^{-1} (G band). These two bands are attributed to delocalized sp^2

π bonding [154]. The appearance of D and G bands correlate to the existence of disordered and ordered structural configurations, respectively, therefore the ratio of band intensities I_D/I_G is indicative of the degree of order of the carbons. Gaussian function was used to fit the peaks with R^2>0.99. The ratios of I_D/I_G were calculated using the fitted peaks and found to be 2.19 for 400 °C, 1.90 for 500 °C, and 1.84 for 600 °C samples. My findings are consistent with the literature that I_D/I_G decreases with increasing heat treatment temperature, implying a higher degree of ordering for carbons [155]. From the characterization results, it is evident that heat treatment at 400-600 °C caused graphitization of lignin, bringing forth electronic conductivity.

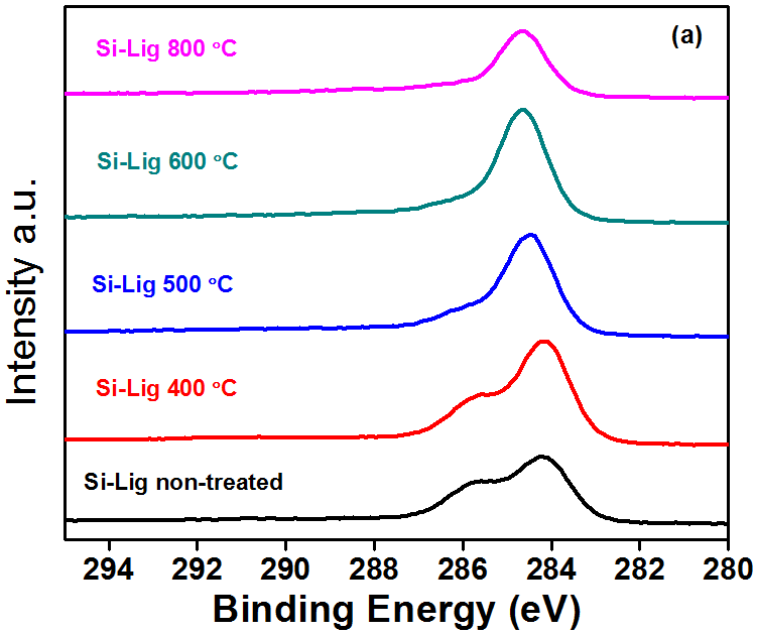

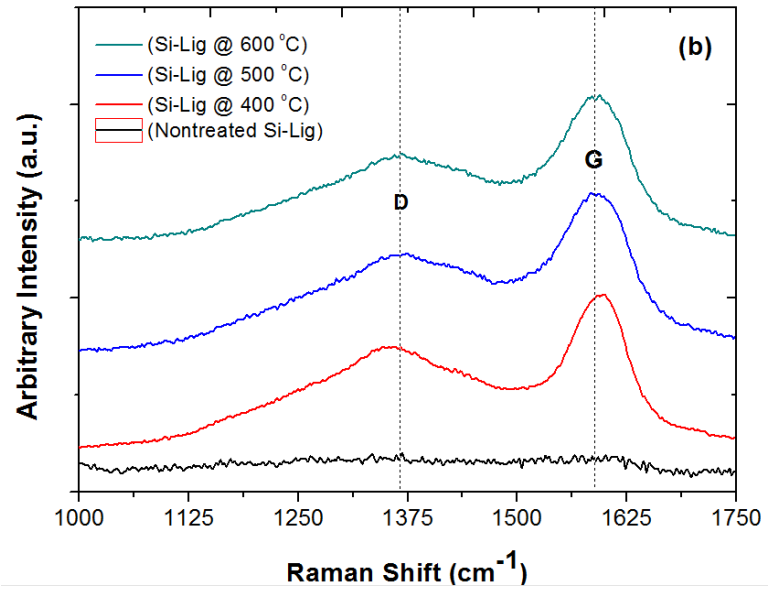

Figure 3.8. (a) C 1s XPS spectra of silicon-lignin composite treated at various temperatures (b) Raman spectra of silicon-lignin composite treated at various temperatures shown with the typical D and G bands.

It is believed that performance of a binder should be dependent on its mechanical properties, in particular elastic modulus and hardness. In the case of silicon nanoparticles, however, there seems to be few studies establishing a correlation between these mechanical properties and the electrochemical performance of a binder. Some previous research has indicated that mechanical properties of binders are one of the key factors in determining their performance [33, 156]. Therefore, detailed nano-indentation measurements were carried out to obtain, in Table 3.2, the mechanical properties of silicon-lignin composites heat treated at two different temperatures. It is found that the modulus of heat treated lignin composited with silicon nanoparticles was much lower than carbon fibers using lignin as a precursor due to difference in configuration and heat treatment protocol. The elastic modulus of lignin without heat treatment is in the range of ~3 GPa and carbon fibers spun from lignin precursor had modulus in the range of 39 to 61 GPa [82, 157]. A notable increase in elastic modulus and hardness is seen for silicon-lignin composites treated at 600 °C compared to 800 °C, which shows a much stiffer composite

was formed due to carbons being more ordered at higher temperatures such as forming graphite-like domains. While this brought an increase in conductivity, it likely decreased polymer-like properties of the composite resulting in lower silicon utilization and volume accommodation ability. These difference in mechanical properties helped explain why silicon-lignin composite treated at temperatures of 600 °C had much improved electrochemical performance over my previous publication where it was treated at 800 °C [26].

Table 3.2. Summary of elastic modulus (E) and hardness (H) for silicon-lignin composites.

	E (GPa)		**H** (GPa)	
	Mean	**S.D.**	**Mean**	**S.D.**
Silicon-lignin composite (600 °C)	6.23	0.72	0.19	0.04
Silicon-lignin composite (800 °C)	16.64	3.73	0.82	0.34

To investigate the electronic conductivity, silicon-lignin composites heat treated at 400, 500, and 600 °C were studied by electrochemical impedance spectroscopy (EIS). EIS measurements for half-cells were conducted during the cycling process and shown in Figure 3.9(a). The EIS plots usually consist of a semicircle at high frequency which represents the resistance of the electrolyte and charge-transfer, and a Warburg tail at lower frequencies due to diffusion-resistance from the electrode material. For the 500 °C electrode the resistance at high frequencies increased over the course of cycling. For the 600 °C cell the resistance at high frequencies did not dramatically change, but the resistance at lower frequencies increased over the course of cycling. An equivalent circuit shown in Figure 3.9(b) was used to fit experimental

data over the high and medium frequency range, and the fitted curves were plotted with the experimental data in close-up in Figure 3.10 [115]. Overall the impedance values were low for such a silicon-based composite electrode [158].

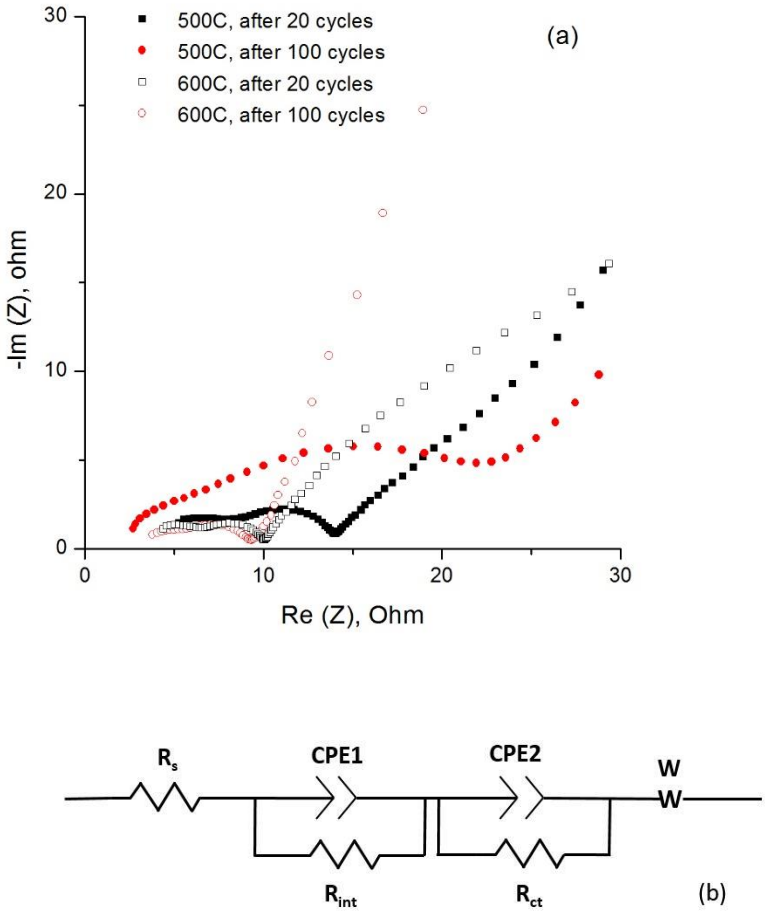

Figure 3.9. (a) Nyquist plots for the Si-Lig composites heat treated at 500 °C and 600 °C after 20 and 100 cycles. (b) Equivalent circuit used for fitting for the experimental data.

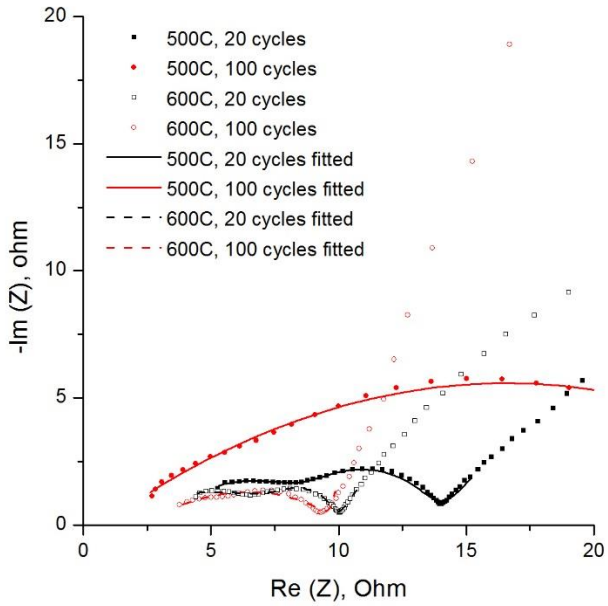

Figure 3.10. Plot of fitted curves using equivalent circuit plotted against the experimental data in close-up.

It is important to note that the addition of 0.5 wt% of PEO helped to stabilize lignin coating on silicon nanoparticles during the heating up process presumably due to (1) promotion of hydrogen bonding between lignin blends, thus increasing the viscosity of Si-lignin composite [106]; (2) Enhanced silicon nanoparticle-lignin hydrogen bonding interactions, allowing for better encapsulation of silicon nanoparticles [117]. PEO is regularly added to lignin blends to ensure better electrospinning or lower the lignin critical concentration required for spinning [107, 116].

It is also worth mentioning that currently the silicon-lignin composites were synthesized with a starting ratio of 1:1 Si to lignin, giving about a final weight ratio of 1.7:1. The increase in Si weight ratio is due to the loss of C, H, and O elements from lignin during heat treatment. This is also accompanied by a volume change in the formed silicon-lignin composite. By experimental observations, a starting ratio of 1:1 guarantees good electronic conductivity while bringing only

moderate volume change. At a starting silicon to lignin ratio of 0.25:0.75, the final weight ratio can be calculated to be ~1:1.8, which is closer in imitating industrial applications of small addition of Si (10 wt%) to graphite (90%). At this weight ratio, substantial volume change for the composite was observed which brought about significant curving of the composite film and underlying Cu substrate. Nonetheless this is harmful to the electrochemical performance of the composite as electrodes should be flat and a curvature may lead to initiation of cracks.

3.4 Conclusions

It is demonstrated that renewable, low-cost, and widely available biopolymer lignin could be composited with silicon nanoparticles under the appropriate low temperature heat treatment to yield composite negative electrodes with exceptional electrochemical performance, retaining 2378 mAh g^{-1} after 100 cycles at 1 A g^{-1}. I explored and presented possible chemical composition changes of lignin during the heat treatment. The effects of heat treatment on lignin as a binder and conductive agent was also elucidated. The performance of this binder-free and conductive additive free electrode is comparable to electrodes where conventional binders or polymer binders were used [31, 118, 133, 158, 159]. Although lignin has been previously explored for use in sodium ion batteries and carbon fibers as active material/support for lithium ion batteries [77, 92, 97], this work demonstrates it effectiveness in silicon-based negative electrodes.

This simple system also presents many opportunities for future studies. Although half-cell performance was remarkable, full-cell performance of the composite electrode shows that there are many challenges to be solved in practical silicon-based electrodes in limiting the loss of lithium. Dupre *et al*. showed that in the case of Si/NMC full cells the NMC and silicon active materials were not degraded or altered, however non lithiated organic species were formed at the extreme surface of the SEI over the course of cycling, pointing out that lithium is likely consumed mainly by parasitic reactions at the negative electrode surface. This was especially true

when a capacity ratio of ~1:1 between negative and positive electrodes was used in this study and the supply of lithium became limited [149]. Although the silicon-lignin composite electrode is quite robust, the porous carbon surface may not be favorable enough in limiting SEI formation and lithium consumption in the full cell configuration. Based on the results and previous literature it is believed that artificial surface SEI coatings of a combination of Al_2O_3/LiF or pre-lithiation to compensate the lithium loss may be two of the approaches to further improve the electrode performance [160, 161].

Chapter 4 High Performance Binder-free SiO_x/C Composite LIB Electrode Made of SiO_x and Lignin

4.1 Introduction

SiO_x-based electrodes are highly promising because of their high specific capacity compared to graphite and improved cycling performance over Si [162, 163]. In amorphous SiO_x, crystalline or amorphous Si cores are uniformly dispersed in SiO_2 matrix which protects Si from contacting the electrolyte during lithiation/delithiation [48, 164]. Lithium oxide (Li_2O) and lithium silicates, primarily Li_4SiO_4, generated from Li reacting with SiO_x during the first lithiation may act as buffer components to accommodate volume change caused by reaction of Li with Si, thus leading to improved cycling performance [164-166]. However, coating SiO_x with carbon [167-169] or compositing with highly conductive material such as carbon nanofibers (CNF) [170] or graphene [171] is highly preferred because of the low conductivity of SiO_x components [172].

Low cost lignin is widely available from paper and pulp mills which is produced in excess of 50 million tons annually [140]. Generally burnt for energy on site, lignin is finding its way into high value-added products such as carbon fibers [79, 80], LIB electrode [93], and sodium ion battery electrode [97]. Previously, it was shown that renewable lignin could be utilized as both the binder and conductive additive for Si nanoparticle composite electrodes with exceptional performance comparable to conventionally designed Si electrodes [26, 126].

Because SiO_x suffers smaller volume changes than Si, it is speculated that heat treated lignin may be a more capable matrix to accommodate SiO_x during extended cycling processes allowing for better capacity retention.

In this section, the structure and electrochemical performance of a binder-free composite electrode of heat treated micro-nano SiO_x-lignin (SiO_x-Lig) electrode is discussed. A binder-free monolithic electrode was formed by mixing cryo-milled SiO_x particles with lignin dispersed in dimethylformamide (DMF), coating on Cu substrate, then heat treated at 600 °C. When tested in the lithium half-cell configuration, the SiO_x-Lig electrode exhibited excellent electrochemical performance, with stable lithium storage capacity of about 900 mAh g^{-1} at current density of 200 mA g^{-1} for 250 cycles.

4.2 Experimental

4.2.1 Materials and experimental procedures

Kraft lignin (Indulin AT) was supplied by Mead Westvaco as a brown powder. It is derived by further acid hydrolysis of Kraft lignin, which removes both the sodium and the hemicelluse. Lignin was first mixed with 0.5 wt% polyethylene oxide (PEO, $1x10^6$ MW, Sigma Aldrich) by spatula, then the powder mixture was dissolved in dimethylformamide (DMF, Sigma Aldrich) with a weight ratio of 30%. The solution was heated to 60 °C under constant magnetic stirring for 2 h. The SiO_x particles of 325 mesh (Sigma Aldrich) were cryo-milled in a 6770 Freezer/Mill (model number 6770, SPEX) for three cycles of 5 min duration each, then added to the solution with a weight ratio of 30% to DMF, and 1:1 weight ratio to lignin. The solution was magnetically stirred for 6 h at 60 °C while going through sonication for 5 min, every 2 h. A Mazerustar KK-250S planetary mixer was used every 2 h to ensure adequate mixing. The solution was stirred and heated until reaching a suitable viscosity for slurry coating onto Cu foil by a doctor blade with a gap spacing of 80 µm. After drying in air, the dried SiO_x-Lig on copper foil was heat treated in a tube furnace with argon atmosphere at a step rate of 2 °C /min up to 600 °C, then held for 2 h. For making electrodes, 12 mm disks of SiO_x-Lig on Cu were cut and stored to be assembled. For making SiO_x-PVDF conventional electrodes for comparison, the

cryo-milled SiO_x particles were mixed with carbon black (Super P C65, TIMCAL) and polyvinylidene (PVDF, No. 1100, Kureha, Japan) in weight ratio of 3:1:1 dissolved in N-methyl-2-pyrrolidone (NMP, 99.5%, Alfa Aesar) using Mazerustar KK-250S planetary mixer, then coated on Cu substrate with a gap spacing of 100 µm. The electrode was dried at 110 °C in vacuum overnight.

4.2.2 Coin cell fabrication and electrochemical measurements

For measuring electrochemical performance of electrodes in half-cells, coin cells (CR2032 type) using the electrodes were assembled in an argon filled glove box, using Li foil as the counter/reference electrode, Celgard 2400 membrane as the separator, and 1M $LiPF_6$ in ethylene carbonate and diethyl carbonate (EC: DEC=1:1 vol%, BASF) with 10 wt% fluoroethylene carbonate (FEC, BASF) additive as the electrolyte. Electrochemical tests were performed using a Bio-Logic potentiostat (VMP-3) at room temperature. The electrochemical properties of the electrodes were measured within a voltage range of 0.005-1.2 V using constant current mode. Impedance was measured potentiostatically by applying an AC voltage of 10 mV amplitude in the range of 100 kHz to 100 mHz using coin cells after a specific number of cycles. The reported specific capacity of the electrodes was based on the weight of the entire electrode material weight. The mass loading of the SiO_x-Lig composite electrodes was 1.1 to 1.2 mg cm^{-2}, and the mass loading of the SiO_x-PVDF electrodes were 1-1.2 mg cm^{-2}. To clarify any ambiguity, in this work the charge process refers to the reactions of Li with SiO_x, and discharge the reverse reactions.

4.2.3 Characterization

Scanning electron microscopy (SEM) images and EDX maps were recorded using a FEI Quanta environmental scanning electron microscope (ESEM). X-ray photoelectron spectroscopy (XPS)

was performed on a Thermo Scientific K-Alpha system with Al Kα radiation. Raman analysis was performed on a Thermo Scientific DXR Raman microscope. X-Ray powder diffraction (XRD) was performed on a Siemens D500. The carbon content of the composite electrode was analyzed by a Leco SC-144DR elemental analyzer. Peak analysis was done using OriginPro 8.

4.3 Results and discussions

Figure 4.1 illustrates the synthesis process of the SiO_x-Lig composite. Prior to heat treatment, SiO_x particles were uniformly dispersed in the lignin polymer. To ensure the uniform and stable coating of lignin on SiO_x particles during the heating process and prevent segregation, 0.5 wt% PEO was added into the mixture. It is well known from previous studies by Kadla *et al* that PEO aids in the formation of fiber morphology during electrospinning of lignin solution [107, 116] due to: 1) promotion of hydrogen bonding between lignin blends, thus increasing the viscosity of the SiO_x-Lig composite and stability of the dispersion [106]; 2) enhanced SiO_x particle-lignin hydrogen bonding interactions allowing for better encapsulation of SiO_x-Lig particles [117]. After the 600 °C low temperature heat treatment lignin is partially pyrolized, leaving behind a conductive carbon shell on individual SiO_x particles while also forming an interconnected conductive matrix to host the SiO_x particles. It should be noted that at this temperature while some H and O are lost as gaseous products such as methanol, formaldehyde, acetic acid, light hydrocarbons, CO_2, and H_2O, some polymeric moieties are still left [103, 104]. It was discussed in the previous study that a Si nanoparticle (Si NP)-lignin composite heat treated at 600 °C showed lower elastic modulus and hardness compared to composite heat treated at 800 °C while displaying superior electrochemical performance, as the result of the better flexibility of the carbon matrix [126]. Also the Si NP-lignin composite showed adequate electrical conductivity for electron transport, therefore in this study the SiO_x-Lig composite was also heat treated at 600 °C instead of higher temperatures.

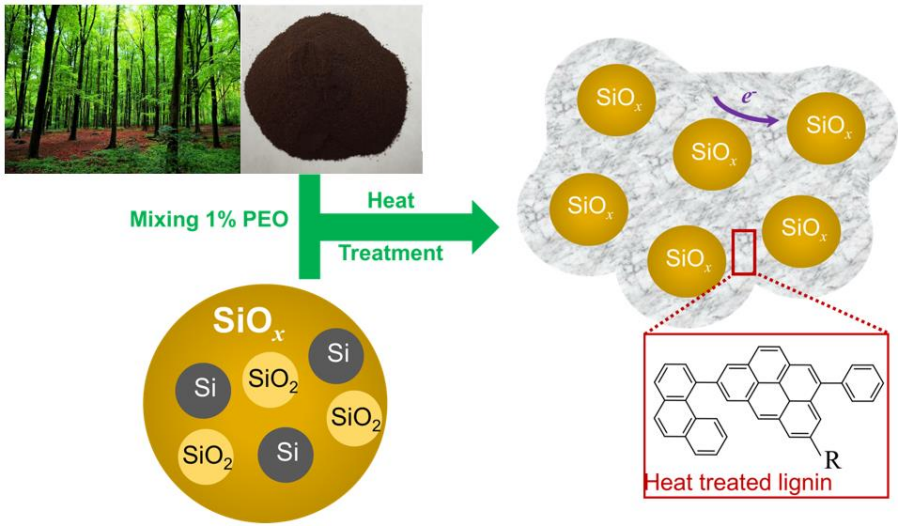

Figure 4.1. Schematic of the formation process of the SiO_x-Lig composite electrode.

Shown in Figure 4.2 are the SEM images of the SiO_x-Lig composite electrode and EDX mapping of O, C, Si elements. It could be seen in Figure 4.2(a) that cryo-milled SiO_x particles are uniformed dispersed in lignin derived matrix with a dense, crack-free surface, and a glassy overall texture [173]. The uniform existence of SiO_x particles in the lignin matrix is confirmed by EDX mapping as shown in Figure 4.2(b).

The crystalline nature of cryo-milled SiO_x particles and as prepared SiO_x-Lig composite were analyzed by XRD and shown Figure 4.3(a). No distinctive peaks of Si or SiO_2 appear for the SiO_x powder, consistent with the generally amorphous nature of the powder. After compositing with lignin and heat treatment, there is an additive broad band superpositioned on the 24.3° broad peak of SiO_x at 21.82 ° attributed to amorphous carbon [62]. Figure 4.3(b) represents the Raman spectra of the SiO_x particles and the as prepared SiO_x-Lig composite. The sharp peak at 502 cm^{-1} and 947 cm^{-1} are attributed to crystalline Si indicating that nano-Si particles were dispersed into Si oxide matrixes, which is in agreement with previous studies [173, 174]. Combining results from XRD pattern and Raman spectra, it could be concluded that some nanocrystalline Si

particles exist in the cryo-milled SiO_x, but they are too small in size to be identified by XRD. For the SiO_x-Lig composite, two broad distinctive bands at 1340 cm^{-1} and 1583 cm^{-1} can be attributed to the D-band (disorder-induced phonon mode) and G-band (graphite band), respectively, of delocalized sp^2 π bands of carbon [175, 176]. The bands related to SiO_x are small in the composite due to the high intensities resulting from carbon atoms.

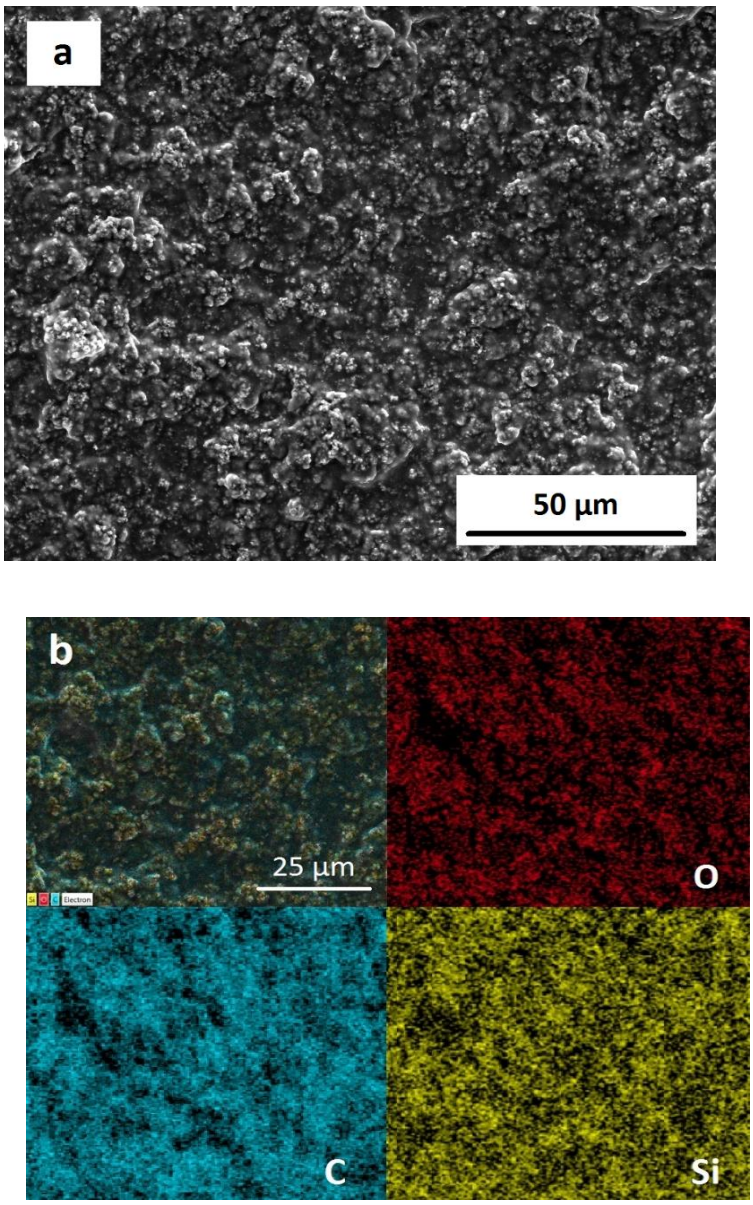

Figure 4.2. SEM image of (a) SiO_x-Lig composite; (b) EDS mapping of O, C, and Si.

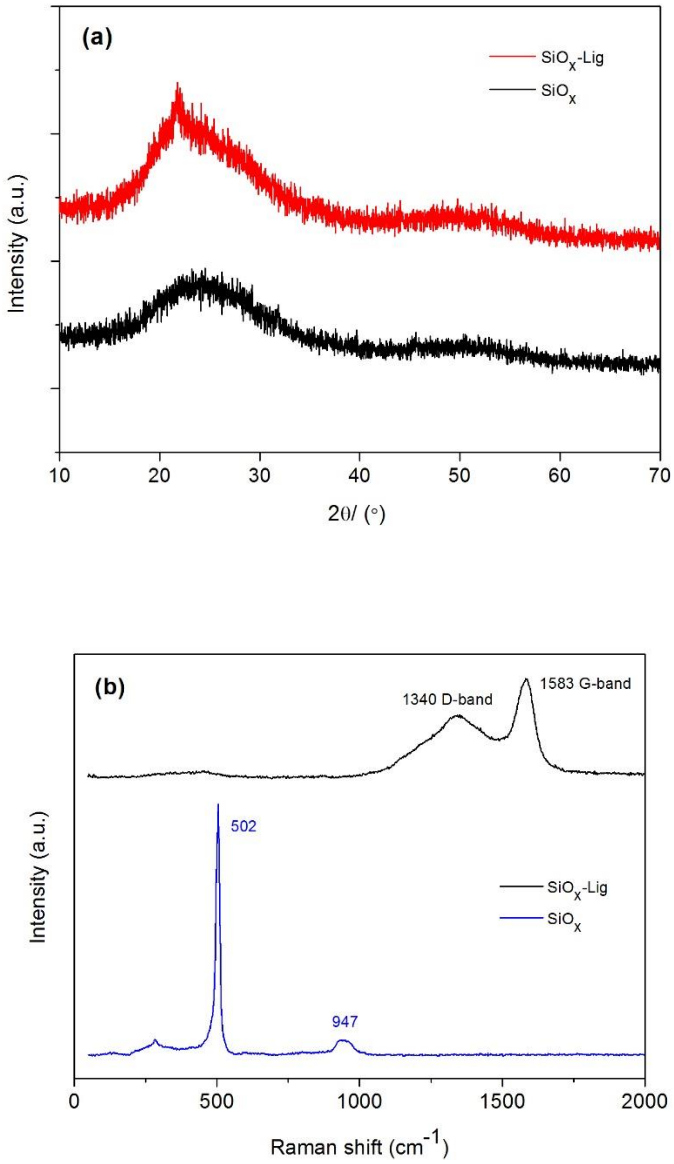

Figure 4.3 (a) XRD pattern and (b) Raman spectra of SiO_x and SiO_x-Lig composite.

To examine the elemental composition and valence states of the composite, XPS was conducted and shown in Figure 4.4. As can be seen in Figure 4.4(a), C, Si, and O are present in the composite. Figure 4.4(b) shows the valence states of Si in the composite. The Si2p spectra was deconvoluted to 4 peaks, 99.8 eV for Si^0, 101.6 eV for Si^{2+}, 102.7 eV for Si^{3+}, and the large

peak at 103.8 eV for Si^{4+}, and is in good agreement with previous reports studying the Si valence states in SiO_x [177, 178].

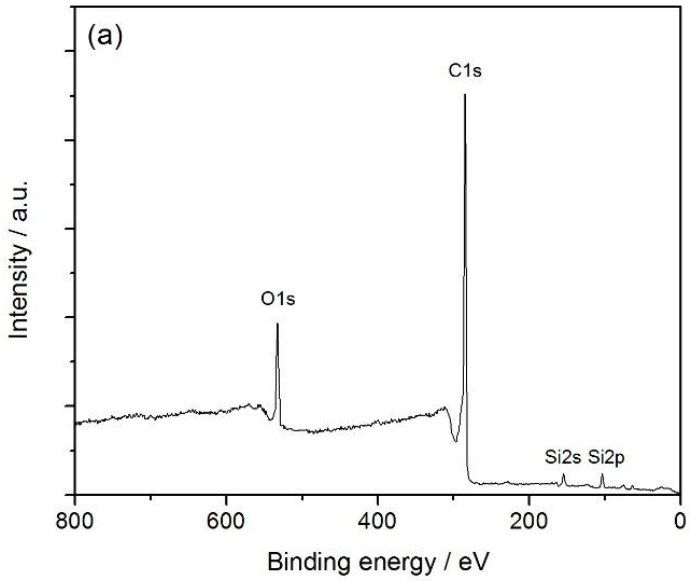

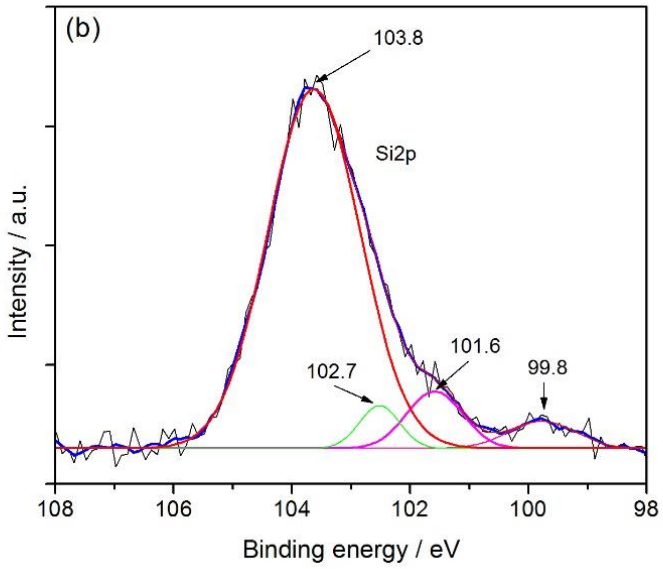

Figure 4.4. XPS spectra of SiO_x-Lig composite (a) full spectra; (b) Si2p spectra.

The electrochemical properties of the SiO_x-Lig composite electrode, including cyclic voltammogram (CV) curves, the potential charge-discharge profile, cycling performance, and rate capabilities were evaluated. Figure 4.5(a) shows the CV of the composite in the initial three cycles at the scan rate of 0.1 mV s^{-1}. In the first cathodic scan, the cathodic peak from 1.75-1 V is associated with the decomposition of the electrolyte additive FEC and the formation of solid electrolyte interface (SEI), while the peak between 0.9-0.5 V is ascribed to the reduction reaction of EC [179]. The small CV area in the 1.75-0.5 V range during the first cathodic scan in this report is similar to other reports utilizing carbon coating, indicating that carbon coating may have procrastinated the reactions in the first cycle [173, 180]. The weak peak from 0.5-0.2 V mainly corresponds to the reduction of SiO_x into Li_2O and electrochemically inactive lithium silicates, primarily Li_4SiO_4 [163, 181], as described in equation [182]:

$$SiO_2 + yLi^+ + ye^- \rightarrow Li_2O + Li\ silicates \qquad (1)$$

Finally, the Si is lithiated and forms the amorphous Li_ySi phase from 0.2 to 0.005V shown in the following equation [183]:

$$Si + yLi^+ + ye^- \rightarrow Li_ySi \quad (2)$$

In the anodic scan, the broad peak centered at 0.56 V is due to the phase transition of amorphous Li_ySi phase to amorphous Si. This phase transition is reversible throughout the cycling process while the formation of Li oxide and Li silicates is mostly irreversible [49]. After the first scan, the CV curve shape stabilizes and increases in area, implying activation of the electrode which agrees with the cycling performance results.

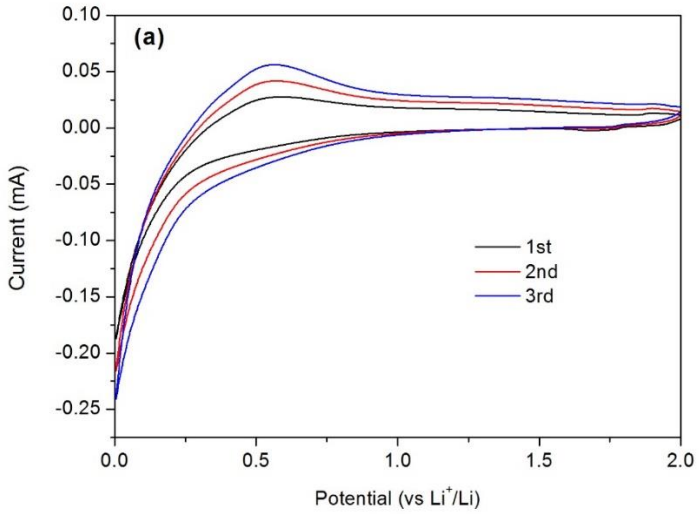

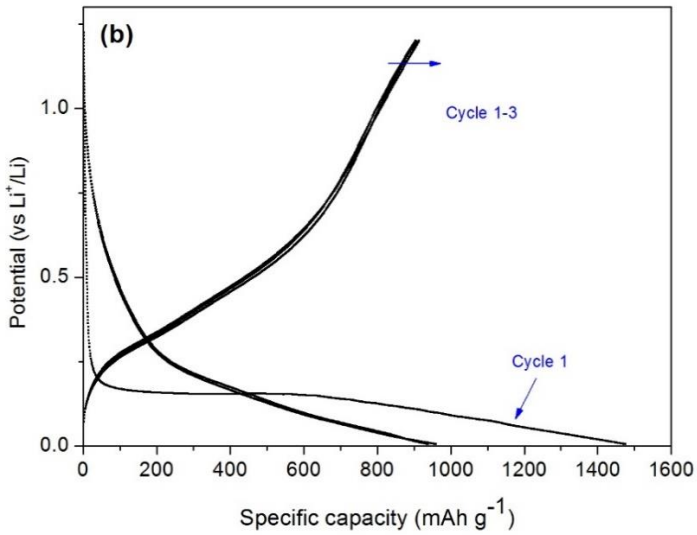
(b)
Cycle 1-3
Cycle 1
Potential (vs Li+/Li)
Specific capacity (mAh g-1)
1.0
0.5
0.0
0
200
400
600
800
1000
1200
1400
1600

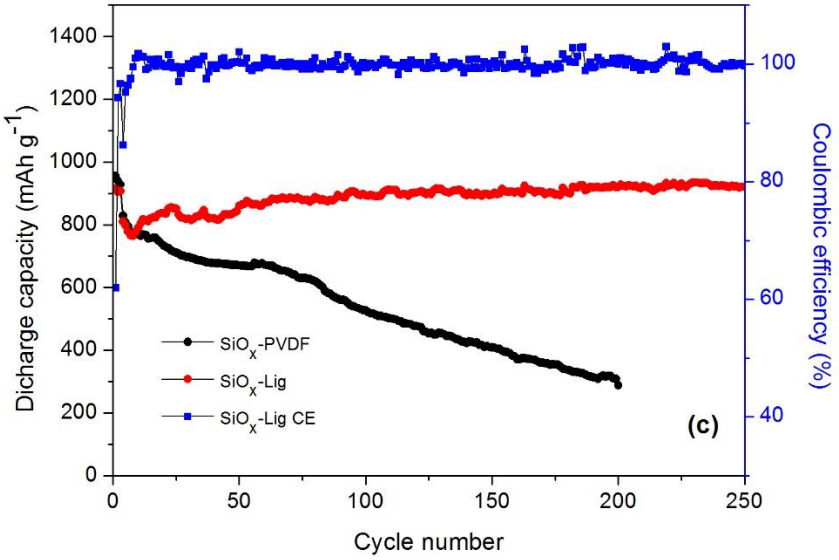
Dicharge capacity (mAh g-1)
Coulombic efficiency (%)
Cycle number
SiOx-PVDF
SiOx-Lig
SiOx-Lig CE
(c)
1400
1200
1000
800
600
400
200
0
100
80
60
40
0
50
100
150
200
250

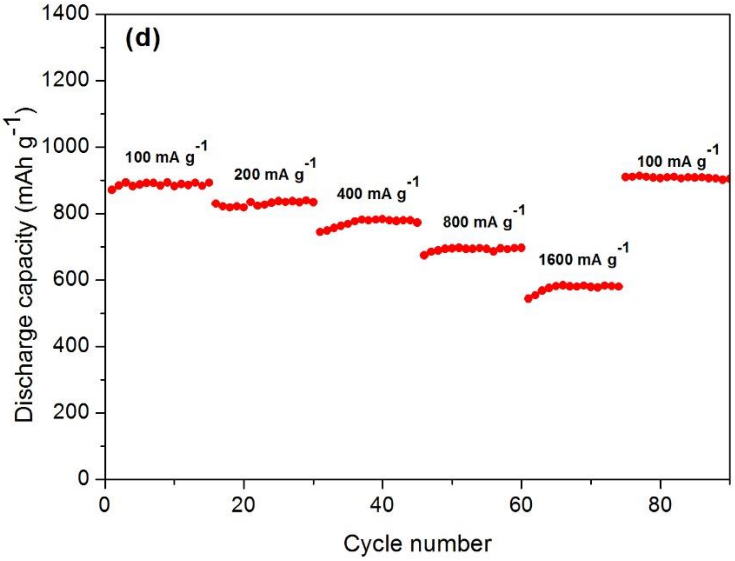

Figure 4.5. (a) Cyclic voltammogram of the SiO_x-Lig composite from the first to the third cycle at a scan rate of 0.1 mV s^{-1}; (b) The charge-discharge curves of SiO_x-Lig composite for the first three cycles at 100 mA g^{-1} in the voltage window of 0.005-1.2 V; (c) The cycling performance of the SiO_x-PVDF and SiO_x-Lig composite at 100 mA g^{-1} for three cycles, then at 200 mA g^{-1} for 3-250 cycles; (d) The rate capabilities of SiO_x-Lig composite at various current densities.

Figure 4.5(b) shows the initial charge/discharge profiles of the SiO_x-Lig composite for the first three cycles at the current density of 100 mA g^{-1}. The first cycle charge capacity of the composite is about 1475 mAh g^{-1} and the first cycle discharge capacity 901 mAh g^{-1}, respectively, with an initial coulombic efficiency of 61%. The low coulombic efficiency is commonly observed in SiO_x-based electrodes and due to the formation of irreversible Li oxides and Li silicates. Although the initial coulombic efficiency is low, the formed inactive phases served as excellent volume expansion buffer and led to excellent cycling capabilities as a trade-off. As measured from elemental analysis, the C wt% in the SiO_x-Lig composite is 35.2%. Since monolithic hard carbon derived from lignin at low temperature typically contributes ~200 mAh g^{-1} [93] and overall capacity of the composite electrode is 901 mAh g^{-1}, the capacity contribution from SiO_x can be estimated to be ~1250 mAh g^{-1} for the first discharge process. The plateau for potential of

1.0 to 0.3 V during the first charge process corresponding to SEI formation is small, with a large plateau from 0.3 to 0.005 V corresponding to Si reaction with Li. The small plateau for 1.0 to 0.3 V during the first charge process may be the result of the thick carbon coating delaying the process. Common charge-discharge profiles attributed to SiO_x material was observed in the 2nd and 3rd cycle [56, 180].

The long-term cycling performance of the SiO_x-Lig electrode is shown in Figure 4.5(c), with SiO_x-PVDF for comparison [52]. After the initial three cycles at 100 mA g^{-1}, there are some discharge capacity fluctuations for the SiO_x-Lig electrode, which resembled local and global fading modes in Si/SiO_x/C electrodes as proposed by Choi *et al* [184]. Basically, both local disconnection of cyclable SiO_x and crumbling of the entire electrode happened during the initial cycles from cycle 3 to cycle 50. As the cycling continued, there is a slight gain in discharge capacity, which stabilized at ~900 mAh g^{-1} until cycle 250. This was observed in several previous reports with carbon coated SiO_x as electrodes and may have been results of utilization of previously unreached Si or a slow activation process [60, 61, 185]. Overall the long-term cycling performance of the SiO_x-Lig composite electrode is extremely stable, and capacity of ~900 mAh g^{-1} was maintained at the end of 250 cycles at a rate of 200 mAh g^{-1}, showing the excellent properties of the lignin derived carbon coating and conductive matrix. Comparatively, the capacity of SiO_x with PVDF as binder faded quickly, reaching 300 mAh g^{-1} after 200 cycles. The rate capability of SiO_x-Lig composite was studied at 100, 200, 400, 800, 1600 mA g^{-1}, and then at 100 mA g^{-1} again and plotted in Figure 5(d). At a high rate of 1600 mA g^{-1}, the capacity is ~584 mAh g^{-1}, 64.9% of the 100 mA g^{-1} values. When the current was switched back to 100 mA g^{-1}, a capacity close to the initial capacities was observed, showing the excellent reversibility of the electrode. The excellent reversibility and rate capability can be attributed to the flexible carbon matrix formed by lignin at a low temperature of 600 °C [126].

To investigate the electronic conductivity the SiO_x-Lig electrode after 5 cycles and after 250 cycles was studied by electrochemical impedance spectroscopy (EIS), with results shown in Figure 4.6. The EIS plots usually consist of a semicircle at high frequency which represents the resistance of the electrolyte and charge-transfer, and a Warburg tail at lower frequencies due to diffusion-resistance from the electrode material. The high frequency semicircle intercept for the electrode after 5 cycles is about 10.3 Ω. After 250 cycles, there is a small increase in the intercept to ~15 Ω. Considering the number of cycles, the electrode shows good ability to maintain electronic conductivity and electrode integrity. Overall the resistances are small compared to similar works with carbon coated SiO_x [62, 186].

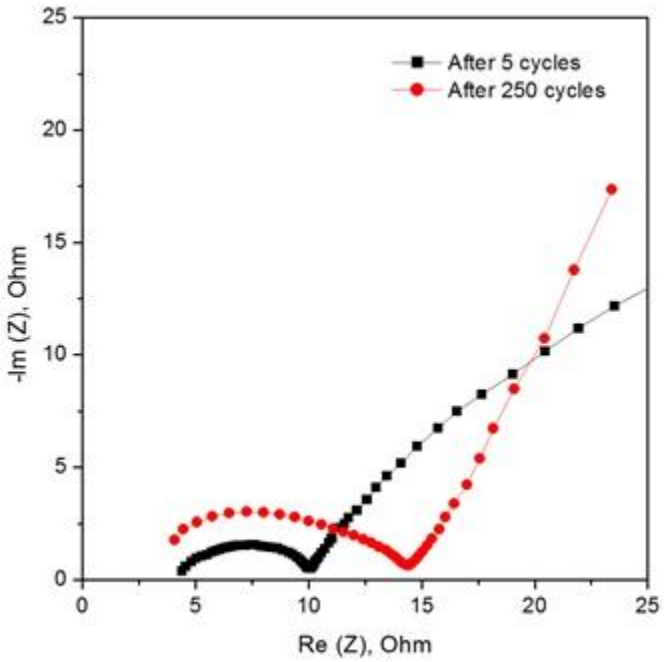

Figure 4.6. Electrochemical impedance spectroscopy (EIS) of SiO_x-Lig composite electrode after 5 cycles, and after 250 cycles.

Top post-cycling (250 cycles) SEM images of the composite electrode was shown in Figure 4.7. The images shows that, after extensive cycling, a dense layer of SEI was formed on the surface of electrode, was somewhat pressed flat due to coin cell configuration, and changed the surface morphology as compared with Figure 4.2(a). No large scale cracks were found in the SEM with lower magnification, and only faint cracks was seen in the SEM image with larger magnification, pointing to the robustness of the composite electrode formed with SiO_x and lignin.

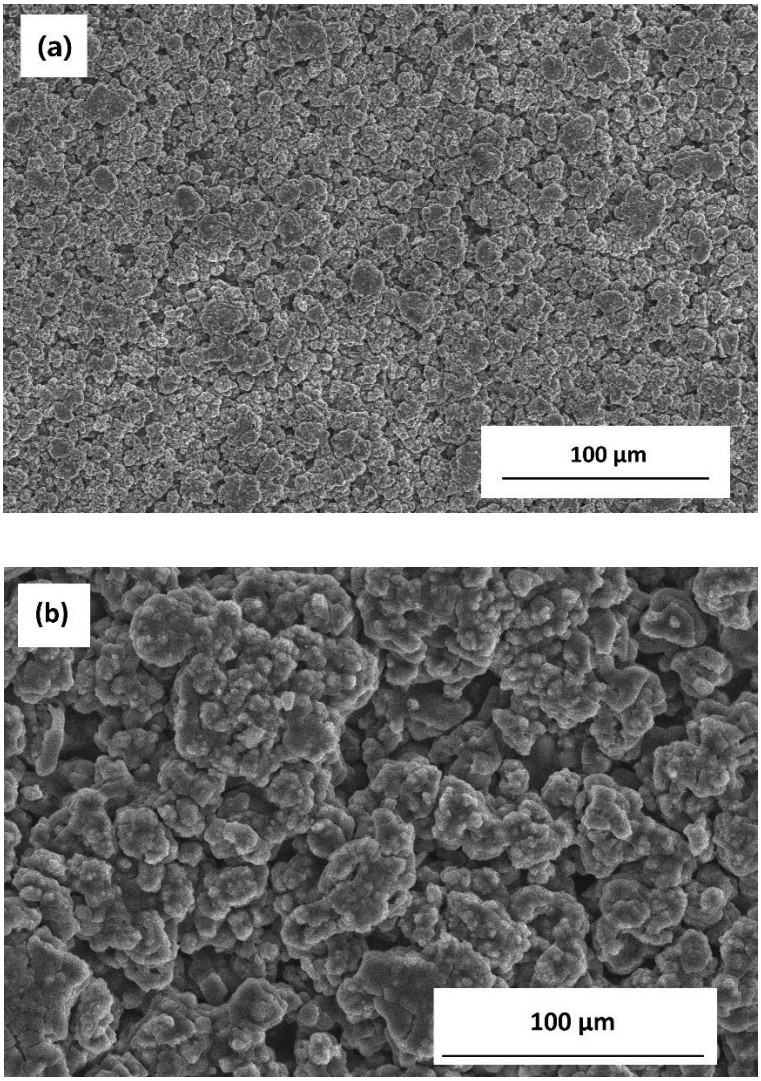

Figure 4.7. Post-cycling SEM image of SiO_x-Lig composite electrode after 250 cycles (a) lower magnification (b) higher magnification.

4.4 Conclusions

A simple method to utilize bio-renewable lignin to prepare a SiO_x-Lig composite electrode with exceptional electrochemical performance and structural robustness was demonstrated. The discharge capacity of the composite electrode can be maintained at ~900 mAh g^{-1} for over 250 cycles at a rate of 200 mA g^{-1}. While in my previous studies lignin was shown to form an excellent composite electrode with Si NP with high capacity, the capacity retention after 100 cycles was a moderate 82% [126]. When composited with SiO_x however, lignin showed even greater potential in accommodating volume changes during lithiation and delithiation. This may be because SiO_x electrode experiences smaller volumes changes (160%) [164] compared to crystalline Si (300%) [187]. Thus, the lignin-derived carbon matrix was more proficient in handling the volume changes in SiO_x-Lignin electrodes. To the best of my knowledge this is the first work incorporating lignin into SiO_x-based electrodes with promising results. It is believed that the performance of the composite electrode could be further improved by optimizing the ratio of SiO_x: lignin or adding prelithiation agents into the composite to improve initial coulombic efficiency [52, 188]. Specifically, SiO_x may be prelithiated with Li in a heated environment, then directly mixed with glassy state lignin at >200 °C to produce high initial coulombic efficiency composite anode material.

Chapter 5 Recent Advancement of SiO_x Based Anodes for Lithium-Ion Batteries

Most of the contents of this chapter is to be published as a review paper "Recent Advancement of SiOx Based Anodes for Lithium-Ion Batteries".

5.1 Introduction

5.1.1 An overview of lithium ion battery anodes

The state-of-the-art LIBs use graphite as the anode (negative electrode) and Li metal oxides ($LiCoO_2$, $LiMn_2O_4$, $LiFePO_4$, $LiCo_{1/3}Mn_{1/3}Ni_{1/3}O_2$, etc.) as the cathode (positive electrode), whose theoretical capacities are 372 mAh g^{-1} and less than 200 mAh g^{-1}, respectively. While on the cathode side gradual advancements were made [189], on the anode side new materials such as Si boasts a theoretical capacity of 4200 mAh g^{-1} which may contribute significantly to the increase of overall capacity. Despite the high theoretical capacity, Si anodes are faced with challenges such as high volume variation during lithiation and delithiation (~300%) and unstable SEI which leads to low cycling efficiency and capacity retention [25, 131]. Although extensive nanostructures [158, 190, 191], coatings [109, 137, 192-194], binders [31, 39, 133], and additives [30, 195, 196] have been studied and improvements were seen to a degree, volume variation, unstable SEI, and consumption of Li is still inevitable in full-cells thus hindering the practical usage of Si [147, 149, 197].

When the total specific capacity of a battery is evaluated as a function of anode and cathode specific capacity, it maybe suggested that for the projected cathode capacity of 200 mAh g^{-1}, anode capacities higher than 2000 mAh g^{-1} reaches saturation and have little effect on the overall capacity [38]. In this context SiO_x-based anode is particularly promising because of its trade off of lower theoretical initial discharge capacity of ~2007 mAh g^{-1} for longer cycle life

compared to Si [198]. During reaction and cycling of Li with SiO_x, formation of irreversible Li_2O and Li_4SiO_4 decreased the specific capacity, but acted as a volume variation buffer matrix to cyclable Li_xSi which in turn saw improved cycling and capacity retention [163, 181, 182].

This article summarizes the most recent advances of SiO_x based nanomaterials with details on reaction mechanism, fabrication of SiO_x electrodes, and methods to improve SiO_x electrode performance. Finally, a general outlook is given for using SiO_x based electrodes in LIBs.

5.1.2 Characteristics of SiO_x-based anode

5.1.2.1 Structure of amorphous SiO_x

Amorphous Si suboxides were known for decades and used in a variety of technical applications prior to its utilization as anode material for LIBs. The structure of the monoxide phase was controversially in early literature, where two main models were preferred. In the random-bonding (RB) model by Philipp [199, 200], Si-Si and Si-O bonds are described as statistically and randomly distributed throughout a continuous random network of single-phase Si monoxide, hence implying a single-phase Si monoxide. In the random-mixture model (RM) it is assumed that SiO_x contained mixtures of small-domains of Si and SiO_2, corresponding to a multi-phase mixture [201, 202]. More recently through the help of TEM electron scattering, electron energy-loss spectroscopy (EELS), and electron spectroscopic imaging (ESI) amorphous Si and amorphous SiO_2 phases are clearly identified in Si monoxide, pointing out the RM model is appropriate to describe its structure [203]. Hohl *et al*. [178] proposed an interface clusters mixture model (ICM) based on previous models and combination of experiments (HRTEM, ELNES, XPS, NMR, ESR, etc.) which suggested amorphous SiO_x as a frozen non-equilibrium system of disproportionation in the initial state. Specifically, Si existed in a number of chemical states, Si^0,

Si^{+}, Si^{2+}, Si^{3+}, Si^{4+}, and a number of possible atomic chains are possible as shown in Figure 5.1(a). Nevertheless, techniques such as XRD, XPS, X-Ray Raman scattering and so on only provided the average or spectroscopic information on the structure of amorphous SiO mainly due to the limitation in spatial resolution of these conventional methods. Most recently by deploying angstrom-beam electron diffraction (ABED) as the main tool and supplemented by synchrotron high-energy XRD (HEXRD) and computational simulations, Hirata *et al*. [48] was able to directly experimentally observe the structure of SiO_x on the atomic resolution. The reconstructed heterostructure model of amorphous SiO_x is shown in Figure 5.1(b). This reinforced the established theory that in amorphous SiO_x, Si and O exists in clusters of Si and SiO_2 while surrounded by a variety of suboxide-type tetrahedral coordinates at interface regions.

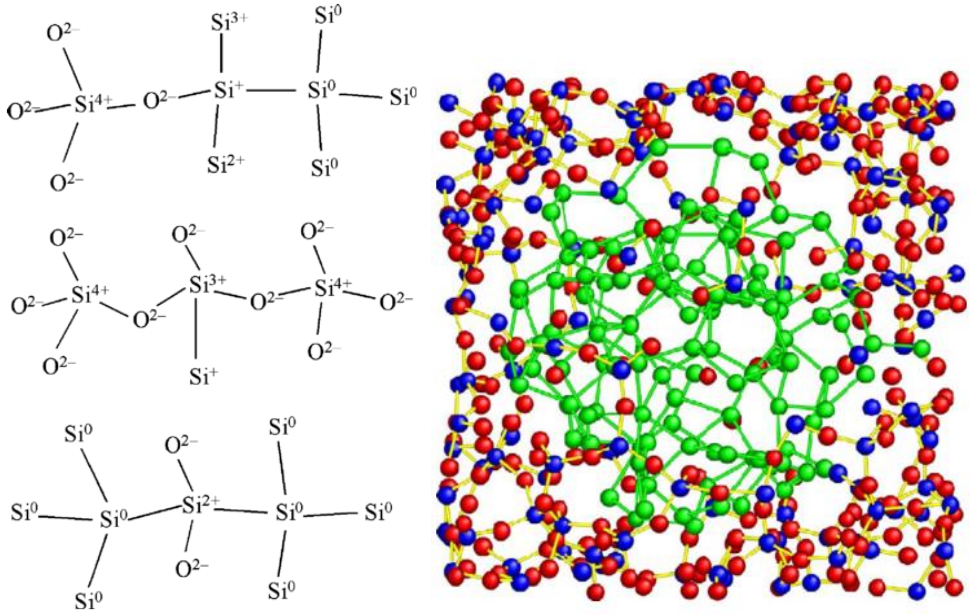

Figure 5.1. (a) A selection illustrating the variety of the possible atomic chains and Si chemical states in SiO_x. Reproduced from [178], with permission from Elsevier. (b) Reconstructed heterostructure model of amorphous SiO_x. The inner part corresponds to an amorphous Si cluster and the outer part is amorphous SiO_2 matrix. The blue, red, and green circles denote Si and O in amorphous SiO_2 and Si in the Si cluster, respectively. Reproduced with permission [48]. Copyright 2016, Nature Publishing Group.

5.1.2.2 Electrochemical properties of amorphous SiO_x

Yang *et al*. was one of the first to systematically study electrochemical properties of amorphous SiO_x [162], with oxides of varying oxygen content. They showed that SiO_x consisted of crystalline Si, amorphous SiO, and SiO_2 through XPS, and that all SiO_x oxides showed reactivity with Li. Additionally, it was observed that a decrease in oxygen content in SiO_x enhanced the reversible capacity and the first cycle efficiency, but reduced the capacity retention upon cycling. Subsequently the electrochemical behaviors and mechanisms of SiO_x anode for LIBs have been reported by several researchers [49, 50, 163, 181, 182, 204, 205]. From these studies varying initial charge capacities, discharge capacities, and coulombic efficiencies have been reported, likely due to the varying composition of SiO_x and experimental conditions. The reaction mechanism of SiO_x can be summarized in equation 1 as follows according to Yamamura *et al.* [206]:

$$4SiO + 17.2Li \rightarrow 3Li_{4.4}Si + Li_4SiO_4 \qquad (1)$$

This gives SiO electrode theoretically an initial charge, discharge capacity, and initial coulombic efficiency (ICE) of 2615 mAh g^{-1}, 2007 mAh g^{-1}, and 76.7%, respectively. From thermodynamics point of view the electrochemical reaction process of the SiO_x component in SiO_x with Li can be divided into the following stages [205]: (1) At the initial stages of the reaction, Li silicates (Li_2SiO_5, Li_2SiO_3, and mainly Li_4SiO_4) are formed together with metallic Si, which corresponds generally to the 0.35-0.5 V potential plateau area of amorphous SiO curve shown in Figure 5.2(a). Li_4SiO_4 is electrochemically inactive as reported in ref. [206], and no Li dissolution occurs even at the very high positive potential of 4.0 V vs Li/Li^+. Thus, the formation of Li_4SiO_4 results in generation of irreversible capacity, and the silicate acts as a buffer component which accommodates volume changes of SiO_x due to further alloying of Si with Li [166, 207]. The observed capacity of ~600 mAh g^{-1} in this potential range corresponds well with

the theoretical capacity of Li silicates. (2) Secondly, the formed metallic Si react with Li to form Li-Si alloys ($Li_{12}Si_7$, Li_7Si_3, and $Li_{13}Si_4$) that are in equilibrium with Li_4SiO_4, this is seen in the potential range of 0.05-0.35 V (including the capacity contribution from KB and PI additives from their experiment) in the amorphous SiO_x curve shown in Figure 5.2(a). The capacity contribution from metallic Si alone cannot account for the observed 2610 mAh g^{-1} if excluding the ~600 mAh g^{-1} irreversible capacity of Li silicates, thus indicating the partial decomposition of Li silicates to Li_2O. (3) Thirdly, Li_4SiO_4 is decomposed to form Li_2O and $Li_{13}Si_4$. (4) Further Li insertion produces $Li_{22}Si_5$ from $Li_{13}Si_4$. (5) Finally metallic Li is deposited.

In reality SiO_x commercially available is a complex mixture of amorphous Si, interphase boundary layer (corresponding to Si:O=1:1, or SiO), and amorphous Si oxide (SiO_2). Studies have proved that SiO_2, although known to be inactive with Li^+ and strongly insulating, can in fact react with Li shown in equation 2 [182] and equation 3 [204]:

$$SiO_2 + yLi^+ + ye^- \rightarrow Li_2O + Li\ silicates \qquad (2)$$

$$2Li_2O + Si \rightarrow SiO_2 + 4Li^+ + 4e \qquad (3)$$

A simplified depiction of reaction of amorphous SiO_x with Li comprised of amorphous Si, SiO, and amorphous SiO_2 in the ratio of 4:2:4 was proposed by Kim *et al*. [50] and shown in Figure 5.2(b), where $Li_{15}Si_4$, Li_4SiO_4, and Li_2O are shown as the main products. A visual depiction of SiO_x anode during repeated lithiation and delithiation cycles could be presented as shown in Figure 5.2(c) [164], where reversible Li_xSi cores (yellow) are embedded in a matrix (orange) consisting of irreversible Li silicates and Li_2O. The formation of Li_2O phase from SiO_x is important in a number of aspects. First, Jung *et al.* [164] suggested through first principles molecular dynamics simulation that Li_2O phase served as a fast Li diffusion channel of the matrix surrounding Li_xSi cores, because the Li ions in Li_2O diffuse faster by at least 2 orders of magnitude than those in Li silicates. A Li_2O-rich matrix in lithiated SiO_x may maximize the

performance of SiO_x in terms of both capacity and rate capability. Secondly, Li_2O and Li_4SiO_4 matrix surrounding Li_xSi cores acted as volume expansion buffer zones during lithiation and delithiation. For the $Li_{15}Si_4$ phase, the volume expansion is approximately 280% [208], much larger than the 200% of Li_4SiO_4 or Li_2O [163]. Coupled with the higher densities of Li_4SiO_4 (2.39 g cm^{-3})or Li_2O (2.02 g cm^{-3}) compared to $Li_{15}Si_4$ (1.18 g cm^{-3}), this explains why Li_4SiO_4 and Li_2O acted efficiently as volume expansion buffers in the cycling of SiO_x and resulting improved cycling performance [204].

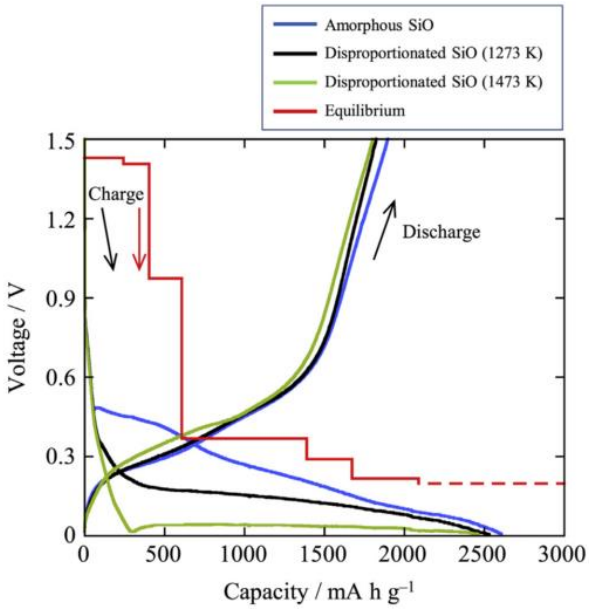

a

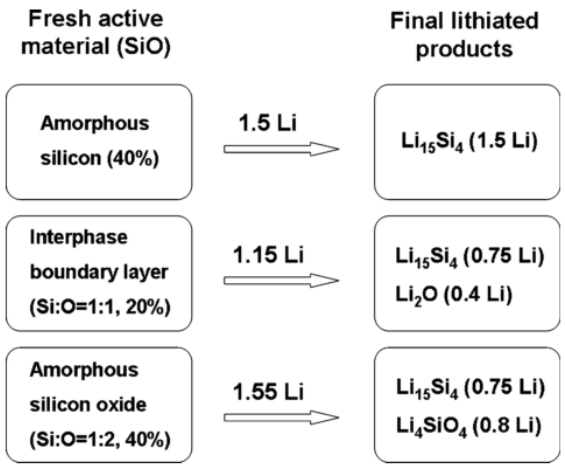

b

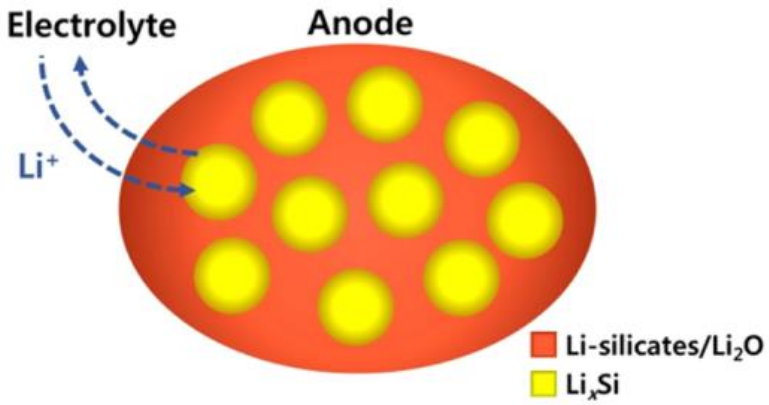

c

Figure 5.2 (a) Typical charge and discharge curves for amorphous SiO_x electrode. The 1st cycle of SiO/EC:DEC(1:1) + 1 mol L^{-1} $LiPF_6$/Li cell in the voltage range of 0-1.5 V at 25 ℃ is shown in blue. Charge conditions: a constant current of 15 mA g^{-1} until a voltage of 0 V. Discharge conditions: a constant current of 15 mA g^{-1} until a voltage of 1.5 V. Reproduced with permission [205]. Copyright 2016, Elsevier. (b) The overall schematic model for the reaction of SiO_x electrode with Li. Reproduced with permission[50]. Copyright 2011, Elsevier. (c) Schematic illustration of SiO anode during repeated lithiation and delithiation cycles. Reproduced with permission [164]. Copyright 2016, American Chemical Society.

5.1.2.3 Effect of disproportionation on SiO_x electrochemical properties

Among Si suboxides, amorphous SiO_x is the most common commercially available variety, and is usually manufactured with a vapor deposition technique from the gaseous SiO produced by the reaction of Si and SiO_2 at high temperatures [205, 209, 210]. A notable characteristic of amorphous SiO_x is its disproportionation into solid nanocrystalline Si particles and solid SiO_2 above ~850 ^oC [211, 212], although it is also shown to be unstable even at 400-900 ^oC by an earlier report [213]. Mamiya *et al.* [211] found that nanocrystalline Si with average particle sizes of 4-5 nm started forming at ~850 ^oC, and the amount of, rather than size, of the precipitated particles gradually increased with annealing time. Si^0 and Si^{4+} valence states found in the disproportionated SiO_x increased and Si^{1+}, Si^{2+}, and Si^{3+} states decreased, giving rise to different electrochemical properties than amorphous SiO_x. The voltage profile for the first cycle lithiation of disproportionated SiO_x is much closer to that of Si anodes due to the amount of nanocrystalline Si formed in the reaction, as shown in Figure 2a. The electrochemical behavior and mechanisms of disproportionated SiO_x have been reported further by a number of researchers [177, 184, 205, 214-217]. Park *et al.* [177] attributed the superior cyclability and reversibility of d-SiO_x (1000 °C)(disproportionated SiO_x at 1000 °C) compared to pristine SiO_x and d-SiO_x (800 °C) to the formation of well-distributed Si nanocrystallites of *ca.* 5nm and amorphous SiO_x matrix. However further increase of heat treatment temperature to 1200 °C saw a decrease in performance presumably due to formation of excess Si^{4+}-based amorphous suboxide which were inactive to Li reaction. Similarly, Hwa *et al.* [216] observed that disproportionated SiO_x heat treated at 1200 °C showed almost no capacity because Si nano-crystallites and amorphous SiO_2 were surround by inactive Si-suboxide and could not react with Li. By deploying a mechanical ball-milling process, the size of disproportionated SiO_x particles decreased and Si nano-crystallites and amorphous SiO_2 was exposed, leading to excellent electrochemical storage and cycling properties.

Tashiro *et al*. [217] synthesized amorphous core SiO_x nanocomposites with improved capacity and cycling performance by rapid quenching plasma spray physical vapor deposition (PS-PVD). Under rapid quenching conditions SiO_x particles were cooled rapidly to attain smaller size and the subsequent disproportionation reaction which directly happened after condensation of the SiO_x nanocomposites from SiO vapor, altered the particle structure from crystalline to amorphous. Diffusivity of such SiO_x nanocomposites was estimated to be two orders of magnitude higher than that for the bulk SiO_x, which facilitated instantaneous nanoparticle and composite structure formation. Additionally, the addition of CH_4 to SiO_x vapor during deposition decreased oxygen content in the synthesized SiO_x may also have contributed to the enhanced electrochemical properties [218].

The effect of oxygen content on the electrochemical behavior of SiO_x anodes was systematically studied mainly using film model electrodes due to the easiness of oxygen content control [165, 218-220]. By deploying ATR FTIR spectroscopy and XPS analysis, Nguyen *et al*. [218] suggested that an increase in oxygen content of SiO_x ($0.4 \leq x \leq 1.3$) led to the decrease of reduction of electrolyte but oxides are subject to degradation by acid-etching, resulting in poor cycling ability. The use of silanes as electrolyte additive then was shown to be effective in forming a protective layered network at the electrode surface, providing preservation of the electrode structure and particle connectivity. Kim *et al*. [220] found that increase in x resulted in decrease of the initial columbic efficiency (ICE) largely due to the oxidation of Li-ions such as Li_2O and Li_4SiO_4. Cyclability, however, is improved with the increase of the x-values, indicating that stress and volume change during lithiation/delithiation are accommodated by the oxide buffer around the Si.

These studies suggest that disproportionation maybe an effective method to alter the chemistry in SiO_x and improve cycling by forming an enhanced buffer matrix, however additional

treatments were required to "activate" the heat-treated SiO_x, either by ball-milling, addition of additives, or other synthesis alternatives.

5.1.3 The advantages and challenges of SiO_x-based LIB anode

Table 5.1 compares the properties of graphite, Si, and SiO_x anodes for LIBs [38]. Graphite has a low theoretical capacity of 372 mAh g^{-1} while Si had the largest theoretical capacity of the three. The large difference in lithiation capacity is also reflected in the volume change of the anode materials as Si suffers from massive 280% volume expansion upon lithiation, leading to electrode pulverization and loss of electric contact between active materials and active material-current collector interface [172]. Furthermore, the large volume expansion often leads to growth of new solid electrolyte interface (SEI) on each cycle, which is a Li conducting but electronic insulating passivation layer. While the SEI layer is critical for stable cycling of Si-based anodes due to its passivating properties, cyclable Li and electrolyte is also consumed during its formation leading to capacity fading [221]. This effect is more pronounced in full-cell setups where the amount of Li is provided by the cathode oxide material and fixed, wherein the half-cell the Li is provided by a Li foil and much more abundant [149]. Although in some studies good capacity retention was achieved in Si-based anode full cells [222-224], complicated or expensive synthesis techniques makes them questionable in large scale industrial applications. In most other cases, large discrepancies between electrochemical performance of Si-based anodes in half-cell and full-cell setups were observed, showing that a lot work still needs to be done in the field [147-149, 197, 225].

In comparison SiO_x-based anode has a lower initial theoretical capacity of 2615 mAh g^{-1}, is usually denser, and has a much smaller volume change of ~160% during lithiation/delithiation [164]. Smaller volume changes in SiO_x-based anodes means capacity loss due to disconnection between particles, conductive additives, and binder/current collector are less likely to occur. In

addition, smaller volume changes and the formation of Li_2O and Li silicates from the first cycle also prevented direct contact of core Si nanocrystallites with electrolyte, thus resulting in less SEI growth in subsequent cycles [226]. Therefore, the inherent long-term cycling performance of SiO_x is considered superior to that of Si-based anodes. Due to its excellent performance, small amounts of SiO_x have already been added to graphite as the anode material commercially buy a few manufacturers.

The main drawback for SiO_x-based anodes is the low initial coulombic efficiency (ICE) resulted from the formation of Li_2O and Li silicates in the first cycle. This figure varies in reports due to different experimental conditions, typically falls in the range of 65.1-82.1%, and is lower than that of Si-based anodes [188]. Recently through pre-lithiation, the ICE of SiO_x-based anodes was dramatically increased along with enhancement in cycling performance [52, 56, 188, 227-234]. Further studies into optimization of pre-lithiation conditions may see the low ICE drawback tackled and realization of practical SiO_x-based anodes with exceptional performance.

Table 5.1 Comparison of anode materials

Anode material	C	Si	SiO_x
Density (g cm^{-3})	2.25	2.33	2.13
Volume change (%)	12	280[a]	160[b]
Lithiated phase	LiC_6	$Li_{15}Si_4$	Li_xSi, Li_2O, Li_4SiO_4
Initial theoretical charge capacity (mAh g^{-1})	372	3579	2615
Typical initial coulombic efficiency (%)	90-95	77.5-84[c]	65.1-82.1, 93.8-94.9[d]

[a] The theoretical capacity of Si is based on $Li_{15}Si_4$. [b] From ref [164]. [c] Based on a number of recently published Si-based anode works (not taking into account Si-Graphite composites) [27,

114, 133, 150, 158]. [d] Based on a selection of recently published SiO_x-based anode works [52, 56, 180, 205, 228, 235-239].

Since unlithiated intrinsic Si is a rather poor electrical conductor ($\approx 10^{-3}$ cm^{-1}, which increases to $\approx 10^{-3}$ cm^{-1} after lithiation) [240], SiO_x-based anodes also suffer from poor electronic conductivity leading to limited performance under high rates and potentially reduced cycling performance [172]. Nanostructuring to reduce particle diffusion [241], application of carbon coatings [242], and doping [243] maybe some of the techniques to alleviate this problem and is further discussed in detail.

5.2 Fabrication of SiO_x based nanostructured electrodes and their electrochemical performance as LIB anodes

As described briefly above, although SiO_x displays promising results as LIB anode due to its composition, problems in capacity retention, Si utilization, and low ICE still needs to be addressed. In this section, we highlight some of the strategies which addresses these setbacks and improves the performance of SiO_x electrodes, such as (1) SiO_x/C composites, (2) Si/SiO_x core-shell composites, (3) SiO_x/CNF, SiO_x/CNT, and SiO_x/Graphene, (4) Si/SiO_x nanotubes, wires, and rods, (5) porous SiO_x electrodes, (6) Si/others electrodes.

5.2.1 SiO_x/C composite electrodes

One of the most appealing approaches to for both Si-based and SiO_x-based anodes is to form core-shell composites by coating the nanoparticles with a conductive layer of carbon or carbon matrix. Carbon coatings/matrixes are especially attractive because carbon is (1) highly conductive allowing for fast transport and rate kinetics [244]; (2) relative ductility compared to inorganic

coatings allowing for accommodation of stress and strain [28]; (3) easy to obtain with a variety of techniques and precursors with potential for scale-up synthesis; (4) enables the formation of a stable SEI layer. For these reasons, many reports utilized SiO_x/C composites for high performance electrodes [58, 62, 166-169, 184, 207, 237, 242, 245-256].

An early report in 2007 by Kim *et al.* [255] synthesized SiO_x/C composite powders by mixing pure milled SiO_x powders with polyvinyl alcohol and subsequent heat treatment at 900 °C under argon atmosphere. The electrode delivered an initial charge and discharge capacity of 1050 and 800 mAh g^{-1}, respectively with an ICE of 76%, and the capacity remains at 710 mAh g^{-1} after 100 cycles. The disproportionation of pure SiO_x into Si and SiO_2 in the presence of polyvinyl alcohol at 900 °C was confirmed by X-ray power diffraction (XRD) and transmission electron microscopy (TEM), which saw the growth of Si crystallite size from 1-2 nm to 3.6 nm, as estimated by Debye-Scherrer formula. A few reasons contributed to the enhanced performance of the composite SiO_x/C electrode. First, reduced particle size of SiO_x by ball-milling helped to increase the mechanical stability. Secondly, the carbon from resulting from polyvinyl alcohol provided better electrical contact during cycling. Thirdly, the electrode material remained in an amorphous state during the lithiation/delithiation reaction, and this helped to maintain the integrity of the electrodes. Liu *et al.* [252] similarly synthesized SiO_x/C composite anode with milled SiO_x and coating by chemical vapor deposition (CVD) instead of pyrolysis method, which delivered first-cycle charge and discharge capacities of 1225 and 546 mAh g^{-1} (44.5% ICE), respectively. The specific capacity at 0.15 A g^{-1} can be maintained above 620 mAh g^{-1} after 50 cycles with a capacity retention rate of 88%. It was found that C-coating of sub-μm SiO_x particles in a fluidized-bed CVD process produced nano-porous SiO_x/C composite secondary particles that contained randomly distributed pores thus allowing accommodation of volume expansion.

While many of the reports synthesized SiO_x/C composite electrodes using commercialized SiO_x powder and graphite or organic carbon precursor, wet chemistry routes were also reported by several groups using siloxane (e.g., tetraethoxysilane, TEOS) as the Si source [167, 237, 256, 257]. Wang *et al*. [169] prepared precursor solution of SiO_2 nanoparticles by a modified Stöber method using TEOS, absolute ethanol, and ammonia as the starting materials. To form Core-shell SiO_x/C nanocomposites, epoxy resin as carbon source was then added into the SiO_2 microemulsion followed by pyrolysis. The SiO_x/C composite electrode, comprised of Si clusters and well-ordered SiO_2 domains delivered highly reversible specific capacity of (~800 mAh g^{-1}), excellent cycling stability and good rate-capability. To further simply the synthesis process of SiO_x/C composite electrode and improve yield of SiO_x/C particles, Lv *et al*. [245] devised a one-pot synthesis method to prepare SiO_x/C composite as shown in Figure 5.3(a). High concentration colloidal silica solution was mixed with sucrose as carbon source to form a slurry, which was ball-milled to avoid agglomeration in high concentration environment and then pyrolized to form the final product. The derived SiO_x/C composite showed initial cycle charge and discharge capacities of 1475 and 1015 mAh g^{-1} (68.8% ICE), respectively, and the capacity remained above 820 mAh g^{-1} after 100 cycles. Li *et al*. [167] reported synthesis of sugar apple-shaped SiO_x/C nanocomposite spheres by replacing the silicate sol-gel process with organic resorcinol/formaldehyde sol-gel process as shown in Figure 3b. First, resorcinol/formaldehyde coupled with positively charged cetyltrimethyl ammonium bromide (CTAB) micelles to form CTAB-coated micelles via electrostatic interaction, acting as a soft template. Polysiloxane and resorcinol/formaldehyde further condensed at the soft template surface via electrostatic interaction, leading to the formation of an outer layer sphere coating on the resorcinol/formaldehyde core. After annealing, the resorcinol/formaldehyde polymer was transformed into carbon while polysiloxane was transformed into SiO_x, giving a nanostructure that truly resembled sugar apples. Due to its unique interconnected structure with interparticle

voids, the composite maintained discharge capacity of up to 550 mAh g^{-1} at 100 mA g^{-1} after 400 cycles.

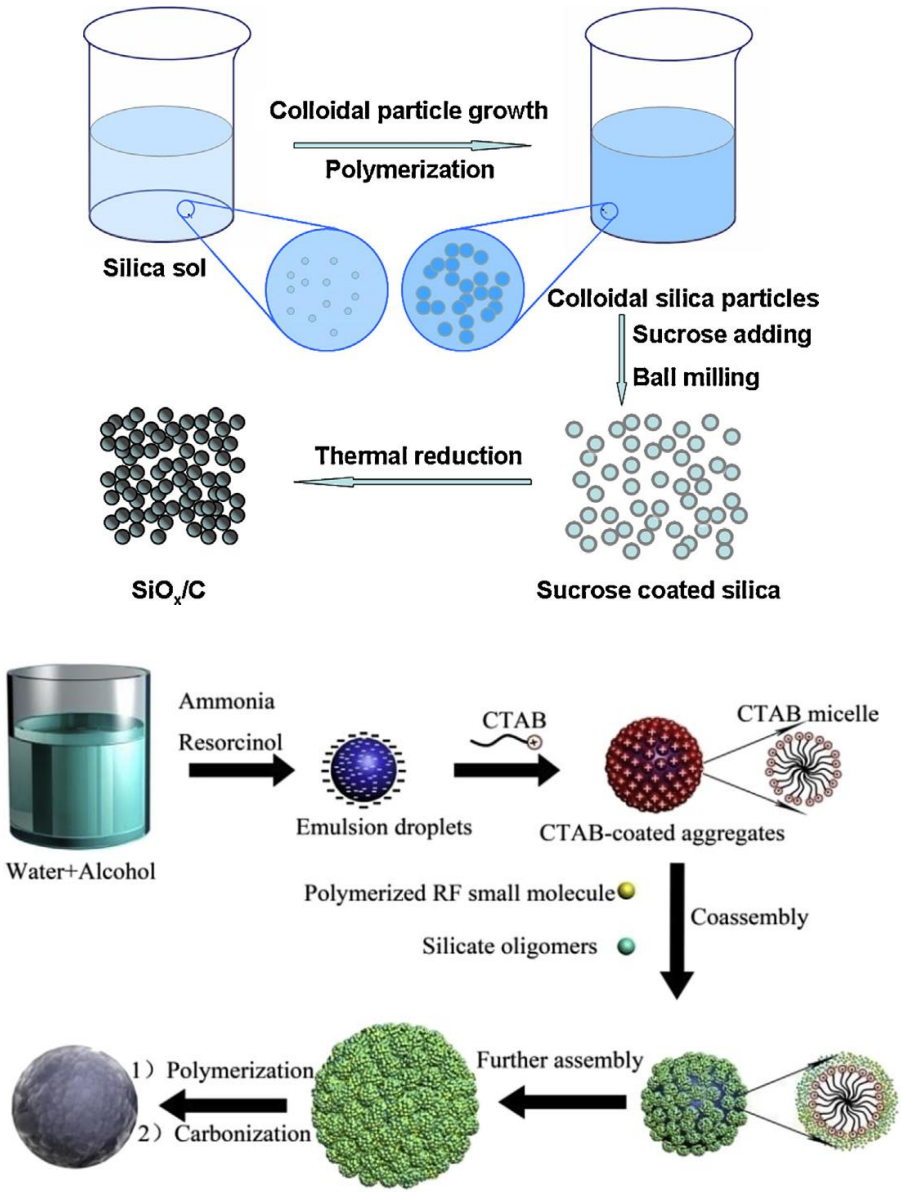

Figure 5.3. (a) Schematic representation of the fabrication process for SiO_x/C composite. Reproduced with permission [245]. Copyright 2015, Elsevier. (b) Preparation process of sugar apple-shaped SiO_x/C spheres. Reproduced with permission [167]. Copyright 2015, Elsevier.

Recently Cui *et al*. [62] reported the synthesis of SiO_x/C composite from renewable rice husks via aluminothermic reduction. Silica, which naturally exists as nanoparticles, is assimilated from soil in the form of silicic acid during the growth of rice and uniformly deposited on the cell wall material as a polymer of hydrated and amorphous silica, as shown in **Figure 4**. Rice husks powder were carbonized after pretreatment, activated with $ZnCl_2$ to obtain porous carbonized rice husks powder, then directly reduced using Al powder to obtain porous SiO_x/C samples. The composited showed excellent cyclability maintaining 1230 mAh g^{-1} at 100 mA g^{-1} rate, and capacity retention of 98.1% after 200 cycles, which was superior to several SiO_x/C composites synthesize via TEOS precursor route [167, 245, 256]. The low ICE of 45.04% was mainly ascribed to the generation of excess Li_4SiO_4 and Li_2O. The utilization of bio-renewable resources brings new perspectives into synthesis of low-cost SiO_x/C composites with high performance. In conclusion, SiO_x/C composites are promising through means of facile synthesis routes resulting in low fabrication costs and potential for scale up. Carbon coatings and matrix also increases inter-particular connection of SiO_x while providing high electronic conductivity, allowing for good cyclability and rate capability. But carbon coatings does not adequately address the problem of low ICE, as most ICEs of SiO_x/C composites mentioned in this section are lower than 60%, severely hindering their practicability in commercial applications [234].

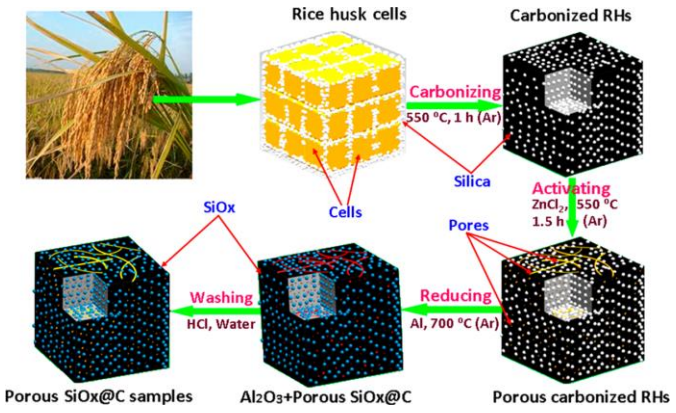

Figure 5.4. Synthesis of SiO_x/C composites from rice husks. Reproduced with permission [62]. Copyright 2016, Elsevier.

5.2.2 Si/SiO_x core-shell nanocomposite electrodes

Another potential morphology is the Si/SiO_x core-shell composite which may provide more stability for cycling Si and prevent separation unlike soft matrixes such as carbon [258]. As early as 2007, Zhang *et al*. [258] synthesized a Si/SiO core-shell nanocomposite by coating Si nanoparticles with sol-gel and following heat treatment. The composite showed better cycling properties than pure Si as the SiO layer can form Li silicates, serving as a buffer to alleviate volume expansion of the Si nanoparticles. Combining soft carbon coating with SiO_x coating, Hu *et al*. [259] synthesized $Si@SiO_x/C$ nanocomposite by hydrothermally carbonizing the mixture of Si nanoparticles, glucose, and water, with the TEM images shown in Figure 5.5. The specific capacity of the composite can be maintained at 600 mAh g^{-1} after 200 cycles at a high specific current of 1 A g^{-1}. Both SiO_x and carbon acted as volume expansion zones and contributed to the long cycle life. Another multi-layered $Si/SiO_x/SiO_2$ nanocomposite was synthesized by Dai *et al*. [260] using $SiCl_4$ as the Si precursor and sodium potassium alloy (NaK) as the reducing agent. The specific capacity at 200 mA g^{-1} can be maintained at 600 mAh g^{-1} after 350 cycles with a high coulombic efficiency of >99% owing to its unique nanostructure.

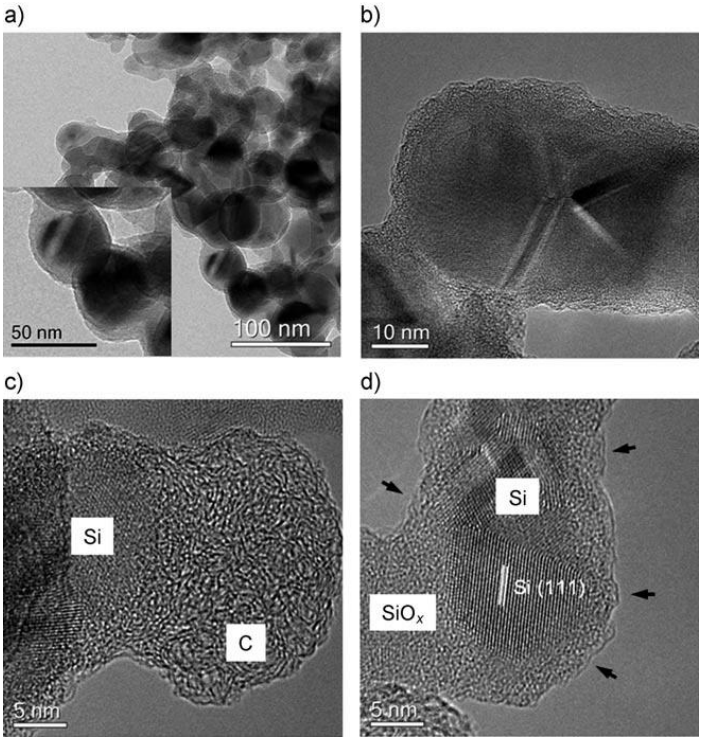

Figure 5.5. TEM images of the Si@SiO_x/C nanocomposite. a) overview of the nanocomposite and a TEM image at higher magnification (insert) showing uniform sphere-like particles. b) HRTEM image clearly showing the core/shell structure. c), d) HRTEM image displaying details of the Si nanoparticles coated with SiO_x and carbon. Reproduced with permission [259]. Copyright 2008, Wiley and Sons.

Similarly Lee *et al.* [261] synthesized highly stable multi-component Si-SiO-SiO_2 particles with Si/SiO_x core and a crystalline SiO_2 shell from commercially available SiO_x bulk particles via a thermal annealing process in the presence of sodium hydroxide (NaOH). Both the Si and the SiO_2 crystalline sizes formed increased with an increasing amount of NaOH. When coated with a carbon layer via thermal decomposition of acetylene gas, the multi-component particles showed excellent cyclability with a capacity retention of 99.5% after 200 cycles with a reversible charge capacity of 1280 mAh g^{-1}. Recently, Park *et al.* [235] sought to increase both capacity retention and ICE by synthesizing Si nanocrystal-embedded SiO_x nanocomposite. The duals-size Si/Si-SiO_x composite were prepared by simple addition of commercial Si nanoparticles

during a sol-gel reaction of triethoxysilane followed by heat treatment at 1000 °C. Triethoxysilane decomposed into a Si/SiO_x layer 20-30 nm thick encompassing Si nanoparticles after the heat treatment. The addition of Si nanoparticles into the Si/SiO_x nanocomposite significantly increased ICE to 59.2%-73.6% (dependent on Si nanoparticle size), higher than that of 47.6% of Si/SiO_x alone. The dual-size composites also displayed good cyclability, retaining up to 1500 mAh g^{-1} even after 100 cycles. It was also shown that a carbon coating could further enhance capacity retention by ensuring good electrical conduction. In summary, creating Si/SiO_x-based nanocomposites through wet chemistry routes can be attractive, however the bulk Si in the composite core still contributed to capacity loss due to volume expansion and pulverization.

5.2.3 SiO_x/CNF, SiO_x/CNT, and SiO_x/Graphene electrodes

Si/carbon nanofiber(CNF) composites have been studied due to the high conductivity, mechanical strength, ductility, and long aspect-ratio of carbon nanofibers [262-264]. It is also utilized in SiO_x-based electrodes as Hanai *et al.* [265] prepared ball-milled SiO_x and carbon nanofiber composite electrodes with a reversible capacity of 700 mAh g^{-1} after 200 cycles. They concluded flexible CNFs may function as good electronic contact, and secondly, act as an effective buffer matrix for the volume change of Li_xSi by cycling. Recently Zhang *et al*. [51] demonstrated that high energy ball-milled SiO_x showed superior electrochemical performance of an initial capacity of 1416.8 mAh g^{-1}, with coulombic efficiency ≥99.8% and capacity retention of 83.6% even after 100 cycles when the conductive agent was optimized to contain vapor grown carbon fibers (VGCF) along with KS-6 and Super P carbon black. Carbon nanotubes (CNTs) offer excellent conductivity, high surface area, and mechanical flexibility, and have also been examined in composites with SiO_x. In 2010 Ren *et al*. [266] prepared a SiO_x/graphite/CNT composite electrode that exhibited an initial discharge capacity of 790 mAh g^{-1} with an ICE of 65%. After 100 cycles, a reversible capacity of 495 mAh g^{-1} was retained, which is superior to that of bare

SiO_x electrode. Carbon nanotubes served as excellent volume expansion and contraction buffer for SiO and SiO/graphite particles. Post-cycling SEM analysis also revealed that relatively compact and homogeneous SEI layers were formed on the surface of SiO_x/graphite/CNT electrode and no cracks appeared. In 2016 they further improved the composite performance by combining multiwalled carbon nanotubes (MWCNT) and N-doping, achieving a stable discharge capacity of 620 mAh g^{-1} at 100 mA g^{-1} rate after 450 cycles [186]. MWCNTs served as a highly conductive and porous scaffold facilitating electron transport, while N-doped carbons improved the electric contact between SiO_x/MWCNT particles and prevented the physical and electrochemical agglomeration of SiO_x. SiO_x/CNT&CNF by Li *et al*. [267] and SiO@CNF&graphite by Hou *et al*. [170] showed also showed good electrochemical performances.

Besides CNFs and CNTs, graphene is another highly promising candidate to enhance SiO_x electrochemical performance due to its mechanical flexibility, chemical stability, and excellent conductivity [268]. Nguyen *et al*. [269] first reported on carbon fiber-interwoven amorphous nano-SiO_x/graphene composite prepared by a simple room temperature synthesis of amorphous SiO_x nanoparticles using silica, followed by their homogeneous dispersion with graphene nanosheets and carbon fibers in aqueous system. TEM and SEM images revealed that SiO_x nanoparticles 20-30 nm in diameter and graphene sheets were interwoven with carbon fibers into secondary particles of 200-300 nm in diameter. As a result of this interconnected nanoparticle-conductive bedding nanostructure the composite exhibited impressive cycling performance, delivering discharge capacities of 1263-1579 mAh g^{-1} at the C/5 rate with capacity retention of 80% over 50 cycles. Guo *et al*. [55] combined carbon coated SiO_x with reduced graphene oxide (RGO) into SiO_x/C@RGO nanoparticles. Through FE-SEM the authors observed the insertion of SiO_x/C nanoparticles into disorderly stacked layer-by-layer RGO and by TEM adherence or embedding of SiO_x/C nanoparticles to RGO layers. The SiOx/C@RGO anode

delivers a capacity of 2402.9 mAh g^{-1} in the first charge and 1225.5 mAh g^{-1} in the first discharge process. The rather large capacity was attributed to enhanced surface area (additional storage of Li-ions in the defects) or stacking of the nanoscale composites [55]. A high reversible capacity of 1264 mAh g^{-1} was observed after 400 cycles, which is 84.3% of the fifth cycle. The authors attributed the good electrochemical performance to the 3D conducting network formed by RGO. Further SiO_x/graphene composite by Yuan *et al*. [270] and SiO_x/RGO composite by Bai *et al*. [171], showed good electrochemical performances and confirmed the effectiveness of graphene in facilitating electron and Li ion transport and mechanical durability in composites of such kind.

5.2.4 Si/SiO_x nanotubes, wires, and rods as electrodes

Nanotubular structured Si bear a great potential to be applied in LIBs because the axial void buffer naturally provides additional space for expansion during lithiation and delithiation, and thus preventing the pulverization of Si [40, 45]. In addition, the Li diffusion length is greatly reduced for the nanostructures with high aspect ratio, allowing for fast ion transfer and rate kinetics. These advantages also hold true for SiO_x tubular nanostructures. In 2012 Guo *et al*. [271] first synthesized hollow tubular SiO_x by using cellulose fibers as template. TEOS and sol-gel precursors were slowly suction filtered in sequence through a piece of cellulose filter paper to ensure adequate growth of nanometer-thick SiO_x layer on cellulose fibers, after which the entire filter paper was heat treated at 650 °C for 6 h to remove the original paper template. The obtained white sheets composed of SiO_x nanotubes was tested electrochemically, which showed discharge capacities of 810 and 740 mAh g^{-1} at the current densities of 200 and 500 mA g^{-1}, respectively. Stable discharge capacities of 940 mAh g^{-1} and the coulombic efficiencies of 98.7-99.5% were obtained at the current density of 100 mA g^{-1}. The Park group developed a novel method to synthesize large-scale interconnected Si/SiO_x nanowire anodes for LIBs via thermal disproportionation of SiO with metal-catalyzed Si nanowire growth [272]. Bulk SiO_x particles

were first disproportionated into Si nanocrystals and SiO_2 matrix, then coated with Ni nanoparticles to act as nucleation sites for Si nanowire growth via vapor-liquid-solid (VLS) mechanism. Through this method, lab-scale mass production of >10 g Si/SiO_x nanowires a few hundred nanometers in width and tens-of-micrometers in length can be obtained in one batch. When coated with carbon, these nanowires showed first cycle charge and discharge capacities of 2360 mAh g^{-1} and 1570 mAh g^{-1}, respectively, with an ICE of 66.5%. Highly stable cycling of the electrodes was seen at 0.1 C, and 0.2 C for 150 cycles without significant capacity loss. Even at a high rate of 10 C, specific capacity of 1180 mAh g^{-1} was recorded, highlighting the influence of nanowire nanostructure on improving rate kinetics. In 2014 the Park group further developed a catalyst free method to synthesize the Si/SiO_x nanowire anodes by a simple evaporation of Si monoxide and substrate temperature control, as catalysts can be a source of contamination in nanowire based devices [273]. The growth of $Si\text{-}SiO_x$ nanowires directly on Cu substrate in a three heat zone furnace without catalysts can be generally described as an oxide-assisted growth mechanism, although with details not yet fully understood [274, 275]. The Si/SiO_x nanowire anodes showed excellent electrochemical performance, with a reversible capacity of ~1000 mAh g^{-1} even at a high-rate of 5 C (1 C = 3.7 A g^{-1}). Another SiO_x nanowire synthesis method was proposed by Li *et al*. [61] using self-sacrifice of bimodal mesoporous silica (BMS). Under the effecting of amine vapor etching, Fe^{3+} from $FeCl_3$ were loaded in the pores of BMS and acted as catalyst for SiO_x nanowire growth on the surface of BMS spheres along the direction of (001) crystal plane. They also synthesized $p\text{-}SiO_2$ NPs (porous silica nanoparticles), $pC\text{-}p\text{-}SiO_2$ NPs (porous silica nanoparticles with porous carbon coating), $nC\text{-}SiO_x$ NWs (SiO_x with no carbon coating), and $pC\text{-}SiO_x$ NWs (SiO_x nanowires with porous carbon coating) for comparison as shown in Figure 5.6. The $pC\text{-}SiO_x$ NWs synthesized using the self-sacrificial method performed substantially better and retained 1060 mAh g^{-1} after 100 cycles, showing the beneficial synergic effect of nanowire nanostructure and porous carbon coating. Ren *et al*. [60] synthesized SiO_x

nanorod electrodes via a template assisted hydrothermal route followed by heat treatment that exhibited a discharge capacity of about 720 mAh g^{-1} after 350 cycles at a current density of 100 mA g^{-1}. The excellent results of these 1D SiO_x nanostructures confirm the advantages of electrode material with long aspect ratio and short Li diffusion length, also the more complicated synthesis process and limitations to scale-up needs to be addressed in further works.

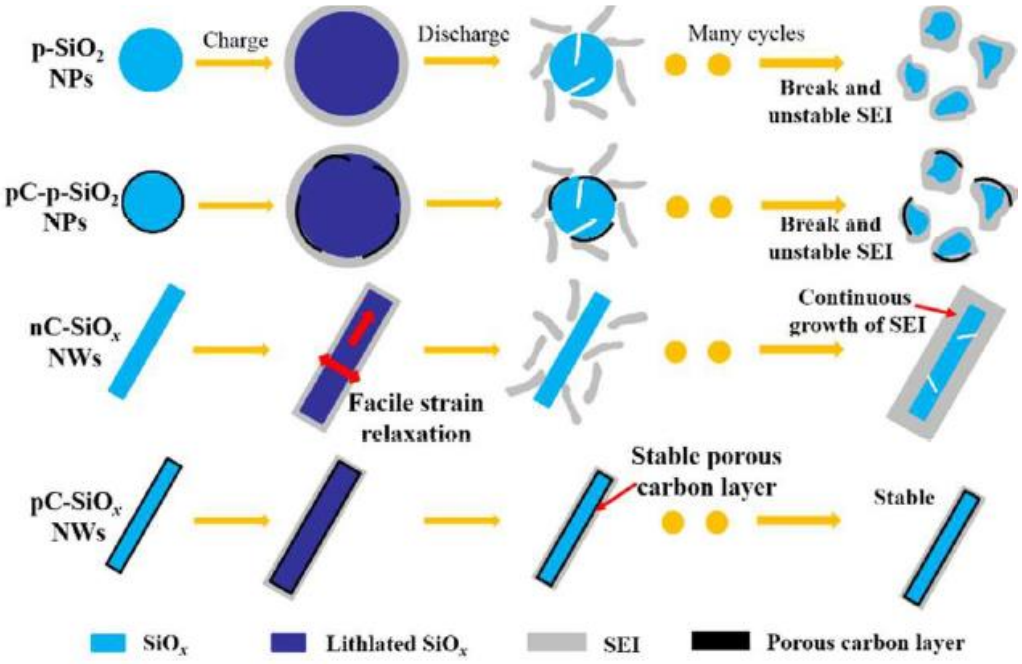

Figure 5.6. Schematic illustration of different SiO_x nanostructures before and after charge-discharge cycling, indicating that pC-SiO_x nanowires have more stable structure during electrochemical cycling. Reproduced with permission [61]. Copyright 2017, Royal Society of Chemistry.

5.2.5 Porous SiO_x electrodes

Since Si/SiO_x experience volume expansions during lithiation and delithiation, generating porous structures is an effective method to alleviate detrimental effects from it by providing extra free

space. Lee *et al*. [276] employed three-dimensional porous SiO_x as anodes synthesized via combination of galvanic displacement reaction and metal-assisted chemical etching. Silver nanoparticles that act as catalyst were deposited on the surface of SiO_x via a galvanic reaction. Subsequently, the silver-deposited SiO_x particles were chemically etched to synthesize porous SiO_x particles, without changing the chemical and physical properties of SiO_x. After carbon coating, the electrodes delivered high specific capacity of 1520 mAh g^{-1}, a stable cycling retention (reversible capacity of 1490 mAh g^{-1} after 50 cycles), and a high rate capability (74% at 3 C rate compared to 0.1 C rate). In 2013 Yu *et al.* [241] enhanced the electrochemical performance of pristine SiO_x particles by surface etching with NaOH. The SiO_x powder etched under 1 M NaOH for 2 h as electrodes showed dramatically enhanced electrochemical performance, maintaining 1260 mAh g^{-1} after 50 cycles. Later the authors developed a new approach to synthesize porous SiO_x by chemical etching of Si crystallites [277]. Crystalline Si and Si oxides from disproportionation of SiO_x acted as pore-generating agent and self-template, respectively, since etching rates of nano-size crystalline Si and amorphous Si oxides are different when etched with NaOH. By controlling etching time, nc-Si were attacked more aggressively by NaOH leaving leave pores while SiO_x was dissolved only slightly. The porous SiO_x electrode exhibited a stable reversible capacity of about 1240 mAh g^{-1} over 100 cycles at 0.2 C. A porous SiO_x electrode with arrayed mesoporous architecture was developed by Gao *et al*. [256]. Due to the bipolar feature of CTAB molecules, they self-assembled onto the large polyvinylpyrrolidone (PVP) solution to form micellar rods with hydrophilic group outside. TEOS was then introduced onto the micellar rods as Si precursor and silica precursor with mesoporous structure was produced after hydrothermal reaction. Sucrose solution was further introduced to provide carbon coating after heat treatment. The mesoporous SiO_x with carbon coating showed excellent electrochemical performance and stable cycling with 780 mAh g^{-1} was achieved for more than 350 cycles. Recently a highly resilient mesoporous carbon coated SiO_x anode prepared by oil-

water templating was reported by Park *et al* [57]. During the synthesis process, hydrophobic oil droplets dispersed throughout triethoxysilane containing the precursor solution was trapped inside hydrogen silsesquioxane (HSQ) after completion of the sol-gel reaction of triethoxysilane [57]. Oil droplets was important both for the generation of mesopores in the SiO_x matrix and to act as the precursor for a carbon layer on the surface of porous SiO_x. As a result of high porosity, the anode exhibited capacity of 730 mAh g^{-1} and outstanding cycling performance over 100 cycles without significant change in structure as observed with SEM.

5.2.6 Other SiO_x electrodes

A W-coated SiO_x/graphite composite anode was developed by Yom *et al* [236]. Tungsten has been applied in various industries because of its superior conductivity ($18.9x10^6$ S m^{-1}) compared to Ni and graphite [278-280]. The W-coated SiO_x/graphite electrode showed a capacity retention of 63.2% for 100 discharging/charge cycles whereas the uncoated SiO/graphite electrode exhibited a retention capacity of 52%. The W-coated SiO_x/graphite electrode also showed an undamaged surface with no cracks. Besides W coating, Cr coating was also applied in SiO_x electrodes [246].

Yamamura *et al*. [281] studied the reduction effect of irreversible capacity on SiO_x electrode by heat reaction with Fe_2O_3. The authors reported that low ICE of a-SiO_x may be because the amorphous structure has an oxygen defect and distortion of SiO_4 tetrahedral [206]. Therefore for supplying oxygen to SiO under an inert atmosphere to reduce oxygen defects, Fe_2O_3 was chosen because Si has been used as a reducing element for the reduction for reduction of Fe_2O_3 in the steel industry [282]. When the molecular ratio of SiO: Fe_2O_3=1:0.2, an uniform Fe_2SiO_4 layer 50-100 nm thick was formed on Si surface. The performance of this SiO_x+ Fe_2O_3 material showed that the Li-insertion capacity was 2095 mAh g^{-1}, the Li-extraction capacity was

1900 mAh g^{-1}, and the charge-discharge efficiency had significantly improved from 70% to 90%. More studies would be required for the exact mechanism of this heat treatment.

Zhang *et al*. [226] developed a novel SiO_x/SiO_y bilayer nanomembrane which exhibited a reversible capacity of about 1300 mAh g^{-1} at a current density of 100 mA g^{-1}, an excellent stability of over 100 cycles, as well as good rate capability. The design of rolled up alternating layers of Si-rich and O-rich SiO_x allowed for high capacity, fast Li ion transport, and good volume expansion resistance. The design is also attractive because it is based on industry-compatible think film deposition techniques.

Homma *et al*. [283] studied the effect of CH_4 addition into Si/SiO_x production by plasma spray physical vapor deposition (PS-PVD). The addition of CH_4 into precursor vapor was effective in lowering energies of Si(g) so it became the most stable Si-containing phase, in effect promoting SiO reduction and thereby increasing the volume of core nc-Si allowing higher specific capacity of the composite. However, as a result of CH_4 addition at high temperatures a SiC inactive phase was formed and an optimal C/Si ratio was necessary to realize the best electrochemical performance. The amount of CH_4 addition at C/Si=0.25 seemed to be in the optimal range to produce an enlarged nc-Si core with reduced SiO_x shell while suppressing inactive SiC formation.

5.3 Effect of other LIB components on SiO_x-based anode performance besides nanostructuring

The optimal design of nanostructured SiO_x electrodes are not the only factor in the final electrochemical performance of the assembled LIBs. In this chapter, some other variables and conditions that influence the performance of SiO_x electrodes are reviewed.

5.3.1 Effect of additives on SiO_x electrode performance

A common problem associated with Si and SiO_x based electrodes are the growth of a SEI layer by reductive decomposition of the electrolyte solution during charge process [195, 282], and continuous growth of that SEI film due to continuous crack formation after the first charge-discharge cycle, exposing new surfaces to the electrolyte. To address this problem in 2006 Choi *et al*. [195] studied the effect of fluoroethylene carbonate (FEC) on Li/Si thin film cell electrochemical performance. The ICE for the cell with 3 wt% FEC additives was improved from 87.8 to 88.7%, and notably discharge capacity retention from 67.9% to 88.5% at end of 80 cycles. The addition of FEC additive produced a less porous surface structure after cycling, and thus decreased total surface area exposed to electrolyte for side reactions. Through XPS analysis it is identified that electrodes with FEC additives formed more stable SEI components such as LiF and -Si-F compounds, while electrodes without FEC additives formed less stable surfaces such as LiP_xF_y and ethylene carbonate (EC)-derivatives [195]. Since the report FEC additives have been utilized in a wide range of Si-based electrode studies. Vinylene carbonate (VC) is another effective additive primarily targeted at graphite electrodes [284], but also utilized for Si-based electrodes by Chen *et al* [30, 285]. Although less LiF is formed in VC containing electrolyte cells which may contradict the effect of FEC additives, higher intensity of XPS peaks attributed to SiO_x was also observed in VC containing electrolyte cells compared to VC free cells, hinting that stabilizing effect of SiO_x maybe one of the reasons for the enhancing effect of VC [285].

Because SiO_x-based electrodes is in effect nanocrystalline Si surrounded by SiO_x matrix, FEC [59, 168, 228, 273, 277], VC [207, 248, 286], or a combination of FEC and VC [51, 60, 186, 287] as additives were commonly seen in the literature after 2006 in half cells for its stabilization properties. Interestingly, there are also many reports where additives were not used at all [52, 56, 57, 61, 185, 188, 217, 270, 283] for SiO_x electrodes while it has became the norm for Si

electrodes. The sensible reason behind this is that in Si-based anodes only a thin layer of native SiO_x thick exists and it is not enough to withstand the large volume expansions of Si during lithiation/delithiation. In SiO_x-based electrodes Si does not exist as a bulk crystal, but often were uniformed dispersed in an inactive SiO_x matrix much more robust and thicker than Si-based anodes so only a small fraction of pure Si could be directly exposed to electrolyte leading to side reactions. In this case the effect of additives in performance enhancement of SiO_x electrodes could be much less significant than in Si electrodes, although no comprehensive study was conducted on the matter. However Hu *et al*. [259] compared the electrochemical performance of a $Si@SiO_x/C$ electrode with and without VC additives, where the electrode performance was substantially improved with VC addition. They attributed the results to the mechanically and electrochemically stable SEI layer formed due to the existence of both a SiO_x layer and 10-20 nm thick carbon shell.

Table 5.2 summarized some recent studies where SiO_x full cell performance was evaluated to study various variables. It could be seen that additives were used in only a few studies. Specifically, VC was added to the electrolyte for the high temperature SiO_x full cell studies in ref [286] because its proven effectiveness in enhancing cycling life of LIBs under elevated temperature conditions [284, 288, 289]. In the rest of the studies SiO_x full cells without additives still performed well. It might be interesting to see further work exploring the effectiveness of additives in SiO_x electrodes with regards to different nanostructured geometry, Si/O ratio, and existence of C coatings.

A non FEC/EC siloxane forming additive tris(2-methoxyethoxy)vinylsilane (TMVS) was studied by Nguyen *et al*. [218]. It was found through ex situ ATR IR spectroscopy that the use of TMVS additive induced thickening of the SEI layer by mainly organic compounds (e.g., alkyl carbonate and carboxylate salts) and Li_2CO_3. They believed the surface siloxane network constructed at the electrode surface provided the effect of surface protection from acid attack.

With TMVS additive, SiO_x particles also appeared aggregated and interconnected with little cracking, indicating that TMVS is also effective in providing mechanical robustness. Together improved electrochemical performances were observed for cells with TMVS additives.

5.3.2 Effect of non-conventional binders on SiO_x electrode performance

Si electrodes works poorly with traditional poly(vinylidene fluoride) (PVDF) binders, as a result a number of binders has been evaluated for Si electrodes, including sodium carboxymethyl cellulose (NaCMC) [39], polyacrylic acid (PAA) [33], polyimide imide [54], and alginate [31]. Alginate, a major constituent of brown algae, enables better cycling of Si electrodes by 1) inducing only weak interactions between the binder and the electrolyte; 2) providing access of Li^+ to the Si surface; 3) assisting in building a deformable and stable SEI layer on the Si surface. Overall significant electrochemical cycling performance was observed by the development of the binders. For SiO_x electrodes they were also applied, for example CMC [55, 56] , PAA [51, 57], polyimide imide [58, 59], and alginate [60]. PVDF is still used in some SiO_x electrode works, such as [52, 61, 62]. Guerfi *et al*. [63] studied the effect of three types of binders, PVDF, CMC-based water dispersed binder (WDB), and polyimide on SiO_x/C or SiO_x/C-graphite (1:1 w:w) composite electrode electrochemical performance. The average size of the SiO_x particles was 7 µm. The highest 1st cycle reversible capacity was found in cells containing polyimide (1026 mAh g^{-1}), followed by WDB (817 mAh g^{-1}) and then PVDF (472 mAh g^{-1}). The cell with WDB had the highest 1st cycle CE, followed by polyimide and then PVDF. Through cross section in situ SEM, obvious disintegration of SiO_x particles and cracks due to cycling was observed for both electrodes.

Table 5.2 Summary of SiO_x-based full cell studies

Anode material	Cathode material	Electrolyte +additive	Specific capacity (mAh g^{-1})	Primary research focus	Current density	Cycle Number	Capacity retention	Ref
Ni, Fe, Ti-doped SiO	$Li_{0.8}Mn_{0.8}Ni_{0.2}O_{2.2}$	EC/DEC (3:7 v:v)	1260 (anode)	Effect of metal doping	1 C	400	82% (SiO-Ni)	[243]
SiO/C thin film	$Li_{1/3}Co_{1/3}Mn_{1/3}Ni_{1/3}O_2$/LiCoO$_2$ (7:3)	EC/DEC (3:7 v:v)	400-2100(Anode)	Performance of carbon coated SiO	0.5 C	100	10-50%	[250]
SiO	$LiFePO_4$	PC/GBL (1:2 v:v)	150 (Cathode)	Performance of heat treated SiO	0.2 C	600	90%	[215]
SiO/C	$LiNi_{0.8}Co_{0.15}Al_{0.05}O_2$	EC/DEC/EMC	254-931 (anode)	Cut-off voltage and	1 C	500	25.4-92.4%	[290]

				deterioration mechanism				
SiO/C	$LiCoO_2$	EC/DEC (1:1 v:v)	1500 (anode)	Li coating prelithiation on the separator	0.1 C	100	69%	[230]
SiO/C	$LiNi_{0.8}Co_{0.15}Al_{0.05}O_2$	EC/DEC/EMC	830-940 (anode)	Temperature-UCV dependence	1C	500	80%	[291]
SiO	$Li_{1/3}Co_{1/3}Mn_{1/3}Ni_{1/3}O_2$	EC/DEC (3:7 w:w)/30% FEC	150 (full cell)	Functional conductive binder, SLMP prelithiation	C/3	100	73%	[66]
SiO-Li	$LiNi_{0.8}Co_{0.15}Al_{0.05}O_2$	EC/DEC(1:1 w:w)/5 wt% FEC	165 (cathode)	Scalable prelithiation	1 C	100	61%	[228]

				technique effect on ICE Pairing of irreversible capacity of anode/cathode				
SiO/Si	LR-NMC	EC/DEC (1:1 v:v)/VC/MB	150 (cathode)		0.5 C	165	88%	[286]
SiO/Li powder	$LiCoO_2$	EC/DEC (1:1)	1012 (anode)	Prelithiation by SiO/Li powder reaction	C/50	15	74.7%	[56]

The authors confirm that there is difference in electrochemical performance when different binders were used with SiO_x, however a limited number of cycles and fixed SiO_x size was reported in the study. Komaba *et al.* [64] studied the effect of PAA, CMCNa, poly(vinyl alcohol) PVA, and PVDF binder on SiO_x cycling with a larger number of cycles. PAA binder showed the best performance as the reversible capacity reached 700-750 mAh g^{-1} for 50 cycles at a rate of 100 mA g^{-1}. SiO_x particles with the three other binders lost almost all of its capacity after 50 cycles. Through synergized analysis of XRD, electron microscopy, XPS, IR, and adhesive strength test, the authors attributed the good results to amorphous PAA being not only able to tightly bind, but also cover individual SiO_x particles. Additionally, PAA binder had a suppressing effect on electrode deformation compared to the PVDF binder. The schematic illustration is shown in Figure 5.7. In 2013 Feng *et al*. [65] also studied alginate, CMC, and PAA binder performance with SiO_x/C or SiO_x electrodes and confirmed their beneficial effect in enhancing capacity retention due to their amorphous structure and high adhesion strength related to ester-like bonds. The best performance was seen when SiO_x/C electrode was combined with alginate or CMC binder.

Another non-conventional binder worth mentioning is functional conductive polymer binder poly(9,9-dioctylfluorene-*co*-fluorenone-*co*-methylbenzoic ester) (PFM) [66]. The polar ester functional group, which is designed for the adhesion with the SiO_2 surface, is especially suitable for SiO electrode material because it forms chemical bonding with the hydroxide terminated SiO_2 surface on via a trans-esterification reaction. Thus, the highly conductive polymer binder solves both the problem of low conductivity of SiO_x material and disconnection between active material and binder due to excessive volume change. As a result, reversible capacity of 1000 mAh g^{-1} for over 400 cycles with a 2% to 10% PFM was realized in the half cell. By using the conductive polymer binder PFM, the loading of active material SiO_x in the anode could be up to 98%, which realized capacities ~3 times higher than graphite in half cell. With

addition of SLMP prelithiation Li powder, a SiO_x/NMC full cell was able to maintain a reversible capacity of ~110 mAh g^{-1} after more than 100 cycles at C/3, highlighting excellent properties of the binder.

In summary, development and systematic studies of non-conventional binders are important in harnessing the full potential of SiO_x electrodes. While non-PVDF binders exhibited enhancement in many SiO_x electrode reports, they do not explain the good performance of SiO_x with PVDF in other studies [52, 61, 62]. Whether non-traditional binders are superior likely depends on the Si distribution, degree of disproportionation, nanostructure, and surface modification of the SiO_x particles.

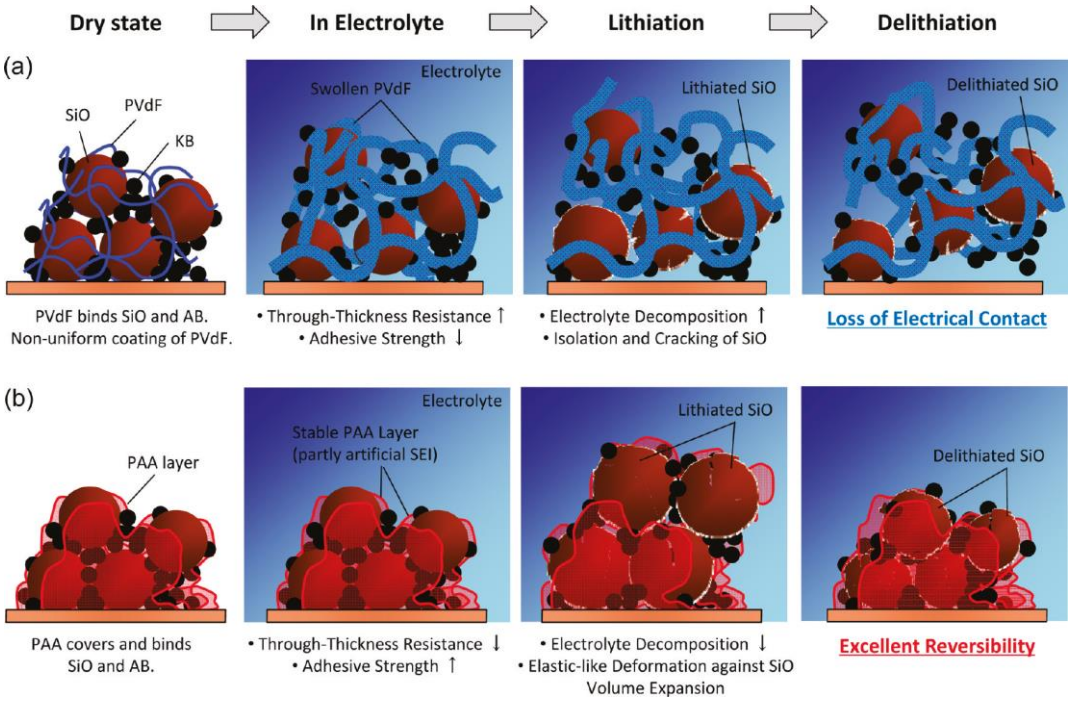

Figure 5.7. Schematic illustrations of the proposed mechanism for the improved cyclability for the SiO powder composite electrodes; (a) PVDF and (b) PAA binders. Reproduced with permission [64]. Copyright 2011, American Chemical Society.

5.3.3 Effect of doping on SiO_x electrode performance

Heteroatom doping in carbons can increase Li storage by creating defects, which may serve as active sites for Li storage. Nitrogen-doping (N-doping) also leads to increase of d-spacing between graphitic layers, which facilitates the transport of Li [292]. Additionally, N-doping could enhance the electronic conductivity of carbon, enhancing rate capabilities of carbon materials as anodes [293]. As such, N-doped graphene for ultracapacitors [294], N-doped multiwalled carbon nanotubes for Li storage [292], N-rich carbons derived from protein for ultra-high capacity anode and supercapacitor [293], and N-doped carbon nanosheets from silk for anodes and supercapacitor [295] have been developed.

Because carbon coatings are important in SiO_x electrodes as it provide high conductivity, surface protection, and a ductile matrix to accommodate volume change, it is a natural step to study doped carbon coatings as a means to enhance SiO_x electrode performance. Lee *et al*. [168] first reported N-doped carbon coatings on SiO_x particles by using a nitrogen-containing ionic liquid (IL), 1-ethyl-3-methylimidazolium dicyanamide (EMI-DCA) as nitrogen precursor material. The initial reversible discharge capacities are 1258, 1429, and 1496 mAh g^{-1} for bare SiO, C-SiO, and N-doped C-SiO respectively, corresponding to ICE of 58.4, 72.3, and 73.9%. Long term cycling retention was also improved, as NC-SiO showed 955 mAh g^{-1} after 200 cycles when cycled at 1 C, whereas C-SiO and bare SiO showed 813 mAh g^{-1} and 545 mAh g^{-1} respectively. While the difference between bare SiO and carbon coated SiO is expected, the capacity difference of 142 mAh g^{-1} between N-doped C-SiO and C-SiO is noteworthy. The authors attributed the results to enhanced electronic conductivity originating from C-N and C=N bonds which was observed by XPS, and was shown previously to increase electronic conductivity via excess electrons at nitrogen sites [294, 296]. EIS measurements also confirmed the increased conductivity, as the charge transfer resistance for the N-doped C-SiO was smaller than C-SiO

during initial cycles and the discrepancy enlarged after further cycling. Wang *et al*. [173] synthesized binder-free anodes of micro-nano Si/SiO_x with N-doped carbons by using polyacrylonitrile (PAN) as nitrogen precursor. SiO_x particles was thoroughly mixed with PAN to form a viscous slurry to be coated on Cu substrate, then dried and post-annealed to obtain the composite electrode. The composite electrode showed excellent electrochemical performance with a high initial reversible capacity (2734 mAh g^{-1} with 75% ICE), stable cycling (988 mAh g^{-1} after 100 cycles), and good rate capability (800 mAh g^{-1} at 1 A g^{-1} rate). Shi *et al*. [180] developed a scalable method to synthesize core-shell SiO_x/N-doped carbon composite with excellent electrochemical performance. Dopamine hydrochloride was polymerized in the presence of oxygen onto SiO_x as N-doped carbon precursor. The composite electrode delivered a reversible capacity of 1514 mAh g-1 after 100 cycles at a current density of 100mA g^{-1} and 933 mAh g^{-1} at 2 A g^{-1}.

Woo *et al*. [297] studied the effect of boron doping in SiO_x electrode performance by a direct spin-on dopants (SOD) technique without boron powder (B_2O_3) and carbon coating. The boron diffusion in a gaseous phase and disproportionation reaction inside all SiO was simultaneous completed in one heat treatment. A Raman shift of Si peak from 508 cm^{-1} for un-doped SiO sample to 498 cm^{-1} for B doped SiO was clearly observed due to the stress applied in the surrounding Si atomic structure after B-doping. Based on this the authors suggests that boron atoms exist in the form of doping rather than in the form of boron particles. The boron doped SiO displayed significantly improved electrochemical performance, with the initial reversible capacity being 1804 mAh g^{-1} with an ICE of 65.1% and less than 10% capacity loss during 100 charge/discharge cycles. Based on results from EIS measurement, the lower impedance coefficient (σ_ω) and Li diffusion coefficient (D_{Li}) of boron-doped SiO_x compared to un-doped SiO_x was also calculated and identified. This study shows that boron-doping can be just as

effective as carbon coatings in SiO_x anodes by strongly influencing the electronic conductivity and Li diffusion rates.

5.3.4 Effect of prelithiation on SiO_x electrode performance

One of the main challenges to SiO_x electrodes is the low ICE resulting from formation of inactive Li silicates, Li oxide, and SEI. In half cell, it is often not a problem as more active material could be loaded to reach a certain areal capacity. In full cell, low ICE leads to the consumption of excess amount of cathode material to compensate for the first cycle thus significantly reduce energy density. Compensating for the low ICE by increasing cathode loading is also impractical due to result of kinetic limitations on the cathode thickness and inherently lower cathode capacity compared to anode (<200 mAh g^{-1}) [52, 298]. Thus, there is a strong demand to improve SiO_x LIB overall ICE by preloading anode electrode with excess Li to compensate for its low ICE. Yang *et al*. [299] improved ICE of SiO_x anode by in situ mechanochemical reduction with SiO_x and Li metal. SiO_x and Li metal starting material was mixed and ball-milled in an argon filled glove box, then heat treated at 500 °C under vacuum for 5 h. The end product is a powder with a mixture of phases according to equation 4 [299]: Li_2O, Li_4SiO_4, and Si.

$$5SiO + 6Li = Li_2O + Li_4SiO_4 + 4Si \qquad (4)$$

The advantage of this method is 1) in situ formation of nano-sized Si (<10nm); 2) effective buffering of volume changes owing to the existence of Li-rich component matrix; 3) high reversible capacity with greatly improved ICE as a result of mechanochemical reduction. As a result, the initial charge capacity of the composite electrode reached 770.4 mAh g^{-1} with ICE of 81%. In 2009 Seong *et al*. [234] pre-lithiated carbon coated SiO_x electrode by surface coating Li powder synthesized from droplet emulsion technique (DET). Subsequently the Li-coated electrode was heated at 60 °C for 48 h to induce reaction between Li powder and SiO_x. Through the pre-lithiating process, rest potential of SiO_x/C was lowered from 3.15 V to 1.84 V, along with

formation of Li oxide and Li silicates. This pre-lithiation method increased ICE from 67.7% to 72.8%. The authors further proposed a different pre-doping technique by forming double layer anode (DLA) of independent SiO_x layer and Li powder layer [233]. Li powder was emulsified in DMC and coated onto Cu substrate foil. Then the SiO_x layer was placed on top of the Li powder layer, separated in between by a Cu mesh. SEM images showed that after the pre-lithiation conditioning process the Li powder disappeared, having fully lithiated into SiO_x active material. As a result of this novel double layer configuration the ICE was dramatically improved from 54.92% of that of SiO_x anode to 101.07% of the Li-SiO_x double layer anode.

Alternatively, a commercial Li powder SLMP was utilized as a prelithiation agent in SiO_x electrodes. Jarvis and Gao *et al*. [300, 301] developed a scheme to corporate fine Li metal powder into active anode host material (e.g. Si, Sn, tin oxides or composite tin alloys), later developed into the commercial product SLMP Li powder. The SLMP Li powder is sealed with a thin layer of Li_2CO_3 to limit the exposure of Li to ambient environment. Upon contact with electrolyte, spontaneous partial lithiation of the anode active materials occurs along with SEI formation. This prelithiation method greatly reduces Li consumption from the cathode side and increase ICE of the whole LIB cell. Therefore, it has been coupled with Si-C nanotube anode [232], graphite anode [188, 231], and more recently SiO_x anode [66]. SiO_x electrode with the PFM binder was also examined in full cell setup with $Li_{1/3}Co_{1/3}Mn1_{/3}Ni_{1/3}O_2$ (NMC) as cathode and SLMP microsize Li powder as the anode prelithiation agent [301]. The ICE increased from 48% to 90% with SLMP, and the SiO_x/NMC full cell maintained a reversible capacity of ~110 mAh g^{-1} after more than 100 cycles at C/3.

Recently Zhao *et al*. [52, 227, 229] synthesized dry air and ambient air stable Li silicide-Li oxide (Li_xSi/Li_2O) composites as prelithiation reagents via one step metallurgical process from SiO or SiO_2 and Li metal foil. The composite revealed a unique structure with homogeneously dispersed active Li_xSi nanodomains in inactive Li_2O matrix, which gave the composite

exceptional stability in both dry air and ambient air. The superior stability compared to previously developed core-shell Li_xSi/Li_2O (Figure 5.8(a) top row) [229] or Li_xSi with SEI (Figure 5.8(A) middle row) [227] was attributed to the highly crystalline Li_2O matrix formed at high temperature and the enlarged contact area between Li_2O and Li_xSi as shown in Figure 5.8(A) bottom row and Figure 5.8(B). DFT simulations showed that binding energies between O at different positions was lower than Li-Si bonds as shown in Figure 5.8(C)(D), therefore, enlarging the contact area between Li_2O and Li_xSi has the benefit of stabilization of Li in $Li_{21}Si_5$ nanodomains. Furthermore, since Li_xSi nanodomains are uniformly dispersed in Li_2O matrix, smaller consequences would be brought to the reactivity of the entire Li_xSi/Li_2O composite by a surface breach than to core-shell structured Li_xSi/Li_2O composite. As a result, the composite showed excellent performance as prelithiation agent in SiO_x anode. The ICE of SiO_x: Li-SiO_x anode (Li-SiO_x: Li_xSi/Li_2O composite, Li-SiO:SiO:SuperP:PVDF=10:55:20:15) was increased to 93.8% from 52.6% of SiO_x control. Based on mass of Si, the retention capacity after 400 cycles was ~1509 mAh g^{-1} at rate of C/2. A few reasons contributed to the good capacity retention: 1) Li_xSi nanodomains was pre-formed during Li_xSi/Li_2O synthesis, and sufficient space was already created before electrochemical stimuli; 2) Small domain size reduces effect of pulverization or squeezing between Li_xSi, and surrounding Li_2O acted as a good mechanical buffer; 3) Li_2O served as an artificial SEI to reduce side reactions between Li_xSi and electrolyte.

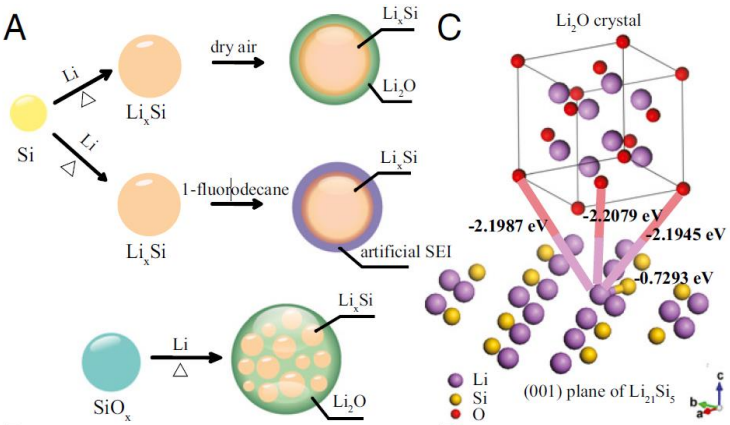

Bonds	Binding energy (eV)
(½ ½ 0) O-Li	-2.2079
(0 0 0) O-Li	-2.1945
(1 1 0) O-Li	-2.1987
Si-Li	-0.7293

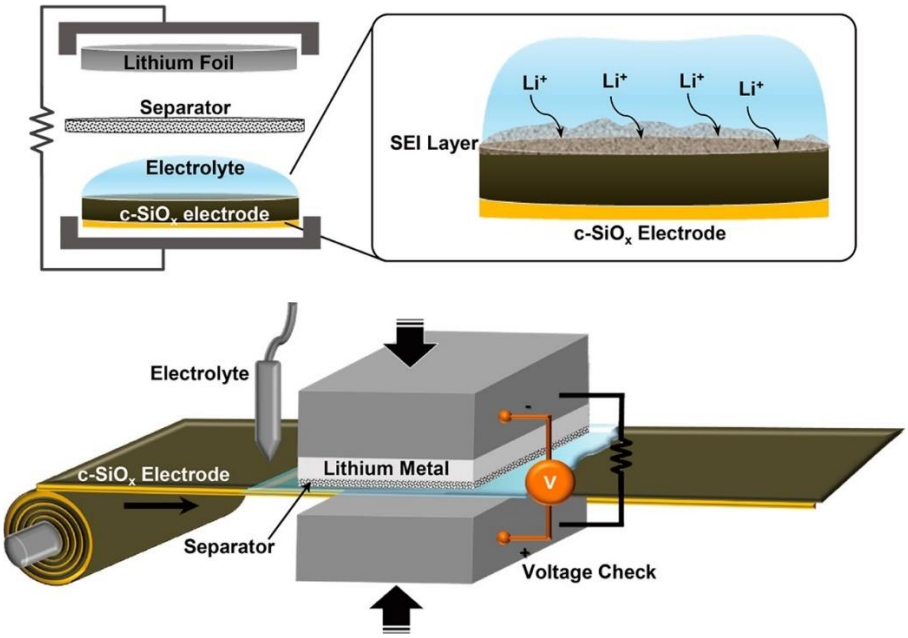

E

Figure 5.8. Schematic diagrams and DFT simulation showing the advantages of Li_xSi/Li_2O composites. (A)Three approaches to stabilize reactive Li_xSi NPs. (B) The different behaviors of Li_xSi/Li_2O composite and Li_xSi/Li_2O core shell NPs under the ambient condition. (C) DFT

simulation is performed by cleaving along the (001) plane of $Li_{21}Si_5$ and calculating the binding energy between O at different positions in Li_2O and Li at the (001) plane of $Li_{21}Si_5$. (D) The table shows the binding energy of different bonds. Reproduced with permission [52]. Copyright 2016, Proceedings of the National Academy of Sciences. (E) Graphical illustration of prelithiation process of c-SiO_x electrode and its scalable roll-to-roll process scheme. Reproduced with permission [228]. Copyright 2015, American Chemical Society.

Kim *et al*. [228] developed a novel controlled prelithiation method with scalable roll-to-roll process, which is shown in Figure 5.8(E). The authors pointed out that a proper degree of prelithiation is very critical for stable operations. While insufficient lithiation does not improve ICE enough, overlithiation removes the possibility of accepting Li ions during the actual alloying reaction in the first cycle. An optimized prelithiation point would be one where the final potential does not lead to electrolyte decomposition and SEI formation, but above the potential needed for the main alloying reaction. To achieve this goal, The pristine electrode was designed to be prelithiated via an electrical short with Li metal foil in the presence of a optimized electrical resistance while simultaneously monitoring the voltage between both electrodes [228]. By studying a) lithiation voltage profile when different resistances are used; b) OCV of electrodes after 10 h relaxation with respect to prelithiation time; c) the first cycle capacities after different prelithiation time, the optimal external electrical resistance and prelithiation time could be determined. A clear relationship between specific capacity, lithiation time, and ICE was also summarized where the ICE could be tuned from 73.6% to 107.9%. Although cycling capacity retention rates did not vary due to prelithiation in half cells, the prelithiated electrode showed both better ICE and CE in the few following cycles. According to time-of-flight secondary ion mass spectrometry (TOF-SIMS), the SEI layer derived from prelithiation is thicker and has more inorganic species such as LiF and Li_2O, since during the prelithiation protocol current is varying as compared to constant current during normal charge process.

Hwang *et al*. [230] proposed a different prelithiation approach by coating Li onto a separator (monolayer Polypropylene (PP)). The SiO_x electrode ICE could be adjusted from 66.4% to 90.8% by changing the Li prelithiation powder loading from 0 mg cm^{-2} to 1.5 mg cm^{-2} in a SiO_x/C-LCO full cell setup. Post cycling SEM images showed that all the Li powder disappeared from the separator and was fully used to compensate for the irreversible loss. The authors also showed that the Li coating prelithiation technique could be utilized for graphite and Si electrodes, and is effective in raising Si electrode ICE from 67.8% to 86.6%.

5.3.5 SiO_x electrode full cell performance

SiO_x electrodes are very promising in half-cells using Li foil as the counter electrode due to their excellent cyclability. Nonetheless, it is essential before commercialization to test their electrochemical performance in full cells utilizing high capacity cathode materials as the counter electrode. Previous studies on Si based electrodes in full cells have shown that often their full cell performance is inferior compared to half-cell performances due to mechanisms as parasitic reactions at the anode, Li trapping, or unstable SEI [147, 149, 225, 302]. Table 5.2 summarized some of the research effort in studying various aspects of SiO_x based anodes in full cell environment.

Miyachi *et al*. [243] first co-evaporated SiO_x with Fe, Ni, or Ti metal, then an additional Li layer on substrate as the anode in an effort to study whether the low ICE of SiO_x was due to its low electron conductivity. A few conclusions were drawn from the study. First, the capacity retention of all the metal-doped SiO_x anodes was as high as 82% after 400 cycles with $Li_{0.8}Mn_{0.8}Ni_{0.2}O_{2.2}$ as the cathode. Secondly, the metal doped anodes had ICEs of higher than 84%, as compared to 50% of un-doped SiO_x. Thirdly, Si^0 and Si^{4+} were the primary Si 2p valence states in the metal-doped SiO_x electrode. During charge and discharge, the ratios of S^0 and S^{4+} changes as a result of lithiation and delithiation. The doped metal makes a percolating conduction

patch through the material, greatly increasing its conductivity and also helps the diffusion of Li^+ in the electrode, easing the changes from Si^{4+} to Si^0 and back. Therefore, the authors drew the conclusion that the improved ICE and capacity retention resulted from the increase in conductivity as a result of metal-doping.

Yamada *et al*. [250] studied the performance of carbon coated SiO_x-carbon composite electrode assembled with a mixture of $Li_{1/3}Co_{1/3}Mn1_{/3}Ni_{1/3}O_2$ and $LiCoO_2$ as cathode. SiO_x-carbon composite was prepared by mechanical grinding and mixing of SiO, graphite, carbon fiber, and polyethylene powder (to make pores in the composite), then carbon coating by thermal vapor deposition. The SiO_x-carbon composite showed best cycling performance, with 700 mAh g^{-1} retained after 100 cycles, a capacity retention rate of 85%. As comparison, a simple mixture of SiO_x-graphite only retained 65% capacity after 100 cycles and pristine SiO_x 20% after only 20 cycles. This study showed that a mechanical mixture of SiO_x with high conductivity carbon materials and carbon coating is extremely effective in enhancing SiO_x full cell performance.

Kajita *et al*. [290] studied the optimal cutoff voltage of carbon coated SiO_x anode paired with $LiNi_{0.8}Co_{0.15}Al_{0.05}O_2$ cathode and proposed different deterioration mechanism when the cell was run under different operating temperatures. Two lower cutoff voltages (LCV), 2.5 V or 3.0 V, and three upper cutoff voltages (UCV), 4.0 V, 4.1 V, 4.2 V were studied. At 20 °C, all cells with lower cutoff voltage (LCV) of 3.0 V had good cyclability at 500 cycles with capacity retention rates from 90.7 to 92.1%. Interestingly, at 20 °C with 2.5 V as LCV, cells with 4.0 V UCV deteriorated faster than cells with 4.1 V or 4.2 V UCV. This result was contrary to the expectation that cells with lower UCV should show better cycling performance because of the smaller volume changes and damage to the electrode. At 60 °C, all cells with UCV of 4.2 V deteriorated significantly. Based on combined analysis from STEM, energy-dispersive X-ray spectroscopy (EDX), electron energy loss spectroscopy (EELS), and dQ dV_{-1} results, the authors proposed that the main deterioration mechanism at 20 °C is the exfoliation of SiO_x at low LCV

which became a resistance and caused capacity fading. The dominant cause for deterioration at 60 °C is the decomposition of electrolyte.

Yamano *et al*. [286] evaluated the cell design and safety of SiO_x-Si composite anode with Li-Rich NMC cathode as full cells. The Li-Rich NMC is a promising cathode material due to its high capacity above 200 mAh g^{-1} over 4.5 V [303], but faces similar low ICE problem like SiO_x anode due to Li_2O removal from the structure. It would be interesting to match the low ICE of SiO_x and Li-Rich NMC cathode in full cells and gauge their relative performance. The low ICE of SiO_x however cannot be fully compensated by the low ICE of Li-Rich NMC, therefore a composite of Si/SiO_x was used as the anode. The cell using the composite electrode of Si-SiO_x/Li-Rich NMC displayed a discharge capacity of 182 mAh g^{-1} as the cathode capacity at 0.1 C rate, and a stable cycle performance for over 100 cycles with a discharge capacity of ca. 150 mAh g^{-1} at the 0.5 C rate and 30 °C. Non-room temperature electrochemical performance of the cell at -55 °C, 60 °C, and 80 °C was also good. To test the safety of the high capacity cell, 1 Ah laminated charged pouch cell went through nail penetration test. Results show that no significant cell voltage change was monitored, and the nail internal temperature and cell surface temperature increased to only 55 °C and 28 °C, respectively. Both metrics was superior to a control cell using graphite as the anode. Based on experimental results, it was postulated that the lithiated SiO and Si could immediately transform from a conductive phase to a low electrical conductive phase after discharge, resulting in the superior safety of Si-SiO_x/Li-Rich NMC LIB cell.

Additionally, the excellent full cell performance of prelithiated SiO_x electrodes [228, 230] and SiO_x electrodes with a novel binder [66] was discussed previously. Based the existing literature of full cell studies, it is convincing that SiO_x have great potential in commercialization as the next generation anode material.

5.4 Investigation of SiO_x-based electrode failure mechanisms

Due to the complexity of components in SiO_x-based anodes, extensive studies have been taken to reveal its operation and degradation mechanism. SEM, TEM, XPS, neutron elastic scattering, etc. are common methods used to explore the fading mechanisms of SiO_x-based anodes, and most studies before 2013 was summarized in table in ref [205]. In this section, a few of the more recent studies on fading mechanisms of SiO_x-based anodes are reviewed.

Choi *et al*. [184] studied the fading mechanisms of carbon coated Si/SiO_x electrode by XRD, TEM, SEM, and qualitative and quantitative STEM-EDX. A theory of global fading and local fading mode was suggested, as shown in Figure 5.9. Specifically, local fading refers to the loss of contact between individual Si and SiO_x with the conducting carbon or themselves due to the large volume expansion/contraction during charge-discharge. Global fading refers to the collapse of the entire electrode, such as crumbling of Si/SiO_x or the exfoliation of the entire electrode. It was found that the electrochemical cycling of Si/SiO_x electrode was divided into several phases: 1) an initial activation phase from cycle 1 to cycle 10 where CE gradually increased. This was attributed to the morphological change of Si/SiO_x electrode and electrolyte decomposition; 2) loss of both CE and capacity from cycle 11 to cycle 29. Local and global fading modes both existed from the 1st to the 29th cycle. 3) After the 29th cycle, a high CE (>99%) was reached while capacity decreased gradually. This was correlated with only the global fading mode because Li^+ could only diffuse into still connected Si/SiO_x particles, therefore the CE was consistently high. The electrochemical behavior was supported by qualitative and quantitative SEM-EDX results.

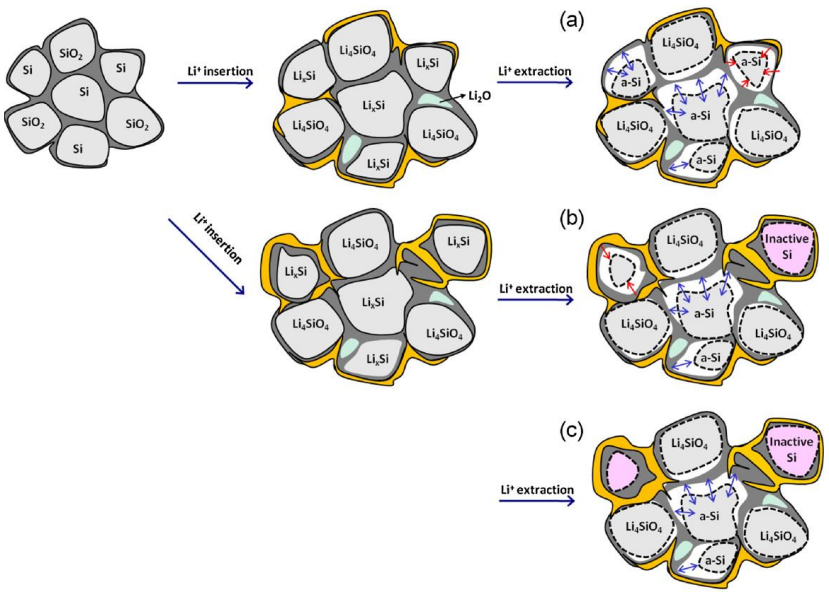

Figure 5.9. Depiction of (a) a local fading mode, (b) a global fading mode with local fading, (c) global fading mode only. Reproduced with permission [184]. Copyright 2012, Elsevier.

Phillipe *et al*. [304] deployed hard and soft XPS to study interfacial mechanisms in Si nanoparticles with a layer of SiO_2, which resembled disproportionated SiO_x nanostructures and is helpful in the understanding of SEI formation mechanisms. Soft XPS photon energies ranged from 50 to 1500 eV and hard XPS photon energies ranged from 2000 eV to 10000 eV. Since the inelastic mean free path of photoelectrons is highly dependent on their kinetic energy, soft and hard XPS corresponded to chemical analysis at the extreme surface or bulk of the particles. This technique has the advantage of non-destructiveness compared to commonly used argon-ion sputtering for depth profiling. Based on the Si 2p spectrum analysis during charge/discharge, reaction of Li with Si leading to reduction of surface oxide is confirmed, summarized in equation 5 [305]:

$$SiO_2 + 4Li \rightarrow Si + 2Li_2O \quad (5)$$

The appearance of Si 2p signals at 100.9 eV and 102.3 eV in the outer SiO_2 shell after charge/discharge pointed to the formation of Li_4SiO_4 and Li_2SiO_3. Based on the relative strength

of the signals, it was proposed that Li_4SiO_4 is likely formed in this case, with a mechanism shown in equation 6:

$$SiO_2 + 4Li \rightarrow Si + 2Li_4SiO_4 \qquad (6)$$

Through the analysis and comparison of O 1s peaks with Si 2p peaks, the relative location and formation timelines of SEI, Li oxide, Li silicates, and lithiated Si were determined, as shown in Figure 5.10. Specifically, at the beginning of charge (0.5 V vs Li^+/Li), Li has not yet reacted with Si but a thin SEI layer had already formed, which constituted the outmost layer of the studied particle system. After further charge at the beginning of the low voltage plateau (0.1 V vs Li^+/Li), the thickness of the SEI increased while Li started to react with Si and Si oxide. The reaction of Li with Si oxide resulted in the formation of Li_2O and Li_xSiO_y, most probably Li_4SiO_4. These species formed the intermediate layer between the outmost SEI and inner Si/lithiated Si. After full charge (0.01 V vs Li^+/Li), the Li-Si alloying process is almost complete. The amount of Li_2O continuously increased toward the end of charge, but some unreacted SiO_2 still remains at the surface. After full discharge (0.9 V vs Li^+/Li), Li has been fully extracted from the core, and Li_2O has disappeared while Li_4SiO_4 remained. This nondestructive depth profiling analysis technique combining hard and soft XPS analysis is promising in the study of interfacial mechanisms not only in Si and SiO_x anodes, but also foreseeably other electrode materials.

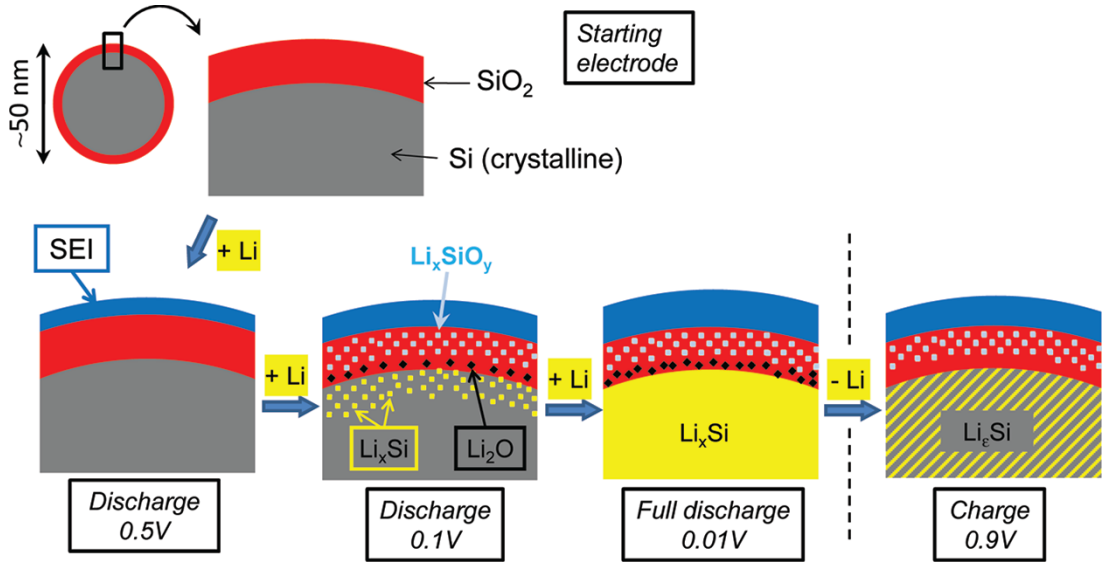

Figure 5.10. Schematic view of the mechanisms occurring at the surface of Si nanoparticles. Formation of the SEI at the beginning of charge. Formation of the Li-Si alloy upon further charge, together with Li_2O and Li_xSiO_y interfacial phases. Partial reversibility upon discharge. Reproduced with permission [304]. Copyright 2012, American Chemical Society.

Jung *et al*. [49] elucidated lithiation mechanisms of SiO_x nanowires at the atomic scale based on molecular dynamics (MD) simulations employing the ReaxFF reactive force field developed through first-principles calculations. They found that Li atoms interacted with the amorphous out SiO_2 layer to form Li_2O and Li_4SiO_4, which agreed with previous studies. Interestingly, it appeared that Li atoms can actually escape from Li_4SiO_4 into the crystalline Si core for reactions. It was also found that an amorphous layer of SiO_2 ~1 nm thick can suppress the volume expansion of the SiO_2 nanowire during lithiation process. This is because the mobility of an interface between amorphous Li_xSi and amorphous Li_ySiO_2 which existed toward the outside of the nanowire is slower than an inner interface formed between crystalline Si and amorphous Li_xSi. The stronger stiffness of amorphous SiO_2 (37GPa) also changed the stress distribution of the particle and exerted a compressive force to retard the tensile strength of amorphous Li_xSi cores, resulting in suppression of the volume expansion of the nanowire as a

whole. This molecular simulation study explained theoretically the observed lower volume expansion of Si nanowires with native SiO_2 [306].

Yoo *et al*. [185] studied the microstructure influence of SiO_x and carbon coated disproportionated SiO_x on electrochemical performance using confocal μ-Raman spectroscopy. Spectra obtained from vibration modes with confocal μ-Raman spectroscopy can provide information about chemical composition and crystallinity of a sample that has amorphous and crystalline phases, which is ideal for the study of lithiation/delithiation of SiO_x electrodes. In this study, bare SiO_x shows inhomogeneous distribution of amorphous Si and crystalline Si. Some particles in the bare SiO_x consist of loose amorphous Si phase that contains a local disordering with Si-O bonding but other particles consist of mainly micro-sized crystalline Si. The carbon coated disproportionated SiO_x showed a much more homogeneous configuration of nanocrystalline Si with small portion of locally disordered amorphous Si and SiO_2 matrix. As the result carbon coated disproportionated SiO_x displayed superior electrochemical properties, which understood well with previous studies [181, 242].

5.5 Conclusions and outlook

SiO_x is a promising class of anode materials that combines high capacity and good cyclability due to its general Si-cluster/SiO_2 matrix nanostructure. Nanocrystalline Si clusters that are uniformed dispersed through the SiO_2 matrix provide high capacity and the overall volume expansion effect also decreased due to the spreading and smaller sizes of Si crystallites. SiO_2 and Li silicates, Li oxide formed during lithiation provided a matrix to protect Si from contact with SEI. Furthermore, the formation of such a homogeneous matrix provided accommodation for stress from lithiation/delithiation and led to the superior cyclability of SiO_x electrodes. However, SiO_x electrodes also suffer from low ICE, low conductivity, and moderate damage brought by volume change during lithiation/delithiation. To alleviate these problems, a range of nanostructuring

techniques and approaches were developed, such as carbon coating, prelithiation, and compositing with conductive materials. In general, carbon coating is an effective method to improve the conductivity of SiO_x electrodes while protecting the surface. Carbon coating can also be applied by a variety of techniques such as CVD or wet chemistry routes, and do not interfere with other modifications of the SiO_x electrode. Prelithiation is very important in raising the ICE of SiO_x electrode, which is essential in full cell configurations and commercialization.

In order to further progress the practicability of SiO_x electrodes, a lot of studies are still required. First, more comprehensive understanding of the lithiation/delithiation mechanisms in the Si core and oxide surface is required in order to develop the optimal nanostructure. This may be accomplished through the experimental techniques mentioned afore, such as hard and soft XPS and μ-Raman spectroscopy, and molecular simulations. In situ microscopy techniques such as SEM and TEM imaging is also important in understanding of SiO_x electrode morphology evolution, which is used in the studies of Si electrodes [307]. Secondly, comprehensive studies on the optimal cycling conditions and cathode interaction of SiO_x electrodes is important to realize its full potential. Thirdly, alternative binders, electrolyte, and additives should be tailored to fit the distinctive attributes of SiO_x electrodes. Finally, consideration should be given to decrease the complexity of various nanostructures to enable low-cost SiO_x electrodes with high performance.

Chapter 6 Conclusions

This dissertation describes the development of Si and SiO_x-based composite anodes with lignin as the precursor for both the conductive agent and binder for the first time. It was found that Si-lignin composite electrodes showed good electrochemical performance in half cells, with capacity retention of ~80% after 100 cycles, which is superior or equal to many reports with conventional electrode designs with Si as the active electrode material. Although the capacity of SiO_x-lignin composite electrodes were lower, much better electrochemical cycling performance was observed, and stable capacities of ~900 mAh g^{-1} could be retained even after 250 cycles. This could be attributed to the more uniform dispersion of Si active nanocrystals and smaller volume changes in the SiO_x material, in which lignin derived carbon matrix was more proficient in accommodating the volume changes and preserving the electrode structure.

The carbon matrix derived from heat treated lignin provided Si and SiO_x particles with a highly conductive and flexible hosting matrix, which is beneficial because 1) the large volume changes of Si and SiO_x particles are partially addressed, leading to improved electrochemical performance; 2) valorization of lignin, a low cost, renewable biopolymer which is produced in large quantities, is realized as the structural material in high performance LIB anode. Apart from the use of lignin in LIB anode active material, Na ion battery anode, and supercapacitors, this dissertation revealed new possibilities in incorporating lignin into high performance energy applications. The author highly believes that the future is emphasized with green and renewable approaches to technological advancements, and the potential of lignin and related biopolymers are just beginning to be realized by the scientific community. This dissertation will hopefully inspire others into related fields.

Although good performance of lignin composite electrodes was demonstrated in this dissertation, there are many technical challenges to be faced before commercial applications can be realized:

1) The loading of the current Si or SiO_x-based electrodes (~2.5 mAh cm^2) are low compared to commercial requirements of ~5 mAh cm^2. Synthesis of Si or SiO_x-lignin composite electrodes with higher loadings may result in segregation of Si and SiO_x from the lignin matrix resulting in deteriorated performance. Indeed, this is a problem that faces even conventional graphite or cathode electrodes. A new method to synthesize high loading electrodes need to be developed, as currently multilayer or thicker films resulted in uneven distribution of Si.
2) As seen in chapter 3, although the half-cell performance of Si-lignin composite electrode is good, the full-cell performance is lackluster due to much more complicated deterioration mechanisms. Artificial coatings such as LiF or Al_2O_3 which can alleviate such deterioration mechanisms for Si-lignin or SiO_x-lignin electrodes are highly desired and would be an interesting topic for future research.
3) A limited set of experimental conditions for Si-lignin and SiO_x-lignin electrodes were studied in this dissertation, and there are many un-answered questions as to the working and failure mechanisms. Currently, too high of a lignin composition in the composite results in excessive Cu substrate curvature and crumbling due to lignin weight loss during heating, and too low of a lignin composition results in poor cycling performance. The use of more flexible Cu substrate would be a possible solution to solve the problem of excessive Cu substrate curvature. It would be interesting to try overcome these barriers and study the performance of Si-lignin and SiO_x-lignin electrodes with varying lignin content in a range where good electronic conductivity can be guaranteed. It might also be interesting to study the effect of different types of lignin on composite electrode performance, and further, altering lignin properties by upstream lignin biosynthesis.

REFERENCES

[1] B. Scrosati, J. Hassoun, Y.K. Sun, Energ Environ Sci, 4 (2011) 3287-3295.
[2] Y. Nishi, J Power Sources, 100 (2001) 101-106.
[3] R. Marom, S.F. Amalraj, N. Leifer, D. Jacob, D. Aurbach, J Mater Chem, 21 (2011) 9938-9954.
[4] B. Scrosati, J. Garche, J Power Sources, 195 (2010) 2419-2430.
[5] M. Armand, J.M. Tarascon, Nature, 451 (2008) 652-657.
[6] T.-H. Kim, J.-S. Park, S.K. Chang, S. Choi, J.H. Ryu, H.-K. Song, Adv Energy Mater, 2 (2012) 860-872.
[7] J.B. Goodenough, K.-S. Park, J Am Chem Soc, 135 (2013) 1167-1176.
[8] M.M. Thackeray, C. Wolverton, E.D. Isaacs, Energ Environ Sci, 5 (2012) 7854-7863.
[9] B. Dunn, H. Kamath, J.-M. Tarascon, Science, 334 (2011) 928-935.
[10] K. Xu, Chem Rev, 114 (2014) 11503-11618.
[11] G. Zheng, in: Y. Cui, T.F. Jaramillo, Z. Bao (Eds.), 2014.
[12] N. Nitta, F. Wu, J.T. Lee, G. Yushin, Mater Today, 18 (2015) 252-264.
[13] D. Lin, Y. Liu, Y. Cui, Nat Nanotechnol, 12 (2017) 194-206.
[14] R. Sengupta, M. Bhattacharya, S. Bandyopadhyay, A.K. Bhowmick, Progress in polymer science, 36 (2011) 638-670.
[15] J.R. Dahn, T. Zheng, Y. Liu, J. Xue, Science, 270 (1995) 590.
[16] D. Aurbach, B. Markovsky, I. Weissman, E. Levi, Y. Ein-Eli, Electrochim Acta, 45 (1999) 67-86.
[17] N. Williard, W. He, C. Hendricks, M. Pecht, Energies, 6 (2013) 4682-4695.
[18] P. Roy, S.K. Srivastava, J Mater Chem A, 3 (2015) 2454-2484.
[19] S. Scharner, W. Weppner, P. Schmid-Beurmann, J Electrochem Soc, 146 (1999) 857-861.
[20] H.-G. Jung, M.W. Jang, J. Hassoun, Y.-K. Sun, B. Scrosati, Nat Commun, 2 (2011) 516.
[21] M. Winter, J.O. Besenhard, Electrochim Acta, 45 (1999) 31-50.
[22] L. Baggetto, P.H. Notten, J Electrochem Soc, 156 (2009) A169-A175.
[23] B. Laforge, L. Levan-Jodin, R. Salot, A. Billard, J Electrochem Soc, 155 (2008) A181-A188.
[24] C.J. Wen, R.A. Huggins, J Electrochem Soc, 128 (1981) 1636-1641.
[25] M.N. Obrovac, L. Christensen, Electrochem Solid St, 7 (2004) A93-A96.
[26] T. Chen, Q. Zhang, J. Xu, J. Pan, Y.-T. Cheng, Rsc Adv, 6 (2016) 29308-29313.
[27] T. Chen, Q. Zhang, J. Pan, J. Xu, Y. Liu, M. Al-Shroofy, Y.-T. Cheng, Acs Appl Mater Inter, 8 (2016) 32341-32348.
[28] U. Kasavajjula, C.S. Wang, A.J. Appleby, J Power Sources, 163 (2007) 1003-1039.
[29] A. Bordes, K. Eom, T.F. Fuller, J Power Sources, 257 (2014) 163-169.
[30] L. Chen, K. Wang, X. Xie, J. Xie, J Power Sources, 174 (2007) 538-543.
[31] I. Kovalenko, B. Zdyrko, A. Magasinski, B. Hertzberg, Z. Milicev, R. Burtovyy, I. Luzinov, G. Yushin, Science, 334 (2011) 75-79.
[32] J.S. Bridel, T. Azais, M. Morcrette, J.M. Tarascon, D. Larcher, Chem Mater, 22 (2010) 1229-1241.
[33] A. Magasinski, B. Zdyrko, I. Kovalenko, B. Hertzberg, R. Burtovyy, C.F. Huebner, T.F. Fuller, I. Luzinov, G. Yushin, Acs Appl Mater Inter, 2 (2010) 3004-3010.
[34] A. Jain, S.P. Ong, G. Hautier, W. Chen, W.D. Richards, S. Dacek, S. Cholia, D. Gunter, D. Skinner, G. Ceder, Apl Materials, 1 (2013) 011002.
[35] J. Xu, (2016).
[36] M. Thackeray, J. Vaughey, L.M. Fransson, JOM Journal of the Minerals, Metals and Materials Society, 54 (2002) 20-23.
[37] M. Obrovac, V. Chevrier, Chem Rev, 114 (2014) 11444-11502.

[38] J.K. Lee, C. Oh, N. Kim, J.-Y. Hwang, Y.-K. Sun, J Mater Chem A, 4 (2016) 5366-5384.
[39] J. Li, R.B. Lewis, J.R. Dahn, Electrochem Solid St, 10 (2007) A17-A20.
[40] X. Su, Q. Wu, J. Li, X. Xiao, A. Lott, W. Lu, B.W. Sheldon, J. Wu, Adv Energy Mater, 4 (2014).
[41] Z. Bao, M.R. Weatherspoon, S. Shian, Y. Cai, P.D. Graham, S.M. Allan, G. Ahmad, M.B. Dickerson, B.C. Church, Z. Kang, Nature, 446 (2007) 172-175.
[42] L. Su, Y. Jing, Z. Zhou, Nanoscale, 3 (2011) 3967-3983.
[43] S.-L. Chou, J.-Z. Wang, M. Choucair, H.-K. Liu, J.A. Stride, S.-X. Dou, Electrochemistry Communications, 12 (2010) 303-306.
[44] W. Wang, P.N. Kumta, Acs Nano, 4 (2010) 2233-2241.
[45] H. Wu, G. Chan, J.W. Choi, Y. Yao, M.T. McDowell, S.W. Lee, A. Jackson, Y. Yang, L. Hu, Y. Cui, Nat Nanotechnol, 7 (2012) 310-315.
[46] C.K. Chan, H. Peng, G. Liu, K. McIlwrath, X.F. Zhang, R.A. Huggins, Y. Cui, Nat Nanotechnol, 3 (2008) 31-35.
[47] S. Ohara, J. Suzuki, K. Sekine, T. Takamura, J Power Sources, 136 (2004) 303-306.
[48] A. Hirata, S. Kohara, T. Asada, M. Arao, C. Yogi, H. Imai, Y. Tan, T. Fujita, M. Chen, Nat Commun, 7 (2016).
[49] H. Jung, B.C. Yeo, K.-R. Lee, S.S. Han, Phys Chem Chem Phys, 18 (2016) 32078-32086.
[50] J.-H. Kim, C.-M. Park, H. Kim, Y.-J. Kim, H.-J. Sohn, J Electroanal Chem, 661 (2011) 245-249.
[51] J. Zhang, C. Zhang, Z. Liu, J. Zheng, Y. Zuo, C. Xue, C. Li, B. Cheng, J Power Sources, 339 (2017) 86-92.
[52] J. Zhao, H.-W. Lee, J. Sun, K. Yan, Y. Liu, W. Liu, Z. Lu, D. Lin, G. Zhou, Y. Cui, Proceedings of the National Academy of Sciences, (2016) 201603810.
[53] B. China, (2017).
[54] N.-S. Choi, K.H. Yew, W.-U. Choi, S.-S. Kim, J Power Sources, 177 (2008) 590-594.
[55] C. Guo, D. Wang, T. Liu, J. Zhu, X. Lang, J Mater Chem A, 2 (2014) 3521-3527.
[56] J.H. Yom, S.W. Hwang, S.M. Cho, W.Y. Yoon, J Power Sources, 311 (2016) 159-166.
[57] E. Park, M.S. Park, J. Lee, K.J. Kim, G. Jeong, J.H. Kim, Y.J. Kim, H. Kim, Chemsuschem, 8 (2015) 688-694.
[58] R. Yuge, A. Toda, K. Fukatsu, N. Tamura, T. Manako, K. Nakahara, K. Nakano, J Electrochem Soc, 160 (2013) A1789-A1793.
[59] B.-C. Yu, Y. Hwa, C.-M. Park, H.-J. Sohn, J Mater Chem A, 1 (2013) 4820-4825.
[60] Y. Ren, M. Li, J Power Sources, 306 (2016) 459-466.
[61] Z. Li, Q. He, L. He, P. Hu, W. Li, H. Yan, X. Peng, C. Huang, L. Mai, J Mater Chem A, 5 (2017) 4183-4189.
[62] J. Cui, Y. Cui, S. Li, H. Sun, Z. Wen, J. Sun, Acs Appl Mater Inter, 8 (2016) 30239-30247.
[63] A. Guerfi, P. Charest, M. Dontigny, J. Trottier, M. Lagace, P. Hovington, A. Vijh, K. Zaghib, J Power Sources, 196 (2011) 5667-5673.
[64] S. Komaba, K. Shimomura, N. Yabuuchi, T. Ozeki, H. Yui, K. Konno, The Journal of Physical Chemistry C, 115 (2011) 13487-13495.
[65] X. Feng, J. Yang, X. Yu, J. Wang, Y. Nuli, J Solid State Electr, 17 (2013) 2461-2469.
[66] H. Zhao, Z. Wang, P. Lu, M. Jiang, F. Shi, X. Song, Z. Zheng, X. Zhou, Y. Fu, G. Abdelbast, X. Xiao, Z. Liu, V.S. Battaglia, K. Zaghib, G. Liu, Nano Lett, 14 (2014) 6704-6710.
[67] D.M. Piper, T.A. Yersak, S.-B. Son, S.C. Kim, C.S. Kang, K.H. Oh, C. Ban, A.C. Dillon, S.-H. Lee, Adv Energy Mater, 3 (2013) 697-702.
[68] J.F. Kadla, S. Kubo, R.A. Venditti, R.D. Gilbert, A.L. Compere, W. Griffith, Carbon, 40 (2002) 2913-2920.
[69] I. Dallmeyer, F. Ko, J.F. Kadla, J Wood Chem Technol, 30 (2010) 315-329.
[70] A.M. Rouhi, Chem Eng News, 79 (2001) 52-56.
[71] N. Smolarski.

[72] R. Vanholme, B. Demedts, K. Morreel, J. Ralph, W. Boerjan, Plant Physiol, 153 (2010) 895-905.
[73] A.G. Vishtal, A. Kraslawski, Bioresources, 6 (2011) 3547-3568.
[74] R. Mörck, H. Yoshida, K.P. Kringstad, H. Hatakeyama, Holzforschung (Germany, FR), (1986).
[75] G. Milczarek, O. Inganas, Science, 335 (2012) 1468-1471.
[76] A. Pandey, T. Bhaskar, M. Stöcker, R. Sukumaran, Recent advances in thermochemical conversion of biomass, Elsevier, 2015.
[77] W.-J. Liu, H. Jiang, H.-Q. Yu, Green Chem, (2015).
[78] D.L. Greene, Transportation Research Record, 2058 (2008).
[79] W. Qin, J.F. Kadla, J Appl Polym Sci, 126 (2012) E203-E212.
[80] S. Chatterjee, E.B. Jones, A.C. Clingenpeel, A.M. McKenna, O. Rios, N.W. McNutt, D.J. Keffer, A. Johs, Acs Sustain Chem Eng, 2 (2014) 2002-2010.
[81] J. Luo, J. Genco, B. Cole, R. Fort, Bioresources, 6 (2011) 4566-4593.
[82] S. Kubo, J.F. Kadla, J Polym Environ, 13 (2005) 97-105.
[83] J.L. Braun, K.M. Holtman, J.F. Kadla, Carbon, 43 (2005) 385-394.
[84] R. Ruiz-Rosas, J. Bedia, M. Lallave, I.G. Loscertales, A. Barrero, J. Rodriguez-Mirasol, T. Cordero, Carbon, 48 (2010) 696-705.
[85] S.X. Hu, Y.L. Hsieh, J Mater Chem A, 1 (2013) 11279-11288.
[86] D.A. Baker, T.G. Rials, J Appl Polym Sci, 130 (2013) 713-728.
[87] A.J. Ragauskas, G.T. Beckham, M.J. Biddy, R. Chandra, F. Chen, M.F. Davis, B.H. Davison, R.A. Dixon, P. Gilna, M. Keller, Science, 344 (2014) 1246843.
[88] D.H. Nagaraju, T. Rebis, R. Gabrielsson, A. Elfwing, G. Milczarek, O. Inganas, Adv Energy Mater, 4 (2014).
[89] M.R. Arcila-Velez, M.E. Roberts, Chem Mater, 26 (2014) 1601-1607.
[90] S. Admassie, A. Elfwing, E.W.H. Jager, Q.Y. Bao, O. Inganas, J Mater Chem A, 2 (2014) 1974-1979.
[91] W.L. Zhang, J. Yin, Z.Q. Lin, H.B. Lin, H.Y. Lu, Y. Wang, W.M. Huang, Electrochim Acta, 176 (2015) 1136-1142.
[92] Z.Z. Chang, B.J. Yu, C.Y. Wang, Electrochim Acta, 176 (2015) 1352-1357.
[93] W.E. Tenhaeff, O. Rios, K. More, M.A. McGuire, Adv Funct Mater, 24 (2014) 86-94.
[94] E. Irisarri, A. Ponrouch, M.R. Palacin, J Electrochem Soc, 162 (2015) A2476-A2482.
[95] K.L. Hong, L. Qie, R. Zeng, Z.Q. Yi, W. Zhang, D. Wang, W. Yin, C. Wu, Q.J. Fan, W.X. Zhang, Y.H. Huang, J Mater Chem A, 2 (2014) 12733-12738.
[96] N. Sun, H. Liu, B. Xu, J Mater Chem A, (2015).
[97] Y.M. Li, Y.S. Hu, H. Li, L.Q. Chen, X.J. Huang, J Mater Chem A, 4 (2016) 96-104.
[98] J. Jin, S.J. Yu, Z.Q. Shi, C.Y. Wang, C.B. Chong, J Power Sources, 272 (2014) 800-807.
[99] J. Ding, H.L. Wang, Z. Li, K. Cui, D. Karpuzov, X.H. Tan, A. Kohandehghan, D. Mitlin, Energ Environ Sci, 8 (2015) 941-955.
[100] W. Sun, S.M. Lipka, C. Swartz, D. Williams, F. Yang, Carbon, 103 (2016) 181-192.
[101] W. Zhang, H. Lin, Z. Lin, J. Yin, H. Lu, D. Liu, M. Zhao, Chemsuschem, 8 (2015) 2114-2122.
[102] H. Wang, Z.W. Xu, A. Kohandehghan, Z. Li, K. Cui, X.H. Tan, T.J. Stephenson, C.K. King'ondu, C.M.B. Holt, B.C. Olsen, J.K. Tak, D. Harfield, A.O. Anyia, D. Mitlin, Acs Nano, 7 (2013) 5131-5141.
[103] J. Yang, B.F. Wang, K. Wang, Y. Liu, J.Y. Xie, Z.S. Wen, Electrochem Solid St, 6 (2003) A154-A156.
[104] R.K. Sharma, J.B. Wooten, V.L. Baliga, X.H. Lin, W.G. Chan, M.R. Hajaligol, Fuel, 83 (2004) 1469-1482.
[105] H.P. Yang, R. Yan, H.P. Chen, D.H. Lee, C.G. Zheng, Fuel, 86 (2007) 1781-1788.
[106] S. Kubo, J.F. Kadla, J Appl Polym Sci, 98 (2005) 1437-1444.

[107] I. Dallmeyer, F. Ko, J.F. Kadla, Ind Eng Chem Res, 53 (2014) 2697-2705.
[108] K. Chen, Z.H. Bao, J. Shen, G.M. Wu, B. Zhou, K.H. Sandhage, J Mater Chem, 22 (2012) 16196-16200.
[109] T.H. Hwang, Y.M. Lee, B.S. Kong, J.S. Seo, J.W. Choi, Nano Lett, 12 (2012) 802-807.
[110] J.C. Guo, X.L. Chen, C.S. Wang, J Mater Chem, 20 (2010) 5035-5040.
[111] J. Seo, H. Park, K. Shin, S.H. Baeck, Y. Rhym, S.E. Shim, Carbon, 76 (2014) 357-367.
[112] M. Li, X.H. Hou, Y.J. Sha, J. Wang, S.J. Hu, X. Liu, Z.P. Shao, J Power Sources, 248 (2014) 721-728.
[113] L. Zhou, X.J. Lin, T. Huang, A.S. Yu, Electrochim Acta, 116 (2014) 210-216.
[114] X.L. Wang, G. Li, F.M. Hassan, M. Li, K. Feng, X.C. Xiao, Z.W. Chen, J Mater Chem A, 3 (2015) 3962-3967.
[115] D. Aurbach, M.D. Levi, E. Levi, H. Teller, B. Markovsky, G. Salitra, U. Heider, L. Heider, J Electrochem Soc, 145 (1998) 3024-3034.
[116] I. Dallmeyer, L.T. Lin, Y.J. Li, F. Ko, J.F. Kadla, Macromol Mater Eng, 299 (2014) 540-551.
[117] D. Munao, J.W.M. van Erven, M. Valvo, E. Garcia-Tamayo, E.M. Kelder, J Power Sources, 196 (2011) 6695-6702.
[118] H. Wu, G.H. Yu, L.J. Pan, N.A. Liu, M.T. McDowell, Z.A. Bao, Y. Cui, Nat Commun, 4 (2013).
[119] X.L. Chen, X.L. Li, F. Ding, W. Xu, J. Xiao, Y.L. Cao, P. Meduri, J. Liu, G.L. Graff, J.G. Zhang, Nano Lett, 12 (2012) 4124-4130.
[120] Y.S. Hu, R. Demir-Cakan, M.M. Titirici, J.O. Muller, R. Schlogl, M. Antonietti, J. Maier, Angew Chem Int Edit, 47 (2008) 1645-1649.
[121] J. Jin, B.-j. Yu, Z.-q. Shi, C.-y. Wang, C.-b. Chong, J Power Sources, 272 (2014) 800-807.
[122] S.X. Wang, L.P. Yang, L.P. Stubbs, X. Li, C.B. He, Acs Appl Mater Inter, 5 (2013) 12275-12282.
[123] O. Rios, S.K. Martha, M.A. McGuire, W. Tenhaeff, K. More, C. Daniel, J. Nanda, Energy Technol-Ger, 2 (2014) 773-777.
[124] A.K. Roy, M. Zhong, M.G. Schwab, A. Binder, S.S. Venkataraman, Ž. Tomović, Acs Appl Mater Inter, 8 (2016) 7343-7348.
[125] Y.J. Chen, M.Y. Nie, B.L. Lucht, A. Saha, P.R. Guduru, A. Bose, Acs Appl Mater Inter, 6 (2014) 4678-4683.
[126] T. Chen, Q. Zhang, J. Pan, J. Xu, Y. Liu, M. Al-Shroofy, Y.-T. Cheng, Acs Appl Mater Inter, (2016).
[127] U.D.o. Energy, (January 2014).
[128] J. Hassoun, F. Bonaccorso, M. Agostini, M. Angelucci, M.G. Betti, R. Cingolani, M. Gemmi, C. Mariani, S. Panero, V. Pellegrini, B. Scrosati, Nano Lett, 14 (2014) 4901-4906.
[129] J. Qian, W.A. Henderson, W. Xu, P. Bhattacharya, M. Engelhard, O. Borodin, J.-G. Zhang, Nat Commun, 6 (2015).
[130] B. Liang, Y. Liu, Y. Xu, J Power Sources, 267 (2014) 469-490.
[131] L.Y. Beaulieu, K.W. Eberman, R.L. Turner, L.J. Krause, J.R. Dahn, Electrochem Solid St, 4 (2001) A137-A140.
[132] J. Xu, Q. Zhang, Y.-T. Cheng, J Electrochem Soc, 163 (2016) A401-A405.
[133] T.M. Higgins, S.-H. Park, P.J. King, C. Zhang, N. McEvoy, N.C. Berner, D. Daly, A. Shmeliov, U. Khan, G. Duesberg, V. Nicolosi, J.N. Coleman, Acs Nano, 10 (2016) 3702-3713.
[134] Q. Si, M. Kawakubo, M. Matsui, T. Horiba, O. Yamamoto, Y. Takeda, N. Seki, N. Imanishi, J Power Sources, 248 (2014) 1275-1280.
[135] S.R. Chen, M.L. Gordin, R. Yi, G. Howlett, H. Sohn, D.H. Wang, Phys Chem Chem Phys, 14 (2012) 12741-12745.
[136] J.P. Maranchi, A.F. Hepp, P.N. Kumta, Electrochem Solid St, 6 (2003) A198-A201.
[137] L.F. Cui, Y. Yang, C.M. Hsu, Y. Cui, Nano Lett, 9 (2009) 3370-3374.

[138] Y.C. Ru, D.G. Evans, H. Zhu, W.S. Yang, Rsc Adv, 4 (2014) 71-75.
[139] I.S. Kim, G.E. Blomgren, P.N. Kumta, J Power Sources, 130 (2004) 275-280.
[140] W. Boerjan, J. Ralph, M. Baucher, Annu Rev Plant Biol, 54 (2003) 519-546.
[141] A. Bahi, A. Goudarzi, M. Cho, L. Lin, M.A. Karaaslan, F.K. Ko, Design, Manufacturing and Applications of Composites, (2015) 195-205.
[142] U.E.P. Agency, (2009).
[143] T. Saito, R.H. Brown, M.A. Hunt, D.L. Pickel, J.M. Pickel, J.M. Messman, F.S. Baker, M. Keller, A.K. Naskar, Green Chem, 14 (2012) 3295-3303.
[144] W.C. Oliver, G.M. Pharr, J Mater Res, 19 (2004) 3-20.
[145] W.C. Oliver, G.M. Pharr, J Mater Res, 7 (1992) 1564-1583.
[146] B. Key, R. Bhattacharyya, M. Morcrette, V. Seznec, J.-M. Tarascon, C.P. Grey, J Am Chem Soc, 131 (2009) 9239-9249.
[147] M. Klett, J.A. Gilbert, S.E. Trask, B.J. Polzin, A.N. Jansen, D.W. Dees, D.P. Abraham, J Electrochem Soc, 163 (2016) A875-A887.
[148] S.E. Trask, K.Z. Pupek, J.A. Gilbert, M. Klett, B.J. Polzin, A.N. Jansen, D.P. Abraham, J Electrochem Soc, 163 (2016) A345-A350.
[149] N. Dupré, P. Moreau, E. De Vito, L. Quazuguel, M. Boniface, A. Bordes, C. Rudisch, P. Bayle-Guillemaud, D. Guyomard, Chem Mater, 28 (2016) 2557-2572.
[150] D. Molina Piper, T. Evans, S. Xu, S.C. Kim, S.S. Han, K.L. Liu, K.H. Oh, R. Yang, S.H. Lee, Adv Mater, (2015).
[151] M. Klett, J.A. Gilbert, K.Z. Pupek, S.E. Trask, D.P. Abraham, J Electrochem Soc, 164 (2017) A6095-A6102.
[152] X. Zhou, Y.-X. Yin, L.-J. Wan, Y.-G. Guo, Chem Commun, 48 (2012) 2198-2200.
[153] V. Dave, A. Prasad, H. Marand, W.G. Glasser, Polymer, 34 (1993) 3144-3154.
[154] A.C. Ferrari, J. Robertson, Philosophical transactions. Series A, Mathematical, physical, and engineering sciences, 362 (2004) 2477-2512.
[155] A.C. Ferrari, J. Robertson, Physical Review B, 64 (2001) 075414.
[156] M. Wu, X. Xiao, N. Vukmirovic, S. Xun, P.K. Das, X. Song, P. Olalde-Velasco, D. Wang, A.Z. Weber, L.-W. Wang, J Am Chem Soc, 135 (2013) 12048-12056.
[157] W. Cousins, R. Armstrong, W. Robinson, Journal of Materials Science, 10 (1975) 1655-1658.
[158] X.C. Xiao, W.D. Zhou, Y.N. Kim, I. Ryu, M. Gu, C.M. Wang, G. Liu, Z.Y. Liu, H.J. Gao, Adv Funct Mater, 25 (2015) 1426-1433.
[159] J. Song, M. Zhou, R. Yi, T. Xu, M.L. Gordin, D. Tang, Z. Yu, M. Regula, D. Wang, Adv Funct Mater, (2014) n/a-n/a.
[160] N. Liu, L. Hu, M.T. McDowell, A. Jackson, Y. Cui, Acs Nano, 5 (2011) 6487-6493.
[161] Q. Zhang, J. Pan, P. Lu, Z. Liu, M.W. Verbrugge, B.W. Sheldon, Y.-T. Cheng, Y. Qi, X. Xiao, Nano Lett, 16 (2016) 2011-2016.
[162] J. Yang, Y. Takeda, N. Imanishi, C. Capiglia, J. Xie, O. Yamamoto, Solid State Ionics, 152 (2002) 125-129.
[163] M. Miyachi, H. Yamamoto, H. Kawai, T. Ohta, M. Shirakata, J Electrochem Soc, 152 (2005) A2089-A2091.
[164] S.C. Jung, H.-J. Kim, J.-H. Kim, Y.-K. Han, The Journal of Physical Chemistry C, 120 (2016) 886-892.
[165] M. Al-Maghrabi, J. Suzuki, R. Sanderson, V. Chevrier, R. Dunlap, J. Dahn, J Electrochem Soc, 160 (2013) A1587-A1593.
[166] A. Veluchamy, C.-H. Doh, D.-H. Kim, J.-H. Lee, D.-J. Lee, K.-H. Ha, H.-M. Shin, B.-S. Jin, H.-S. Kim, S.-I. Moon, J Power Sources, 188 (2009) 574-577.
[167] P. Lv, H. Zhao, C. Gao, Z. Du, J. Wang, X. Liu, J Power Sources, 274 (2015) 542-550.
[168] D.J. Lee, M.-H. Ryou, J.-N. Lee, B.G. Kim, Y.M. Lee, H.-W. Kim, B.-S. Kong, J.-K. Park, J.W. Choi, Electrochem Commun, 34 (2013) 98-101.

[169] J. Wang, H. Zhao, J. He, C. Wang, J. Wang, J Power Sources, 196 (2011) 4811-4815.
[170] X. Hou, J. Wang, M. Zhang, X. Liu, Z. Shao, W. Li, S. Hu, Rsc Adv, 4 (2014) 34615-34622.
[171] X. Bai, Y. Yu, H.H. Kung, B. Wang, J. Jiang, J Power Sources, 306 (2016) 42-48.
[172] J.R. Szczech, S. Jin, Energ Environ Sci, 4 (2011) 56-72.
[173] J. Wang, M. Zhou, G. Tan, S. Chen, F. Wu, J. Lu, K. Amine, Nanoscale, 7 (2015) 8023-8034.
[174] D. Wang, M. Gao, H. Pan, J. Wang, Y. Liu, J Power Sources, 256 (2014) 190-199.
[175] L. Qie, W. Chen, H. Xu, X. Xiong, Y. Jiang, F. Zou, X. Hu, Y. Xin, Z. Zhang, Y. Huang, Energ Environ Sci, 6 (2013) 2497-2504.
[176] Z. Li, Z. Xu, X. Tan, H. Wang, C.M. Holt, T. Stephenson, B.C. Olsen, D. Mitlin, Energ Environ Sci, 6 (2013) 871-878.
[177] C.-M. Park, W. Choi, Y. Hwa, J.-H. Kim, G. Jeong, H.-J. Sohn, J Mater Chem, 20 (2010) 4854-4860.
[178] A. Hohl, T. Wieder, P.A. van Aken, T.E. Weirich, G. Denninger, M. Vidal, S. Oswald, C. Deneke, J. Mayer, H. Fuess, Journal of Non-Crystalline Solids, 320 (2003) 255-280.
[179] J. Guo, X. Chen, C. Wang, J Mater Chem, 20 (2010) 5035-5040.
[180] L. Shi, W. Wang, A. Wang, K. Yuan, Z. Jin, Y. Yang, J Power Sources, 318 (2016) 184-191.
[181] Y. Nagao, H. Sakaguchi, H. Honda, T. Fukunaga, T. Esaka, J Electrochem Soc, 151 (2004) A1572-A1575.
[182] Y. Yamada, Y. Iriyama, T. Abe, Z. Ogumi, J Electrochem Soc, 157 (2010) A26-A30.
[183] X. Zhou, L.J. Wan, Y.G. Guo, Small, 9 (2013) 2684-2688.
[184] I. Choi, M.J. Lee, S.M. Oh, J.J. Kim, Electrochim Acta, 85 (2012) 369-376.
[185] S. Yoo, J. Kim, B. Kang, Electrochim Acta, 212 (2016) 68-75.
[186] Y. Ren, X. Wu, M. Li, Electrochim Acta, 206 (2016) 328-336.
[187] L. Beaulieu, T. Hatchard, A. Bonakdarpour, M. Fleischauer, J. Dahn, J Electrochem Soc, 150 (2003) A1457-A1464.
[188] Z. Wang, Y. Fu, Z. Zhang, S. Yuan, K. Amine, V. Battaglia, G. Liu, J Power Sources, 260 (2014) 57-61.
[189] V. Etacheri, R. Marom, R. Elazari, G. Salitra, D. Aurbach, Energ Environ Sci, 4 (2011) 3243-3262.
[190] C.K. Chan, H.L. Peng, G. Liu, K. McIlwrath, X.F. Zhang, R.A. Huggins, Y. Cui, Nat Nanotechnol, 3 (2008) 31-35.
[191] J.K. Yoo, J. Kim, Y.S. Jung, K. Kang, Adv Mater, 24 (2012) 5452-5456.
[192] Y. He, X. Yu, Y. Wang, H. Li, X. Huang, Adv Mater, 23 (2011) 4938-4941.
[193] J. Li, X. Xiao, Y.-T. Cheng, M.W. Verbrugge, The Journal of Physical Chemistry Letters, 4 (2013) 3387-3391.
[194] D.M. Piper, J.J. Travis, M. Young, S.B. Son, S.C. Kim, K.H. Oh, S.M. George, C. Ban, S.H. Lee, Adv Mater, 26 (2014) 1596-1601.
[195] N.-S. Choi, K.H. Yew, K.Y. Lee, M. Sung, H. Kim, S.-S. Kim, J Power Sources, 161 (2006) 1254-1259.
[196] S. Dalavi, P. Guduru, B.L. Lucht, J Electrochem Soc, 159 (2012) A642-A646.
[197] N. Delpuech, N. Dupre, P. Moreau, J.-S. Bridel, J. Gaubicher, B. Lestriez, D. Guyomard, Chemsuschem, 9 (2016) 841-848.
[198] S. Goriparti, E. Miele, F. De Angelis, E. Di Fabrizio, R. Proietti Zaccaria, C. Capiglia, J Power Sources, 257 (2014) 421-443.
[199] H.R. Philipp, Journal of Non-Crystalline Solids, 8 (1972) 627-632.
[200] H. Philipp, J Phys Chem Solids, 32 (1971) 1935-1945.
[201] R. Dupree, D. Holland, D. Williams, Philosophical Magazine B, 50 (1984) L13-L18.
[202] R. Temkin, Journal of Non-Crystalline Solids, 17 (1975) 215-230.

[203] K. Schulmeister, W. Mader, Journal of Non-Crystalline Solids, 320 (2003) 143-150.
[204] T. Kim, S. Park, S.M. Oh, J Electrochem Soc, 154 (2007) A1112-A1117.
[205] K. Yasuda, Y. Kashitani, S. Kizaki, K. Takeshita, T. Fujita, S. Shimosaki, J Power Sources, 329 (2016) 462-472.
[206] H. Yamamura, K. Nobuhara, S. Nakanishi, H. Iba, S. Okada, Journal of the Ceramic Society of Japan, 119 (2011) 855-860.
[207] C.-H. Doh, H.-M. Shin, D.-H. Kim, Y.-C. Ha, B.-S. Jin, H.-S. Kim, S.-I. Moon, A. Veluchamy, Electrochemistry Communications, 10 (2008) 233-237.
[208] M. Obrovac, L. Krause, J Electrochem Soc, 154 (2007) A103-A108.
[209] S. Schnurre, J. Gröbner, R. Schmid-Fetzer, Journal of Non-Crystalline Solids, 336 (2004) 1-25.
[210] F.T. Ferguson, J.A. Nuth, Journal of Chemical & Engineering Data, 57 (2012) 721-728.
[211] M. Mamiya, M. Kikuchi, H. Takei, Journal of crystal growth, 237 (2002) 1909-1914.
[212] M. Mamiya, H. Takei, M. Kikuchi, Journal of the Japanese Association of Crystal Growth, 27 (2000) 169.
[213] L. Brewer, R.K. Edwards, The Journal of Physical Chemistry, 58 (1954) 351-358.
[214] S. Hernández, A. Martínez, P. Pellegrino, Y. Lebour, B. Garrido, E. Jordana, J. Fedeli, Journal of Applied Physics, 104 (2008) 4304.
[215] T. Miyuki, Y. Okuyama, T. Sakamoto, Y. Eda, T. Kojima, T. Sakai, Electrochemistry, 80 (2012) 401-404.
[216] Y. Hwa, C.-M. Park, H.-J. Sohn, J Power Sources, 222 (2013) 129-134.
[217] T. Tashiro, M. Dougakiuchi, M. Kambara, Science and Technology of Advanced Materials, 17 (2016) 744-752.
[218] C.C. Nguyen, H. Choi, S.-W. Song, J Electrochem Soc, 160 (2013) A906-A914.
[219] H. Takezawa, K. Iwamoto, S. Ito, H. Yoshizawa, J Power Sources, 244 (2013) 149-157.
[220] M.K. Kim, B.Y. Jang, J.S. Lee, J.S. Kim, S. Nahm, J Power Sources, 244 (2013) 115-121.
[221] P. Lu, C. Li, E.W. Schneider, S.J. Harris, The Journal of Physical Chemistry C, 118 (2014) 896-903.
[222] K. Fridman, R. Sharabi, R. Elazari, G. Gershinsky, E. Markevich, G. Salitra, D. Aurbach, A. Garsuch, J. Lampert, Electrochemistry Communications, 33 (2013) 31-34.
[223] M. Ko, S. Chae, S. Jeong, P. Oh, J. Cho, Acs Nano, 8 (2014) 8591-8599.
[224] Y. Li, K. Yan, H.-W. Lee, Z. Lu, N. Liu, Y. Cui, Nature Energy, 1 (2016) 15029.
[225] D.-T. Nguyen, J. Kang, K.-M. Nam, Y. Paik, S.-W. Song, J Power Sources, 303 (2016) 150-158.
[226] L. Zhang, J. Deng, L. Liu, W. Si, S. Oswald, L. Xi, M. Kundu, G. Ma, T. Gemming, S. Baunack, Adv Mater, 26 (2014) 4527-4532.
[227] J. Zhao, Z. Lu, H. Wang, W. Liu, H.-W. Lee, K. Yan, D. Zhuo, D. Lin, N. Liu, Y. Cui, J Am Chem Soc, 137 (2015) 8372-8375.
[228] H.J. Kim, S. Choi, S.J. Lee, M.W. Seo, J.G. Lee, E. Deniz, Y.J. Lee, E.K. Kim, J.W. Choi, Nano Lett, 16 (2015) 282-288.
[229] J. Zhao, Z. Lu, N. Liu, H.-W. Lee, M.T. McDowell, Y. Cui, Nat Commun, 5 (2014).
[230] S.W. Hwang, W.Y. Yoon, J Electrochem Soc, 161 (2014) A1753-A1758.
[231] L. Wang, Y. Fu, V.S. Battaglia, G. Liu, Rsc Adv, 3 (2013) 15022-15027.
[232] M.W. Forney, M.J. Ganter, J.W. Staub, R.D. Ridgley, B.J. Landi, Nano Lett, 13 (2013) 4158-4163.
[233] I.W. Seong, W.Y. Yoon, J Power Sources, 195 (2010) 6143-6147.
[234] I.W. Seong, K.T. Kim, W.Y. Yoon, J Power Sources, 189 (2009) 511-514.
[235] E. Park, H. Yoo, J. Lee, M.-S. Park, Y.-J. Kim, H. Kim, Acs Nano, 9 (2015) 7690-7696.
[236] J.H. Yom, J.K. Lee, W.Y. Yoon, J Appl Electrochem, 45 (2015) 397-403.
[237] W. Wu, J. Shi, Y. Liang, F. Liu, Y. Peng, H. Yang, Phys Chem Chem Phys, 17 (2015) 13451-13456.

[238] T. Osaka, H. Nara, T. Momma, T. Yokoshima, J Mater Chem A, 2 (2014) 883-896.
[239] J.-S. Kim, C.C. Nguyen, H.-J. Kim, S.-W. Song, Rsc Adv, 4 (2014) 12878-12881.
[240] E. Pollak, G. Salitra, V. Baranchugov, D. Aurbach, The Journal of Physical Chemistry C, 111 (2007) 11437-11444.
[241] H. Nara, T. Yokoshima, M. Otaki, T. Momma, T. Osaka, Electrochim Acta, 110 (2013) 403-410.
[242] T. Morita, N. Takami, J Electrochem Soc, 153 (2006) A425-A430.
[243] M. Miyachi, H. Yamamoto, H. Kawai, J Electrochem Soc, 154 (2007) A376-A380.
[244] M.T. McDowell, S.W. Lee, W.D. Nix, Y. Cui, Adv Mater, 25 (2013) 4966-4984.
[245] P. Lv, H. Zhao, C. Gao, T. Zhang, X. Liu, Electrochim Acta, 152 (2015) 345-351.
[246] J.K. Lee, J. ha Lee, B.K. Kim, W.Y. Yoon, Electrochim Acta, 127 (2014) 1-6.
[247] K.W. Kim, H. Park, J.G. Lee, J. Kim, Y.-U. Kim, J.H. Ryu, J.J. Kim, S.M. Oh, Electrochim Acta, 103 (2013) 226-230.
[248] X. Feng, J. Yang, Q. Lu, J. Wang, Y. Nuli, Phys Chem Chem Phys, 15 (2013) 14420-14426.
[249] Y. Yao, J. Zhang, L. Xue, T. Huang, A. Yu, J Power Sources, 196 (2011) 10240-10243.
[250] M. Yamada, A. Ueda, K. Matsumoto, T. Ohzuku, J Electrochem Soc, 158 (2011) A417-A421.
[251] Z. Lu, L. Zhang, X. Liu, J Power Sources, 195 (2010) 4304-4307.
[252] W.-R. Liu, Y.-C. Yen, H.-C. Wu, M. Winter, N.-L. Wu, J Appl Electrochem, 39 (2009) 1643-1649.
[253] C.-H. Doh, C.-W. Park, H.-M. Shin, D.-H. Kim, Y.-D. Chung, S.-I. Moon, B.-S. Jin, H.-S. Kim, A. Veluchamy, J Power Sources, 179 (2008) 367-370.
[254] X. Yuan, Y.-J. Chao, Z.-F. Ma, X. Deng, Electrochem Commun, 9 (2007) 2591-2595.
[255] J.-H. Kim, H.-J. Sohn, H. Kim, G. Jeong, W. Choi, J Power Sources, 170 (2007) 456-459.
[256] C. Gao, H. Zhao, P. Lv, C. Wang, J. Wang, T. Zhang, Q. Xia, J Electrochem Soc, 161 (2014) A2216-A2221.
[257] M.-S. Park, E. Park, J. Lee, G. Jeong, K.J. Kim, J.H. Kim, Y.-J. Kim, H. Kim, Acs Appl Mater Inter, 6 (2014) 9608-9613.
[258] T. Zhang, J. Gao, H. Zhang, L. Yang, Y. Wu, H. Wu, Electrochemistry communications, 9 (2007) 886-890.
[259] Y.S. Hu, R. Demir-Cakan, M.M. Titirici, J.O. Müller, R. Schlögl, M. Antonietti, J. Maier, Angewandte Chemie International Edition, 47 (2008) 1645-1649.
[260] F. Dai, R. Yi, M.L. Gordin, S. Chen, D. Wang, Rsc Adv, 2 (2012) 12710-12713.
[261] J.-I. Lee, N.-S. Choi, S. Park, Energ Environ Sci, 5 (2012) 7878-7882.
[262] J.Y. Howe, D.J. Burton, Y. Qi, H.M. Meyer, M. Nazri, G.A. Nazri, A.C. Palmer, P.D. Lake, J Power Sources, 221 (2013) 455-461.
[263] Q. Si, K. Hanai, T. Ichikawa, A. Hirano, N. Imanishi, Y. Takeda, O. Yamamoto, J Power Sources, 195 (2010) 1720-1725.
[264] L. Ji, X. Zhang, Carbon, 47 (2009) 3219-3226.
[265] Q. Si, K. Hanai, T. Ichikawa, M. Phillipps, A. Hirano, N. Imanishi, O. Yamamoto, Y. Takeda, J Power Sources, 196 (2011) 9774-9779.
[266] Y. Ren, J. Ding, N. Yuan, S. Jia, M. Qu, Z. Yu, J Solid State Electr, 16 (2012) 1453-1460.
[267] Y. Li, X. Hou, J. Wang, J. Mao, Y. Gao, S. Hu, Journal of Materials Science: Materials in Electronics, 26 (2015) 7507-7514.
[268] X. Zhou, Y.X. Yin, L.J. Wan, Y.G. Guo, Adv Energy Mater, 2 (2012) 1086-1090.
[269] D.T. Nguyen, C.C. Nguyen, J.-S. Kim, J.Y. Kim, S.-W. Song, Acs Appl Mater Inter, 5 (2013) 11234-11239.
[270] X. Yuan, H. Xin, X. Qin, X. Li, Y. Liu, H. Guo, Electrochim Acta, 155 (2015) 251-256.
[271] H. Guo, R. Mao, X. Yang, J. Chen, Electrochim Acta, 74 (2012) 271-274.
[272] S. Yoo, J.I. Lee, M. Shin, S. Park, Chemsuschem, 6 (2013) 1153-1157.

[273] K.W. Lim, J.-I. Lee, J. Yang, Y.-K. Kim, H.Y. Jeong, S. Park, H.S. Shin, Acs Appl Mater Inter, 6 (2014) 6340-6345.
[274] Z. Pan, Z. Dai, L. Xu, S. Lee, Z. Wang, The Journal of Physical Chemistry B, 105 (2001) 2507-2514.
[275] S. Lee, N. Wang, Y. Zhang, Y. Tang, Mrs Bull, 24 (1999) 36-42.
[276] J.-I. Lee, S. Park, Nano Energy, 2 (2013) 146-152.
[277] B.-C. Yu, Y. Hwa, J.-H. Kim, H.-J. Sohn, Electrochim Acta, 117 (2014) 426-430.
[278] N. Deprez, D. McLachlan, Journal of Physics D: Applied Physics, 21 (1988) 101.
[279] P.D. Antunez, D.H. Webber, R.L. Brutchey, Chem. Mater, 25 (2013) 2385-2387.
[280] C. Feng, L. Huang, Z. Guo, H. Liu, Electrochemistry communications, 9 (2007) 119-122.
[281] H. Yamamura, S. Nakanishi, H. Iba, J Power Sources, 232 (2013) 264-269.
[282] A.M. Andersson, M. Herstedt, A.G. Bishop, K. Edström, Electrochim Acta, 47 (2002) 1885-1898.
[283] K. Homma, M. Kambara, T. Yoshida, Science and Technology of Advanced Materials, (2016).
[284] D. Aurbach, K. Gamolsky, B. Markovsky, Y. Gofer, M. Schmidt, U. Heider, Electrochim Acta, 47 (2002) 1423-1439.
[285] L. Chen, K. Wang, X. Xie, J. Xie, Electrochemical and solid-state letters, 9 (2006) A512-A515.
[286] A. Yamano, M. Morishita, M. Yanagida, T. Sakai, J Electrochem Soc, 162 (2015) A1730-A1737.
[287] Q. Yuan, F. Zhao, Y. Zhao, Z. Liang, D. Yan, Electrochim Acta, 115 (2014) 16-21.
[288] J.-Y. Eom, I.-H. Jung, J.-H. Lee, J Power Sources, 196 (2011) 9810-9814.
[289] H.-C. Wu, C.-Y. Su, D.-T. Shieh, M.-H. Yang, N.-L. Wu, Electrochemical and solid-state letters, 9 (2006) A537-A541.
[290] T. Kajita, R. Yuge, K. Nakahara, J. Iriyama, H. Takahashi, R. Kasahara, T. Numata, S. Serizawa, K. Utsugi, J Electrochem Soc, 160 (2013) A1806-A1810.
[291] T. Kajita, R. Yuge, K. Nakahara, J. Iriyama, H. Takahashi, R. Kasahara, T. Numata, S. Serizawa, K. Utsugi, J Electrochem Soc, 161 (2014) A708-A711.
[292] W.H. Shin, H.M. Jeong, B.G. Kim, J.K. Kang, J.W. Choi, Nano Lett, 12 (2012) 2283-2288.
[293] Z. Li, Z. Xu, X. Tan, H. Wang, C.M.B. Holt, T. Stephenson, B.C. Olsen, D. Mitlin, Energ Environ Sci, 6 (2013) 871-878.
[294] H.M. Jeong, J.W. Lee, W.H. Shin, Y.J. Choi, H.J. Shin, J.K. Kang, J.W. Choi, Nano Lett, 11 (2011) 2472-2477.
[295] J.H. Hou, C.B. Cao, F. Idrees, X.L. Ma, Acs Nano, 9 (2015) 2556-2564.
[296] M. Seredych, D. Hulicova-Jurcakova, G.Q. Lu, T.J. Bandosz, Carbon, 46 (2008) 1475-1488.
[297] J. Woo, S.-H. Baek, J.-S. Park, Y.-M. Jeong, J.H. Kim, J Power Sources, 299 (2015) 25-31.
[298] H. Zheng, J. Li, X. Song, G. Liu, V.S. Battaglia, Electrochim Acta, 71 (2012) 258-265.
[299] X. Yang, Z. Wen, X. Xu, B. Lin, S. Huang, J Power Sources, 164 (2007) 880-884.
[300] Y. Gao, J.L. Burba III, in, Google Patents, 2004.
[301] C. Jarvis, M. Lain, Y. Gao, M. Yakovleva, J Power Sources, 146 (2005) 331-334.
[302] R. Petibon, V. Chevrier, C. Aiken, D. Hall, S. Hyatt, R. Shunmugasundaram, J. Dahn, J Electrochem Soc, 163 (2016) A1146-A1156.
[303] Z. Lu, J.R. Dahn, J Electrochem Soc, 149 (2002) A815-A822.
[304] B. Philippe, R. Dedryvère, J. Allouche, F. Lindgren, M. Gorgoi, H. Rensmo, D. Gonbeau, K. Edström, Chem Mater, 24 (2012) 1107-1115.
[305] J. Saint, M. Morcrette, D. Larcher, L. Laffont, S. Beattie, J.P. Pérès, D. Talaga, M. Couzi, J.M. Tarascon, Adv Funct Mater, 17 (2007) 1765-1774.
[306] M.T. McDowell, S.W. Lee, I. Ryu, H. Wu, W.D. Nix, J.W. Choi, Y. Cui, Nano Lett, 11 (2011) 4018-4025.

[307] M.T. McDowell, S.W. Lee, J.T. Harris, B.A. Korgel, C. Wang, W.D. Nix, Y. Cui, Nano Lett, 13 (2013) 758-764.

Vita

Education

University of Kentucky, M.S. in Materials Science and Engineering, 2014

Tianjin University of Technology, B.S. in Materials Physics, 2011

Published work at University of Kentucky

1. **Chen, T.**; Zhang, Q.; Pan, J.; Xu, J.; Liu, Y.; Al-Shroofy, M.; Cheng, Y.-T., Low-Temperature Treated Lignin as Both Binder and Conductive Additive for Silicon Nanoparticle Composite Electrodes in Lithium-Ion Batteries. ACS Appl Mater Inter 2016, 8 (47), 32341-32348.

2. **Chen, T.**; Zhang, Q.; Xu, J.; Pan, J.; Cheng, Y.-T., Binder-free lithium ion battery electrodes made of silicon and pyrolized lignin. RSC Adv 2016, 6 (35), 29308-29313.

3. Al-Shroofy, M.; Zhang, Q.; Xu, J.; **Chen, T.**; Kaur, A. P.; Cheng, Y.-T., Solvent-free dry powder coating process for low-cost manufacturing of LiNi1/3Mn1/3Co1/3O2 cathodes in lithium-ion batteries. J Power Sources 2017, 352, 187-193.

4. Xu, J.; Zhang, L.; Wang, Y.K.; **Chen, T.**; Al-Shroofy, M.; Cheng, Y.-T., Unveiling the Roles of Polymeric Binders for Silicon Nanoparticles in Lithium-Ion Full Cells. ACS Appl Mater Inter 2017, 9 (4), 3562-3569.

5. Gulati, G. K.; **Chen, T.**; Hinds, B. J., Programmable carbon nanotube membrane-based transdermal nicotine delivery with microdialysis validation assay. Nanomedicine: Nanotechnology, Biology and Medicine 2017, 13 (1), 1-9.

6. Chen, Z.; **Chen, T.**; Sun, X.; Hinds, B. J., Dynamic Electrochemical Membranes for Continuous Affinity Protein Separation. Adv Funct Mater 2014, 24 (27), 4317-4323.